**POLITECNICO DI MILANO**

Facoltà di Ingegneria Industriale

Corso di Laurea Magistrale in Ingegneria Aeronautica


# Impulse Response in a Turbulent Channel Flow

Relatore: Prof. Maurizio QUADRIO

Tesi di laurea di:
Andrea Roberto CODRIGNANI
Matr. 784036

Anno Accademico 2012 - 2013

**Abstract**

This work describes the measurement through a direct numerical simulation (D.N.S.) of the response of a turbulent flow confined between two planar walls to an impulsive body force. This measurement is performed by considering, for the first time, the dependency of the forcing distance from the wall. A zero-mean white-noise volume forcing is used to probe the turbulent flow, and the response function is obtained by accumulating the space-time correlation between the white forcing and the velocity field.
The interest of this research lies primarily in the context of control theory, where the mean impulse response can have relevant applications in the design of closed-loop control laws which exploit the response function to describe the system dynamics.
The numerical simulations have been performed using a well parallelized D.N.S. solver, whose response measurement procedure has been improved in order to deal with the considerable computational effort.
The measurements have been carried out for both a laminar and a turbulent base flow and, for both the cases, the linearity range has been checked at various forcing distances. The impulse response analysis has bought to the confirmation and extension of some important results known in literature. Furthermore the three dimensional visualization of the response has allowed the identification of the topology of the interaction mechanisms between the body forcing and the flow.

**Key words:** impulse response, body force, anisotropic turbulence, D.N.S., channel flow

**Sommario**

In questa tesi viene descritta la misura tramite simulazione numerica diretta (D.N.S.) della risposta impulsiva di un flusso turbulento confinato tra due pareti piane ad un forzamento di volume. Tale misura viene effettuata considerando, per la prima volta, la dipendenza della distanza del punto di applicazione della forza dalla parete. La tecnica di misura consiste nell'introduzione di un forzamento di volume avente la forma di un rumore bianco a media nulla. La risposta è quindi calcolata misurando la correlazione spazio-temporale tra l'ingresso e il campo di moto in modo da filtrare le fluttuazioni di velocità non dovute al forzamento.
L'interesse della ricerca si colloca nell'ambito della teoria del controllo lineare, dove la funzione di risposta lineare media può avere importanti applicazione nella progettazione di compensatori retroazionati che sfruttano la risposta stessa come modello del sistema.
Fondamentale è stato l'utilizzo di un codice di calcolo D.N.S. con strategia di calcolo parallelo la cui procedura di misura della risposta impulsiva, già presente, è stata migliorata al fine di affrontare il notevole sforzo computazionale. Quest'ultimo ha richiesto particolare cura nell'impostazione dei parametri della risposta impulsiva anche a causa dei pochi riferimenti presenti in letteratura.
Le misure sono state effettuate sia in regime lamiare sia turbolento verificandone la linearità per diverse quote di forzamento. L'analisi della risposta impulsiva ha portato alla conferma e all'estensione di alcuni importanti risultati noti in letteratura. Inoltre, è stato possibile ricavare la topologia dei meccanismi di interazione tra la forzante di volume e la corrente.

**Parole chiave:** risposta impulsiva, forzante di volume, turbolenza anisotropa, D.N.S., canale piano

# Contents

# Introduction

> Some think, king Gelon, that the number of the sand grains can't be counted.
>
> Archimedes

In the incipit of *the Sand Reckoner*, the maximum scientist of the ancient times, shows that the number of sand grains is finite by computing and upper bound. Archimedes opposes to those ancient knowledge that defines mysteries inherently unaccessible to the mankind. The point is not the presumption of completeness of his knowledge. It is the opposite: the awareness that the yesterday ignorance can be lighted today and today's one can be lighted tomorrow. With this spirit the scientific research goes on nowadays, towards the deep comprehensions of the open problems of the modern physics.

Among these, turbulent flow description represents one of the most beautiful mathematical challenges.

## 0.1 Importance of turbulent flows

The most part of the flows in the everyday surroundings has a turbulent behaviours. Atmospheric phenomena, the blood flow in the human body, the wake of a supersonic airplane or the pipe flows of a gas or a liquid, are all turbulent phenomena that have a strong impact on the nature and on the life of human beings. This explains the great interest that physicists and engineers have always aimed to this kind of flows.

Despite the lack of a coherent and complete definition, a generic flow is considered turbulent when some specific properties are present. The main properties are the randomness of the single implementation, the high Reynolds numbers, the repeatability of the statistics, the presence of random velocity variations a low scales, the feature of energy dissipation and the three dimensional nature.

According to Pope [29], the state of art of turbulent flow study and research can be divided in the three main fronts.

- Theoretical comprehension of properties and dynamics of turbulent flows, which allows further developments in turbulence modeling and prediction;
- Experimental campaigns, both numerical and practical which allows the discovery of qualitative and quantitative data on several turbulent flows;
- Flow control techniques, which allows the achievement of particular engineering goals trough the change of particular flow characteristics.

The present work focuses mainly on the second and the third branch, but lays the basis to interesting developments in also in the first one.

Before introducing the main subject of this work, namely the mean impulse response of a turbulent channel flow, a survey about the third research branch, which studies the flow control, is needed.

## 0.2 Flow control for turbulent drag reduction

Flow control technologies have the great capability to manipulate the flow field to obtain specific behaviours which bring better performances and satisfy complex design qualities. The economic impact of the development of such technologies is really promising, since it would be able to save billions of dollar in annual fuel costs for land, air and sea vehicles and it wuold improve the efficiency of many industrial processes involving turbulent flows. Moreover important results could be achieved in pollutant reduction and environment protection.

In aeronautic field, the main aims of control design can be the lift increase, the noise suppression, the improve of mix-mass in the engines, and of course the drag reduction. The latter is the most suitable for a control technique which exploits the mean impulse response. Furthermore, according to a recent study committed by Airbus [35], the application of turbulence and separation control could lead up to a 15% decrease of the drag of a civil airplane (figure 1).

Flow control techniques can be divided into two main groups

- active control, which requires the introduction of external energy in the system

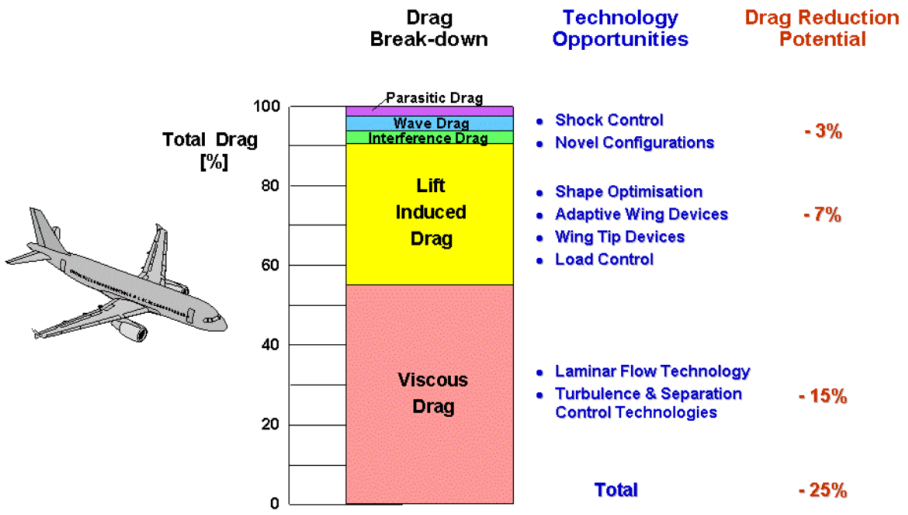


FIGURE 1. Drag breakdown of a civil airplane during cruise flight, the percentages show the possible improvement potential according to [35]

- passive control, which simply modifies the system dynamics with out external energy.

The control actuation through body forcing belongs to the first group and it is an expanding research field. This forcing technique has the distinctive feature of a direct manipulation of the system dynamics, while usual forcing methods operate on the boundary condition of the system. The possibility to operate on the whole domain and in every direction, allows the design of versatile control laws.

The main examples of this kind of forcing are the electromagnetic actuators used for the EMHD control with ionized flows, and the non-thermal plasma actuators DBD for the control of standard fluids. In the last two decades many works implying a body forcing have been presented in literature. Many papers exploit conducting fluids with an EMHD approach, such as the numerical works of Berger *et al.* [1] where a comparison is done, at different Reynolds numbers, between open and closed-loop control techniques with traveling waves, with drag reduction results of about 40%. Other works, following similar paths, are those of Pang and Choi [26] and Du, Symeonidis and Karniadakis [8]. Also an important experimental activity in this field of body forcing control is carried, such as in the works by Stenzel *et al.* [37, 36].

The research is focusing also on what concerns non thermal plasma DBD actuators, Porter *et al.* [30] studied a possible plasma applications to prevent and control the flow separation over lifting surfaces, while Whalley and Choi ([5]) demonstrated the effectiveness of this kind of actuators also from the

experimental viewpoint. Other important works are presented in the 2007 and 2010 annual reviews respectively by Moreau [22] and by Corke *et al.* [6].

This research field is more and more supported by the development of micro electro mechanical system technology (MEMS). Indeed, since closed-loop control laws require the knowledge of the system state, a great availability of sensors is needed to improve the effective and the efficient of the control. The first successful experiments have been reached with this devices in the works of Yoshino *et al.* in [38] and of Kasagi, Suzuki and Fukagata in [15], where a drag reduction of about 7% has been reached. The importance of this result lays in the great versatility of MEMS technologies and their low energy consumption feature.

## 0.3 Linear control and impuse response

Linear Control is the branch of the control theory which is applied to linear systems. Important applications can be obtained also for nonlinear systems which can be brought in the linear control framework with a linearization. This practice always lead to a limitation: the control does not operate on the overall system but on its fluctuations around an equilibrium condition.

A reference paper about the application of linear control to turbulent flows is by Bewley (2001 [2]), where the author applies a linear control on the channel flow through an actuation of the kind *blowing/suction*, employing an observer based on the Kalman filter. Another works that follows this research path is the one by Luchini, Bewley and Quadrio (2005 [18]), where the basis for a Wiener-Hopf control are established.

The Wiener-hopf control is a powerful technique which synthesizes at the same time the observer and the controller exploiting the impulse response of the system to the considered forcing. With this technique, a big part of the control design process is dedicated to the measurement of the impulse response. In [20] (2006) Luchini, Quadrio and Zuccher measured, for the first time, the mean impulse response of a turbulent channel flow, with a *blowing/-suction* forcing at wall. The particularity of their measurement procedure lies in the use of a DNS solver, without any need of linearized equation.

These important results merged in the Phd thesis of Martinelli (2009 [21]), who realized a Wiener-Hopf compensator based on the *blowing/suction* forcing in the channel flow. An extension to [20] has been done in the master thesis work of Pelis and Rampanelli (2011 [28]), where the response measurement procedure is expanded and validated for a body forcing put at a generic distance from the wall.

This thesis is the continuation of the above mentioned works and focuses

on the description of the impulse response due to a generic body forcing in the turbulent channel flow.

## 0.4 Aim of the study

The core of this thesis is the whole measurement and description of the impulse response in a turbulent channel flow, with a complete investigation of the dependency of the impulse response from the application point distance of the forcing from the wall. The knowledge of the impulse response, computed with a DNS based approach, allows to understand the dynamics of the perturbation propagations in the whole domain, by posing them directly in the Navier–Stokes equations. The impulse response can explain the linearized dynamics of the system and it may allows the simulation of the most relevant flow dynamics. A possible benefit of the knowledge of such a mathematical object is the research of the most suitable strategies to design a flow control application. For these reason particular attention is dedicated to the research of the effects on the velocity filed due to different forcing directions.

## 0.5 Structure of the work

The present work is structured in the following manner.

- **Chapter 1: Plane channel flow**. A brief description of the set of equations that governs the flow in a channel is provided, also with the numerical strategy adopted to solve it. This presentation also includes the presence of the body force perturbation
- **Chapter 2: Mean impulse response in the channel flow**. This chapter defines the mean impulse response in a turbulent channel flow and its theoretical demonstration. Then the numerical implementation of the DNS based measurement of the impulse response is presented
- **Chapter 3: Simulation planning** The complete description of the impulse response needs an huge amount of computational efforts, for these reason this chapter is dedicated to the planning of the simulations campaign which has led to the results.
- **Chapter 4: Results** The results are here presented, first giving the outcomes of the turbulent linearity tests. Then the analysis of the impulse response norm allows the comparison with some literature results. After this, the physical space representation of the impulse response is

shown, giving particular attention to the interaction mechanism between the forcing directions and the velocity field. Finally, a preliminary control test is done by computing the velocity field due to a given forcing by means of the impulse response with a convolution computation.

# 1 | Plane Channel Flow

Plane channel plays an important role in the study of interactions between flow and rigid boundaries. This canonical problem provides an excellent testbed for the study of both transition and turbulence in wall-bounded flows. Furthermore this geometry is amenable to very efficient Direct Numerical Simulation (DNS) at moderate Reynolds numbers, and shows all the features of more complex wall flows.

DNS can solve faithfully the turbulent time and spatial scale and computational efforts are usually balanced by the geometrical simplicity of the computational domain.

This chapter treats about the equations, which govern the plane channel flow when body forces are present, and their numerical implementation.

## 1.1 Geometry presentation

Problem geometry is shown in figure 1.1. Orthogonal Cartesian axes are named $x$, $y$ and $z$ and they represents, respectively the streamwise, wall-normal and the spanwise directions. Velocity vector components along these directions are, respectively, $u$, $v$ and $w$. The domain is supposed to have infinite length in both the $x$ and $z$ directions.

Due to the infinite extension of walls, one can identify two statistically homogeneous direction, namely $x$ and $z$, so that the Reynolds-averaged streamwise velocity $\langle u \rangle$ depends only on the wall-normal coordinate $y$. Thanks to this double homogeneity it is possible to take a finite-length doubly-periodic domain for computations. This means that the computational domain has a streamwise and spanwise length of $L_x$ and $L_z$ with periodic boundary conditions on the unbounded portion of the domain.

$$\mathbf{u}(L_x, y, z) = u_j(0, y, z) \qquad \mathbf{u}(x, y, L_z) = u_j(x, y, 0) \tag{1.1a, b}$$

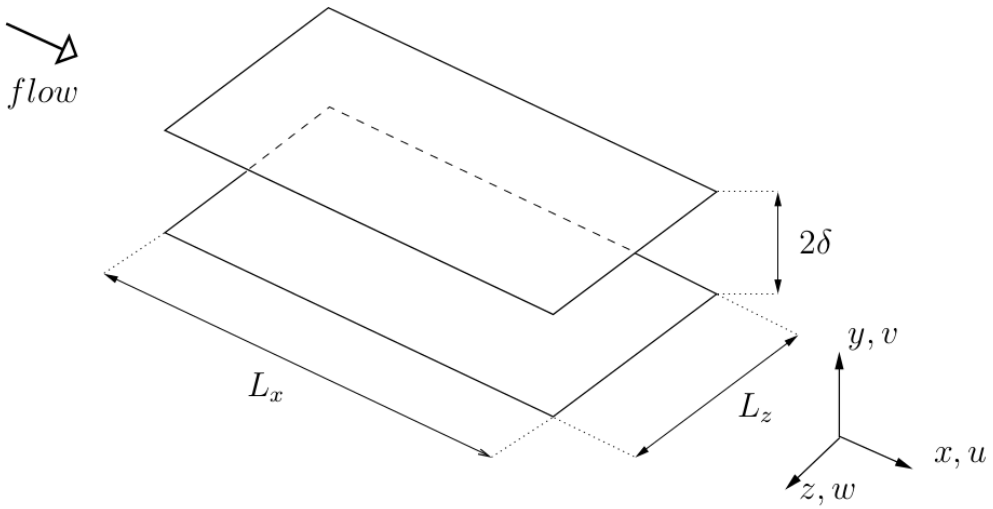


FIGURE 1.1. reference system and problem geometry

### 1.1.1 The Reynolds number

Incompressible viscous flow phenomena can be scaled by an unique parameter, the Reynolds number. Several Reynolds numbers can be defined in a channel flow according to the choice of the reference velocity. One is based on the bulk velocity $U_b$ (which represents the mean channel flow rate) defined as

$$U_b = \frac{1}{2\delta}\int_0^{2h} \langle u \rangle dy \tag{1.2}$$

hence the Reynolds bulk is

$$Re_b = \frac{U_b \delta}{\nu} \tag{1.3}$$

Where $\nu$ is the kinematic viscosity of the fluid and $\delta$ is the reference dimension which corresponds to the half of the channel height.

$$\delta = \frac{y_u - y_l}{2} \tag{1.4}$$

with $y_u$ and $y_l$ the upper and lower wall position.

Moreover, a Reynolds number can be defined, based on the channel half-width and the velocity $U_p$, that is the centerline velocity of a Poiseuille flow with the same mass flow rate, obtaining

$$Re_p = \frac{U_p \delta}{\nu} \tag{1.5}$$

Considering the parabolic law of a laminar Poiseuille flow and the definition 1.2, it is easy to observe that $U_b = \frac{2}{3}U_p$. Another well know definition of the Reynolds number is obtained with the wall unit velocity $u_\tau$ as reference velocity.

$$Re_\tau = \frac{u_\tau \delta}{\nu} \tag{1.6}$$

$u_\tau$ is proportional to the square root of the wall stress $\tau_w$, hence $Re_\tau$ depends on the mean streamwise velocity derive and the Reynolds used in the equation scaling.

$$Re_\tau = \sqrt{< \frac{\partial u}{\partial y} > (Re_b \text{ or } Re_p)} \tag{1.7}$$

All the results in the present work are obtained scaling the equations with $Re_b$ and, for compatibility reasons with the literature, they are presented referring to $Re_\tau$. The flow is driven by a time-varying streamwise pressure gradient, in order to keep a constant volume-flow rate (per unit surface) of $Q = 2$, and respect the periodic boundary conditions on the velocity. thus the the spanwise flow rate vary in time around its null mean value.

## 1.2 Incompressible Navier–Stokes Equations

Channel flow phenomena are well described by incompressible Navier–Stokes equations in Cartesian coordinates 1.8. Navier–Stokes equations govern the general evolution of incompressible viscous fluid flows. These equations compose a system of partial differential equations which is a mathematical statement of the conservation law of mass, and of the balance law for the momentum of a fluid.

$$\begin{cases} \dfrac{\partial \mathbf{u}}{\partial t} + (\mathbf{u} \cdot \nabla)\mathbf{u} + \dfrac{\nabla P}{\bar{\rho}} = \nu \nabla^2 \mathbf{u} + \mathbf{f_v} \\ \nabla \cdot \mathbf{u} = 0 \end{cases} \tag{1.8}$$

Where $\mathbf{f_v}$ represents the body force vector normalized per mass unit with $\bar{\rho}$, hence with the dimension of an acceleration. Usually these equations are implemented in a simpler dimensionless form, which better expresses the

relevance of the Reynolds number.

$$\begin{cases} \dfrac{\partial u}{\partial t} + u\dfrac{\partial u}{\partial x} + v\dfrac{\partial u}{\partial y} + w\dfrac{\partial u}{\partial y} + \dfrac{\partial p}{\partial x} = \dfrac{1}{Re}\nabla^2 u + f_x & \text{(1.10a)} \\ \dfrac{\partial v}{\partial t} + u\dfrac{\partial v}{\partial x} + v\dfrac{\partial v}{\partial y} + w\dfrac{\partial v}{\partial y} + \dfrac{\partial p}{\partial x} = \dfrac{1}{Re}\nabla^2 v + f_y & \text{(1.10b)} \\ \dfrac{\partial w}{\partial t} + u\dfrac{\partial w}{\partial x} + v\dfrac{\partial w}{\partial y} + w\dfrac{\partial w}{\partial y} + \dfrac{\partial p}{\partial x} = \dfrac{1}{Re}\nabla^2 w + f_z & \text{(1.10c)} \\ \dfrac{\partial u}{\partial x} + \dfrac{\partial v}{\partial y} + \dfrac{\partial w}{\partial z} = 0 & \text{(1.10d)} \end{cases}$$

Dimensionless forces $f_j$ are obtained scaling each components of $\mathbf{f_v}$ with the reference quantities.

$$\mathbf{f_v} = \frac{U_{ref}}{T_{ref}}\Big(f_x; f_y; f_z\Big) \tag{1.11}$$

Thanks to the incompressible hypothesis, the mass conservation becomes a non-evolutive equation and represents a cinematic constraint that must be satisfied everywhere and at any time in the domain. Furthermore incompressible flow nature allows a decoupling of the energy equation from 1.10, Hence the pressure does not satisfy a state equation but it acts as a Lagrange multiplier to enforce the constraint of null divergence. However, once computed the velocity field, is possible to recover the pressure field by taking the divergence of the momentum equation and applying the divergence-free constraint, obtaining the Poisson equation for the pressure with the presence of a body force.

$$\nabla^2 P = -\nabla \cdot (\mathbf{u} \cdot \nabla \mathbf{u}) + \nabla \cdot \mathbf{f_v} \tag{1.12}$$

Since no Dirichlet condition exists for this equation, pressure is defined up to an arbitrary function of time $P(t)$ which may be assigned [17], [32] as

$$\bar{P}(t) = \frac{1}{\Omega}\int_\Omega P(\mathbf{x}, t) d\Omega \tag{1.13}$$

The problem composed by the differential equations 1.10 is closed with the initial conditions for all the variables and with the appropriate boundary conditions.

$$\begin{cases} \mathbf{u}(x, y, z, 0) = \mathbf{u_0}(x, y, z) & \text{initial condition} \\ \left.\begin{array}{l} \mathbf{u}(x, y_l, z, t) = 0 \\ \mathbf{u}(x, y_u, z, t) = 0 \end{array}\right\} & \text{boundary conditions} \\ \left.\begin{array}{l} \mathbf{u}(L_x, y, z) = \mathbf{u}(0, y, z) \\ \mathbf{u}(x, y, L_z) = \mathbf{u}(x, y, 0) \end{array}\right\} & \text{cyclic wall conditions} \end{cases} \tag{1.14}$$

No condition is required for the body force, since it is considered as an input whose evolution is known. Initial and boundary conditions can not be freely chosen but have to respect three compatibility conditions namely

$$\begin{cases} \nabla \cdot \mathbf{u_0} = 0 & \text{(1.15a)} \\ \oint_S \hat{\mathbf{n}} \cdot \mathbf{u} dS & \text{(1.15b)} \\ \hat{\mathbf{n}} \cdot \mathbf{u_0}(\mathbf{x})|_S = \hat{\mathbf{n}} \cdot \mathbf{u}(\mathbf{x_0}, 0)|_S & \text{(1.15c)} \end{cases}$$

where $\hat{\mathbf{n}}$ is the unit vector normal tho each boundary surface $S$ of the domain. Equation 1.15a forces the initial field to satisfy the divergence-free condition. While the other two equations are satisfied by homogeneous boundary conditions on the walls and by cyclic conditions on the lateral sides.

## 1.3 $v$-$\eta$ formulation

Null divergence constraint often leads to particular difficulties in the numerical solution of incompressible Navier–Stokes equations. This problem could be solved, theoretically, projecting the equations in a divergence-free manifold. In this way one obtains a set of equations that automatically satisfies the cinematic constraint and does not need the Lagrangian multiplier $P$. The price of this choice is the increase of implementation complexities about boundary conditions and their compatibility. Despite these drawbacks, this approach founds large usage in simple domains such as the plane channel.

Kim *et al.* have shown in [16] that, applied to plane channel, the divergence-free equations take a form very suitable for the numerical solution. In their paper authors exploited all the main characteristics of an incompressible viscous flow in a plane channel by introducing a new formulation called $v$-$\eta$. This formulation transforms the four equations in 1.10 into two scalar differential equations for the wall-normal velocity $v$ and the wall-normal vorticity $\eta$ which is defined as

$$\eta = \frac{\partial u}{\partial z} + \frac{\partial w}{\partial x} \tag{1.16}$$

The equation for the wall-normal velocity can be obtained by taking the laplacian of the $y$-component of the momentum equation and by substituting it in the Poisson equation for pressure, obtaining:

$$\frac{\partial \nabla^2 v}{\partial t} = h_v + \frac{1}{Re}\nabla^2\nabla^2 v + \left(\frac{\partial^2}{\partial^2 x} + \frac{\partial^2}{\partial^2 z}\right) f_y - \frac{\partial}{\partial y}\left(\frac{\partial f_x}{\partial x} + \frac{\partial f_z}{\partial z}\right) \tag{1.17}$$

with

$$\begin{aligned} h_v = \frac{\partial}{\partial y}\Bigg[ \frac{\partial}{\partial x}\left( u\frac{\partial u}{\partial x} + v\frac{\partial u}{\partial y} + u\frac{\partial u}{\partial x} \right) + \\ \frac{\partial}{\partial z}\left( u\frac{\partial w}{\partial x} + v\frac{\partial w}{\partial y} + u\frac{\partial w}{\partial x} \right) \Bigg] + \\ -\left( \frac{\partial^2}{\partial^2 x} + \frac{\partial^2}{\partial^2 z} \right)\left( u\frac{\partial v}{\partial x} + v\frac{\partial v}{\partial y} + u\frac{\partial v}{\partial x} \right) \end{aligned} \tag{1.18}$$

The equation for the wall-normal vorticity can be easily obtained by taking the $y$-component of the curl of the momentum equation for $v$, leading to

$$\frac{\partial \eta}{\partial t} = h_\eta + \frac{1}{Re}\nabla^2 \eta + \frac{\partial f_x}{\partial z} - \frac{\partial f_z}{\partial x} \tag{1.19}$$

with

$$h_\eta = \frac{\partial}{\partial x}\left( u\frac{\partial w}{\partial x} + v\frac{\partial w}{\partial y} + u\frac{\partial w}{\partial z} \right) - \frac{\partial}{\partial z}\left( u\frac{\partial u}{\partial x} + v\frac{\partial u}{\partial y} + u\frac{\partial u}{\partial z} \right) \tag{1.20}$$

The original NS equations becomes a system of two scalar partial differential equations, that is fourth-order (in space) for $v$ and second-order for $\eta$. Therefore the $v$-$\eta$ formulation needs six boundary conditions, four for $v$ and two for $\eta$.

$$\begin{cases} \dfrac{\partial \nabla^2 v}{\partial t} = h_v + \dfrac{1}{Re}\nabla^2\nabla^2 v + \left( \dfrac{\partial^2}{\partial^2 x} + \dfrac{\partial^2}{\partial^2 z} \right) f_y - \dfrac{\partial}{\partial y}\left( \dfrac{\partial f_x}{\partial x} + \dfrac{\partial f_z}{\partial z} \right) \\ \dfrac{\partial \eta}{\partial t} = h_\eta + \dfrac{1}{Re}\nabla^2 \eta + \dfrac{\partial f_x}{\partial z} - \dfrac{\partial f_z}{\partial x} \\ \dfrac{\partial v}{\partial y}(x, y_{l/u}, z) = 0 \qquad \text{non-penetration} \\ \left.\begin{array}{l} v(x, y_{l/u}, z) = 0 \\ \eta(x, y_{l/u}, z) = 0 \end{array}\right\} \qquad \text{non-slip} \end{cases} \tag{1.21}$$

The two remaining velocity components $u$ and $w$ can be recovered *a posteriori* through the null divergence constraint and the definition of $\eta$, solving the following system of two equations.

$$\begin{cases} \dfrac{\partial u}{\partial x} + \dfrac{\partial w}{\partial z} = -\dfrac{\partial v}{\partial y} \\ \dfrac{\partial u}{\partial z} - \dfrac{\partial w}{\partial x} = \eta \end{cases} \tag{1.22}$$

## 1.4 Numerical Discretization

Navier–Stokes equations in their $v$-$\eta$ formulation present many advantages in the numerical discretization when applied to channel geometry. The route to the discretized set of equations and boundary conditions begins with the Fourier expansion in the two homogeneous directions. Then time and spatial derivatives are discretized and the parallelization discussed.

### 1.4.1 Fourier expansion

Geometries with homogeneous directions such as plane channel, allows a representation of the solution $v(x,y,z,t)$ and $\eta(x,y,z,t)$ in terms of a complete expansion that automatically respects the cyclic boundary condition. The most suitable choice for a numerical implementation, falls over Fourier series expansion in the spatial invariant directions $x$ and $z$. A practice well established in literature [16], [19] defines the fundamental wavenumbers in homogeneous directions as

$$\alpha_0 = \frac{2\pi}{L_x} \qquad \beta_0 = \frac{2\pi}{L_z} \tag{1.23a, b}$$

given these numbers is possible to rewrite the solution as

$$v(x,y,z,t) = \sum_{h=-N_x/2}^{N_x/2} \sum_{l=-N_z/2}^{N_z/2} \hat{v}\Big(\alpha, y, \beta, t\Big) e^{i\alpha_0 h t} e^{i\beta_0 l t} \tag{1.24}$$

$$\eta(x,y,z,t) = \sum_{h=-N_x/2}^{N_x/2} \sum_{l=-N_z/2}^{N_z/2} \hat{\eta}\Big(\alpha, y, \beta, t\Big) e^{i\alpha_0 h t} e^{i\beta_0 l t} \tag{1.25}$$

the integers $h$ and $l$ are, respectively, the streamwise and spanwise index that spans the Fourier space so that $\alpha = h\alpha_0$ and $\beta = l\beta_0$. $N_x$ and $N_z$ are the maximum Fourier mode for each directions. Fourier series coefficients depend on $y$ since the presence of the walls does not allow the expansion in this direction. Now Fourier expansion can be introduced in the $v$-$\eta$ set A.1, leading to the discretized equation set.

$$\begin{cases} \dfrac{\partial}{\partial t}\Big(\mathcal{D}_2(\hat{v}) - k^2\hat{v}\Big) = \dfrac{1}{Re}\Big(\mathcal{D}_4(\hat{v}) - 2k^2\mathcal{D}_2(\hat{v}) + k^4\hat{v}\Big) + \\ \qquad\qquad -k^2\widehat{HV} - \mathcal{D}_1\Big(i\alpha\widehat{HU} + i\beta\widehat{HW}\Big) + \\ \qquad\qquad +k^2\hat{f}_y - i\alpha\mathcal{D}_1(\hat{f}_x) - i\beta\mathcal{D}_1(\hat{f}_z) \\ \dfrac{\partial\hat{\eta}}{\partial t} = \dfrac{1}{Re}\Big(\mathcal{D}_2(\hat{\eta} - k^2\hat{\eta})\Big) + i\beta\widehat{HU} - i\alpha\widehat{HW} + i\beta\hat{f}_x - i\alpha\hat{f}_z \end{cases} \tag{1.26}$$

The symbol $\mathcal{D}_n(\,\cdot\,)$ is the $n$-th order derivative operator in $y$ direction and $k^2 = \alpha^2 + \beta^2$. The nonlinear terms, which come from Fourier-transforming the convective part of Navier–Stokes equations, are grouped in the following definitions.

$$\begin{aligned}
\widehat{HU} &= i\alpha\widehat{uu} + \mathcal{D}_1(\widehat{vu}) + i\beta\widehat{wu} \\
\widehat{HV} &= i\alpha\widehat{uv} + \mathcal{D}_1(\widehat{vv}) + i\beta\widehat{wv} \\
\widehat{HW} &= i\alpha\widehat{uw} + \mathcal{D}_1(\widehat{vw}) + i\beta\widehat{ww}
\end{aligned} \tag{1.27}$$

Since the force $f_j$ is known, we can easily notice that the system 1.26 is uncoupled if also the nonlinear terms are known. This is possible if those terms are treated explicitly in the time discretization, keeping in mind that such a treatment will lead to a conditionally stable method. Hence they can be solved separately in the time progress scheme. Non linear terms computation require the knowledge of the velocity field in physical variables $u$, $v$ and $w$, that can be recovered by solving the Fourier-space counterpart of 1.22, namely

$$\begin{cases}
\hat{u} = \dfrac{1}{k^2}\left[i\alpha\mathcal{D}_1(\hat{v}) - i\beta\hat{\eta}\right] \\
\hat{\eta} = \dfrac{1}{k^2}\left[i\beta\mathcal{D}_1(\hat{v}) + i\alpha\hat{\eta}\right]
\end{cases} \tag{1.28}$$

This is a $2 \times 2$ algebraic system that can be solved very efficiently.

The system 1.28 above becomes singular for the mean value of $u$ and $w$, that is for $k^2 = 0$. Hence for the mean velocity components recovery a different procedure is required. Two additional equations must be written to calculate $u$ and $w$. They can be worked out by applying the linear plane-average operator to the relevant components of the momentum equations 1.10.

$$\begin{cases}
\dfrac{\partial\hat{u}}{\partial t} = \dfrac{1}{Re}\mathcal{D}_2(\hat{u}) - \mathcal{D}_1(\widehat{vu}) + \bar{p_x} \\
\dfrac{\partial\hat{w}}{\partial t} = \dfrac{1}{Re}\mathcal{D}_2(\hat{w}) - \mathcal{D}_1(\widehat{vw}) + \bar{p_z}
\end{cases} \tag{1.29}$$

Where $\bar{p}_x$ and $\bar{p}_z$ are the forcing terms required to win the viscous drag of the fluid. Body force effects are not considered in mean flow computation since it is assumed that is neglectable or with null mean value. For the streamwise direction, $\bar{p}_x$ can be an imposed mean pressure gradient, and, during the simulation, the flow rate through the channel will oscillate in time around its mean value. Constant flow rate simulations can be also performed by imposing $\bar{p}_x$ as a time-dependent spatially uniform pressure gradient. The

same procedure can be applied to spanwise forcing term $\bar{p}_z$, in this case however the imposed mean pressure gradient or the imposed mean flow rate is zero, while the other quantity will be zero only after time average.

Fourier series 1.24 is truncated according to a trade-off between resolution and time and memory costs. Furthermore we must notice that every variable is real, hence the Fourier series enjoy the following property:

$$\hat{f}(\alpha) = \hat{f}^*(-\alpha) \tag{1.30}$$

This represents a great benefit about memory occupation. It is possible, indeed, to save only half of the coefficients and compute the remaining with equation 1.30.

Nonetheless this considerations, a Fourier series approach may appears unsuitable since the computation of nonlinear terms $\widehat{HU}$, $\widehat{HV}$ and $\widehat{HW}$ becomes an expensive convolution in the wavenumber space. A more efficient way has been proposed by Luchini and Quadrio in [19]. The three velocity components, can be transformed back to time domain where the convolution of non linear terms becomes a simple product whose result is transformed again in the wave number space. Transforms are computed very efficiently by Fast Fourier Transform (FFT), and in order to preserve spectral accuracy, a de-aliasing factor of 3/2 is introduced to expand the number of collocation points before transforming from wavenumber to physical space.

### 1.4.2 Time Discretization

Time integration of system 1.26 is performed by a semi-implicit method, which is a common approach in DNS implementation. Particular attention has been aimed to memory occupation efficiency.

Viscous term is the most stability-limiting part of the equation, hence it is discretized with an implicit second-order Crank-Nicholson (CN) scheme. This scheme allows an higher time step $\delta t$ which is now solely constrained by CFL condition of the explicit third-order low-storage Runge-Kutta method (RK3) used for advancing nonlinear terms, which can thus benefit from a higher precision [23]. The discretized equations of system 1.26 for $v$ and $\eta$

are the following.

$$\begin{aligned}
&\overbrace{\frac{\lambda}{\delta t}\hat{\eta}_{hl}^{n+1} - \frac{1}{Re}\Big[\mathcal{D}_2(\hat{\eta}_{hl}^{n+1}) - k^2\hat{\eta}_{hl}^{n+1}\Big]}^{implicit\ terms} = \\
&= \overbrace{\frac{\lambda}{\delta t}\hat{\eta}_{hl}^{n} + \frac{1}{Re}\Big[\mathcal{D}_2(\hat{\eta}_{hl}^{n}) - k^2\hat{\eta}_{hl}^{n}\Big]}^{implicit\ terms} + \\
&+ \underbrace{\theta\Big(i\beta_0 l\widehat{HU}_h l - i\alpha_0 h\widehat{HW}_h l + i\beta\hat{f}_x - i\alpha\hat{f}_z\Big)^{n}}_{explicit\ terms} + \\
&+ \underbrace{\xi\Big(i\beta_0 l\widehat{HU}_h l - i\alpha_0 h\widehat{HW}_h l + i\beta\hat{f}_x - i\alpha\hat{f}_z\Big)^{n-1}}_{explicit\ terms}
\end{aligned} \tag{1.31}$$

$$\begin{aligned}
&\overbrace{\frac{\lambda}{\delta t}\Big[\mathcal{D}_2(\hat{v}_{hl}^{n+1}) - k^2\hat{v}_{hl}^{n+1}\Big] - \frac{1}{Re}\Big[\mathcal{D}_4(\hat{v}_{hl}^{n+1}) - 2k^2\mathcal{D}_2(\hat{v}_{hl}^{n+1}) + k^4\hat{v}_{hl}^{n+1}\Big]}^{implicit\ terms} = \\
&= \overbrace{\frac{\lambda}{\delta t}\Big[\mathcal{D}_2(\hat{v}_{hl}^{n}) - k^2\hat{v}_{hl}^{n}\Big] - \frac{1}{Re}\Big[\mathcal{D}_4(\hat{v}_{hl}^{n}) - 2k^2\mathcal{D}_2(\hat{v}_{hl}^{n}) + k^4\hat{v}_{hl}^{n}\Big]}^{implicit\ terms} + \\
&+ \underbrace{\theta\Big[-k^2\widehat{HV}_{hl} - \mathcal{D}_1\Big(i\alpha_0 h\widehat{HU}_{hl} + i\beta_0 l\widehat{HW}_{hl}\Big) - k^2\hat{f}_y - i\alpha\mathcal{D}_1(\hat{f}_x) - i\beta\mathcal{D}_1(\hat{f}_z)\Big]^{n}}_{explicit\ terms} + \\
&+ \underbrace{\xi\Big[-k^2\widehat{HV}_{hl} - \mathcal{D}_1\Big(i\alpha_0 h\widehat{HU}_{hl} + i\beta_0 l\widehat{HW}_{hl}\Big) - k^2\hat{f}_y - i\alpha\mathcal{D}_1(\hat{f}_x) - i\beta\mathcal{D}_1(\hat{f}_z)\Big]^{n-1}}_{explicit\ terms}
\end{aligned} \tag{1.32}$$

Coefficients $\lambda$, $\theta$ and $\xi$ appearing in the equations, take different values according to integration scheme chosen. In the Runge-Kutta scheme used, each temporal step $\delta t$ is split, in turn, in three smaller steps $\delta t_i$ solved with different coefficients $\lambda_i$, $\theta_i$ and $\xi_i$ (table 1.1).

As mentioned before, first of all the velocity product appearing in non-linear terms are computed through direct/inverse FFT explicitly. Then the algorithm has to solve a set of two ODEs derived from the implicit formulation of viscous terms, for each wavenumber pairs $(\alpha, \beta)$. A discrete solution of the resulting ODEs is needed in the wall-normal direction. Hence a compact fourth-order finite difference discretization has been introduced in order to

guarantee the correct spectral accuracy. Finally such discretization produces two linear systems with real banded matrices, whose solution gives $\hat{v}_{hl}^{n+1}$ and $\hat{\eta}_{hl}^{n+1}$. Homogeneous velocity components $\hat{u}_{hl}^{n+1}$ and $\hat{w}_{hl}^{n+1}$ are easily recovered solving the system 1.28. Unlike the procedure used to build the RHS, this second step proceeds per wall-normal planes, since the simultaneous knowledge of the RHS in all $y$ positions is required.

| $i$ | $\delta t_i$ | $\lambda_i$ | $\theta_i$ | $\xi_i$ |
|---|---|---|---|---|
| 1 | $64/120\delta t$ | 1/2 | 2 | 0 |
| 2 | $16/120\delta t$ | 1/2 | 50/8 | -34/8 |
| 3 | $40/120\delta t$ | 1/2 | 90/20 | -50/20 |

TABLE 1.1. time step solution parameter

### 1.4.3 Wall normal derivatives

In order to reach the fourth order accuracy, the finite difference scheme use a computational stencil of five grid points. Given the coefficients $d_n^j(i)$ for the generic $n$-th derivate, centered in the grid point $y_j$, the derivate computation is performed satisfying the constraint

$$\mathcal{D}_n(f(y))|_{y=y_j} = \sum_{i=-2}^{2} d_n^j f(y_{j+i}) \tag{1.33}$$

Clearly a derivative so defined is a polynomial interpolation of the function $f(y)$, whose coefficients are unknown. A possible way to coefficients determination is the Pade's approximation approach [31]. In such approach first the increasing polynomial test function $t_m(y)$ are chosen:

$$t_m(y) = 1, y, y^2, \ldots, y^m \tag{1.34}$$

then analytical derivatives are computed obtaining a system definition of this kind

$$d_j(t_m) - d_0(\mathcal{D}_j(t_m)) = 0 \qquad m = 0, \ldots, 8 \tag{1.35}$$

where $j$ is the derivative order. Once Obtained the zero order coefficients $d_0$ from the condition

$$\sum_{i=-2}^{2} d_0(i) = 1 \tag{1.36}$$

the other coefficients come from the following systems

$$\left.\begin{aligned} d_1(t_m) - d_0(\mathcal{D}_1(t_m)) &= 0 \\ d_2(t_m) - d_0(\mathcal{D}_2(t_m)) &= 0 \\ d_4(t_m) - d_0(\mathcal{D}_4(t_m)) &= 0 \end{aligned}\right\} \qquad m = 0, \ldots, 8 \tag{1.37}$$

## 1.5 Parallel strategy

The most relevant feature of the DNS code used, is its high parallelization performances [19]. Since the authors desired an efficiently and low cost architecture, the aim was to minimize the communication between different machines avoiding complex interface protocol.

Parallel strategy consists in dividing the domain in many slices parallel to homogeneous directions, one for each machine, as shown in figure 1.2. FFT and IFFT process for nonlinear terms computation is executed for each slice independently since no information passages are needed. In order to avoid communication also in wall-normal derivation process, each slice boundary is enlarged with two more $y$ coordinate points. In other words it is better a little increase of problem dimension than slowing the process exchanging informations.

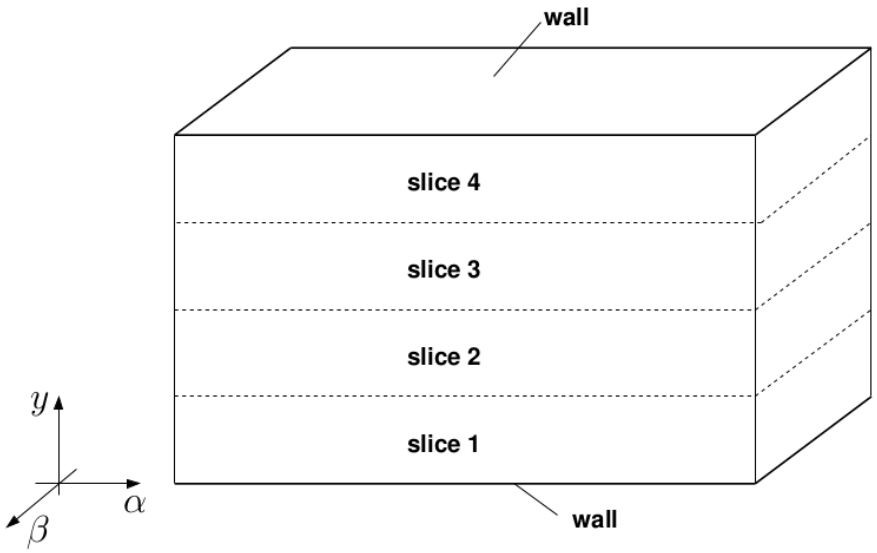


FIGURE 1.2. Domain division with parallel slices of different machines

Time advancing scheme requires the inversion of two pentadiagonal matrices (1.31, 1.32). In this case communication between matrices, apparently

unavoidable, can be reduced proceeding with a serial solution through neighboring machines. Adopting a LU decomposition of pentadiagonal matrix with backward substitution, only few coefficients of the matrix interface must be send to the next machine. Clearly all this process would be useless if the number of pentadiagonal systems is little or even one. Actually, for typical simulation, the number of system to solve is high, *i.e.* one for for each couple of wavenumbers $(N_x+1)(N_z+1) \approx 10^4$. When the LU decomposition of the system matrix for a given pair $(h,l)$ is performed, there is a first loop from the top row of the matrix down to the bottom row, in order to eliminate the unknowns and then a second loop in the opposite direction. So when machine number one finishes the first substitution, the interface coefficients are passed to the next machine, which, in turn, goes on with the substitution. As soon as the first processor finished its first substitution, it begins to substituting another system of a different couple of wavenumbers. Only one synchronization is needed at the end of elimination phase, and then the whole process is repeated with backward substitutions. In this way, if the number of processor is $p$, all the machines work since the last machine begins to handle the $p$-th system.

This parallel computing scheme allows a *point to point* communication modality: each machine exchanges informations only with its neighboring machines. Furthermore the single computing node may be multi-CPU, in this case it is possible to exploit an additional and complementary parallel strategy based on shared-memory parallelization algorithms. Shared-memory allows to divide the slices in more parts through a new distribution of the wavenumbers between CPUs of each computing node.

# 2 | Mean impulse response in the channel flow

Even though a turbulent flow is a non linear phenomenon, a linear response (either in the frequency or in the time domain) can be defined for it if perturbations are small enough. Under linearity hypothesis the response of turbulent flow can be described with an unique mathematical object named impulse response. Impulse response is a powerful tool that allows to characterize the behavior of system, subject to an external forcing, by searching the direct connection between inputs and outputs. The opportunity to focus all the dynamic features of interest in a solely input/output relationship is so useful, that applications of this tool range in every field of engineering interest. This chapter treats about the impulse response of the velocity vector in the whole flow field and in time due to body force perturbations.

In this chapter are discussed the elements used for the impulse response computation. At first, the section 2.1 presents the theoretical impulse response definition, which is applied to the channel flow response measurement in the following section 2.2. Section 2.3 treats the numerical implementation of the measurement technique used. Finally in section 2.4, it is discussed the usage of impulse response to a direct computation of the velocity output field.

## 2.1 Definition

Impulse response function is the dynamic system response to an impulse input, starting with null initial conditions. This concept has the property to include in a solely object all the informations required to obtain system outputs. Thanks to this property, system integration can be avoided leading to an easier way to compute the outputs.

The price of this approach comes with the imposition of linearity. Since the main features of turbulent flows rely on nonlinear effects, in order to

compute the impulse response function we must remain in the linearity range. This is possible choosing properly the forcing amplitude, and assuming that for little perturbations linearity bounds are respected. To underline this passage, from now on, impulse response function $H(t)$ will be called *linear impulse response function* (LIRF), and given the input $\mathbf{g}(t)$ and the output $\mathbf{y}(t)$, its definition is the following

$$\mathbf{y}(t) = \int_{-\infty}^{\infty} H(t-\tau)\mathbf{g}(\tau)d\tau \tag{2.1}$$

From this equation it is easy to see that, according to the sampling property of Dirac delta function $\delta(t)$, if we apply an impulse force $g(t) = \delta(t)$ the output $y(t)$ will be coincident with the impulse response function.

$$\mathbf{y}(t) = \int_{-\infty}^{\infty} H(t-\tau)\mathbf{1}\delta(\tau)d\tau = H(t)\mathbf{1} \tag{2.2}$$

where $\mathbf{1}$ is an unitary column array with the same length of the input vector. Definition 2.1 describes only the time dependency, while in turbulent channel flows input-output relationship is both temporal and spatial. Hence, since the aim is the linear response of the velocity vector in the whole flow field and in time, we need an extension of the previous definition which includes also the spatial convolution in three dimensions. In this way the impulse response function is able to consider not only the forcing history but also its shape. The vectorial nature of body forces makes the response a tensorial quantity, that is denoted with $\mathcal{H}_{ij}$ to indicate the $i$-th component of the response to a forcing in the $j$-th direction.

Hence applying the force in a single direction aligned with a reference axis the velocity output is the following

$$u_i(x,y,z,t) = \int_0^{L_x}\int_{-\delta}^{\delta}\int_0^{L_z}\int_{-\infty}^{\infty} \mathcal{H}_{ij}(x-\xi, y-\eta, z-\zeta, t-\tau) f_j(\xi,\eta,\zeta,\tau)d\tau d\zeta d\eta d\xi \tag{2.3}$$

As described in the subsection 1.4.1, DNS solver applies an hybrid variables formulation, expanding the solution with the Fourier series only in the homogeneous directions $x$ and $z$. Similarly the response is computed in the same formulation, therefore convolutions in $x$ and $z$ directions become simple products in the wavenumbers space.

$$\hat{u}_i(\alpha,y,\beta,t) = \int_{-\delta}^{\delta}\int_{-\infty}^{\infty} \hat{\mathcal{H}}_{ij}(\alpha, y-\eta, \beta, t-\tau)\hat{f}_j(\alpha,\eta,\beta,\tau)d\eta d\tau \tag{2.4}$$

A further simplification can be obtained considering the force $f_j$ as a Dirac delta distribution along the $y$ coordinate. In other word this consists

to apply to force only on a certain wall-normal distance $y'$.

$$\hat{f}_j(\alpha, y, \beta, t) = \hat{\mathfrak{f}}_j(\alpha, \beta, t)\delta(y - y') \tag{2.5}$$

where the symbol $\mathfrak{f}$ points out the force $f$ only in the coordinates $x$, $z$ and $t$ since the dependency from the $y$ coordinate has been substituted with the parameter $y'$. This allows to exploit the sampling property of $\delta(y - y')$ by substituting the new forcing definition 2.5 in the equation 2.4.

$$\hat{u}_i(\alpha, y, \beta, t) = \int_{-\infty}^{\infty} \hat{\mathcal{H}}_{ij}(\alpha, y - y', \beta, t - \tau)\hat{\mathfrak{f}}_j(\alpha, \beta, \tau)d\tau \tag{2.6}$$

Time dependency can be freely shifted, thanks to convolution property, in order obtain a more suitable form for the numerical implementation.

$$\hat{u}_i(\alpha, y, \beta, t) = \int_{-\infty}^{\infty} \hat{\mathcal{H}}_{ij}(\alpha, y - y', \beta, \tau)\hat{\mathfrak{f}}_j(\alpha, \beta, t - \tau)d\tau \tag{2.7}$$

From now on the impulse response tensor notation $\hat{\mathcal{H}}_{ij}(\alpha, y - y', \beta, \tau)$, is replaced with $\hat{\mathcal{H}}_{ij}(\alpha, y, \beta, \tau; y')$ underlining how the wall-normal distance dependency is a parametric dependency indeed.

## 2.2 DNS based measurement of $\mathcal{H}_{ij}$

The first measure of an impulse response in a turbulent flow through a DNS simulation is due to Luchini, Quadrio and Zuccher [20]. Authors computed the mean linear impulse response of a turbulent channel flow with a wall forcing of the kind *blowing/suction*. The response is averaged in time since turbulent fluctuations affect the measure of the velocity field. Further development of this technique has been done by Martinelli in his PhD thesis [21], where the response results found are use to design a feedback control system in the frequency domain. In [4] Carini and Quadrio applied the impulse response computation in the homogeneous isotropic turbulence with body forcing, finding an excellent matching between DNS measures and an analytical result.

The mean impulse response measurement is now explained, first giving a survey of the possible methods existing in literature, and then applying to a body forcing the innovative procedure founded in [20].

In 1970 a pioneer methods to measure the mean impulse response is presented by Hussain and Reynolds in [11]. In this paper authors use a frequency approach exploiting the relationship between impulse response and frequency response. The latter is obtained with a forcing sweep both in

frequency and in wavenumbers domain. The flow, computed with a DNS simulation, has a forcing of the kind

$$\mathfrak{f}_j(x,z,t) = \epsilon_j \sin(\bar{\alpha}x)\sin(\bar{\beta}z)\sin(\bar{\omega}t) \tag{2.8}$$

Chosen an enough small amplitude $\epsilon$ and given $\bar{\alpha}$, $\bar{\beta}$ and $\bar{\omega}$, a phase-locked mean can divide the deterministic effects from the turbulent noise with a reasonable signal to noise ratio. The main drawback is that the response so obtained represents a single point in the variable space $[\alpha, \beta, \omega]$. Hence the iterations of the DNS simulations for a number adequately large of this three parameters, would lead to unsustainable computational efforts.

A second approach could be found relating to the impulse response definition 2.3, employing directly an impulsive forcing with the Dirac delta function.

$$\mathfrak{f}_j(x,z,t) = \epsilon_j \delta(x-x')\delta(z-z')\delta(t-t') \tag{2.9}$$

Thanks to the wavenumbers space formulation, the body force could be Fourier transformed in $x$ and $z$ directions exploiting Dirac delta property, namely

$$\hat{\mathfrak{f}}_j(\alpha,\beta,t) = \epsilon_j \delta(t-t') \tag{2.10}$$

and by substituting in equation 2.7, one obtains

$$\hat{u}_i(\alpha,y,\beta,t) = \int_{-\infty}^{\infty} \hat{\mathcal{H}}_{ij}(\alpha,y,\beta,t-\tau;y')\epsilon_j \delta(\tau-t')d\tau \tag{2.11}$$

Applying the Dirac delta sampling property we finally find

$$\hat{\mathcal{H}}_{ij}(\alpha,y,\beta,t-t';y') \tag{2.12}$$

This kind of forcing allows to compute the whole response in a single measurement simulation. Phased-locked mean is replaced by an average over periodic repetitions well separated, in order to obtain, each time the force is applied, a velocity field uncorrelated from the previous one. However applying the forcing in a so localized manner, with time and spatial impulses, reduces the linearity range considerably. This enforces the employment of small forcing amplitude $\epsilon_j$, finally leading to unsuitable signal to noise ratio. Hence also this approach involves unaffordable computational time to make the mean response emerge from the turbulent noise.

The third way, proposed in [20], bypasses the high linearity limitation above, introducing the statistical correlation as method to measure the impulse response. This idea comes from the signal theory, where, if a white

noise (*i.e.* a delta-correlated signal) is passed though a linear system, the correlation between input and output is proportional to the impulse response of the system itself. Thus authors adopted an independently generated random signal forcing (in their case at the wall), and they obtained at once the whole space-time dependency of the impulse response by computing such a correlation. Furthermore, as opposed to what occurs with the impulsive forcing, the forcing power is uniformly distributed in time and space, hence the linearity range can be enlarged as in the sinusoidal forcing case.

Starting from equation 2.7 the input-output relationship can be rewritten in terms of correlation, looking for the correlation between the velocity field and the force (conjugated in the wavenumbers space).

$$\langle \hat{u}_i(\alpha, y, \beta, t)\hat{\mathfrak{f}}_j^*(\alpha, \beta, t-\mathcal{T})\rangle = \int_0^\infty \hat{\mathcal{H}}_{ij}(\alpha, y, \beta, t-\tau; y')\langle \hat{\mathfrak{f}}_j(\alpha, \beta, \tau)\hat{\mathfrak{f}}_j^*(\alpha, \beta, t-\mathcal{T})\rangle d\tau \tag{2.13}$$

Where the operator $\hat{\mathcal{H}}_{ij}(\alpha, y, \beta, t-\tau; y')$ already assumes the meaning of mean impulse response, so the symbols $\langle \cdot \rangle$ is not needed.

From discrete signals theory, the white noise $w$ is a sequence of uncorrelated random variables with zero mean, this leads to the following property

$$\langle \hat{w}_i(\alpha, y, \beta, t)\hat{w}_j^*(\alpha, \beta, t-\tau)\rangle = \delta(\tau) \tag{2.14}$$

Hence applying a white noise forcing of the kind

$$\hat{\mathfrak{f}}_j(\alpha, \beta, t) = \epsilon\hat{w}(\alpha, \beta, t) \tag{2.15}$$

the equation 2.13 becomes

$$\langle \hat{u}_i(\alpha, y, \beta, t)\hat{\mathfrak{f}}_j^*(\alpha, \beta, t-\mathcal{T})\rangle = \int_0^\infty \hat{\mathcal{H}}_{ij}(\alpha, y, \beta, t-\tau; y')\epsilon^2\delta(\mathcal{T})d\tau \tag{2.16}$$

and once again for the sampling properties of Dirac delta, we obtain

$$\langle \hat{u}_i(\alpha, y, \beta, t)\hat{\mathfrak{f}}_j^*(\alpha, \beta, t-\mathcal{T})\rangle = \hat{\mathcal{H}}_{ij}(\alpha, y, \beta, \mathcal{T}; y')\epsilon^2 \tag{2.17}$$

Finally we obtain the impulse response

$$\hat{\mathcal{H}}_{ij}(\alpha, y, \beta, \mathcal{T}; y') = \frac{\langle \hat{u}_i(\alpha, y, \beta, t)\hat{\mathfrak{f}}_j^*(\alpha, \beta, t-\mathcal{T})\rangle}{\epsilon^2} \tag{2.18}$$

This equation allows to compute the response starting from time 0 till $\mathcal{T}$.

Impulse response computed with the equation 2.18 has a different meaning according to the laminar or turbulent nature of the flow. In laminar

flows, the mean impulse response is actually the deterministic response of the flow and the mean is needed only for the white noise property convergence. Hence *few* averages are enough to get good results. Turbulent case computation, instead, is made more complicated by the turbulence dynamics, which enforces a statistical view point. In other words, equation 2.18 strictly requires the average operator, in order to elide the turbulent velocity fluctuations not related to the forcing. So the average operation is performed for the convergence of both white noise property and turbulent phenomena. In this sense the numbers of time steps necessary to get a numerically correct response must be considerably higher than laminar case, in order to average as many uncorrelated field as possible.

## 2.3 Numerical Implementation

Equation 2.18 has a non trivial numerical implementation since problem dimensions require to handle the memory space carefully. Furthermore particularly attention is focused on efficiency.

As we can see from figure 2.1, the computational procedure is mainly divided in three phases:

1. forcing update
2. correlation computation
3. impulse response memorization and saving

The preliminary phase consists in the choice of the simulation parameters, whose meaning is shown in details further in chapter 3.

### 2.3.1 Forcing update

Forcing update is the first step to response computation. Many ways exists to apply the forcing, varying the number of components used or the time application law, according to the aim of the impulse response analysis. All these possible kinds of forcing are presented further.

The simplest one is initially discussed here, to give a general viewpoint of the response identification procedure. A basic forcing consists in a monodirectional force, aligned with one reference axis, whose white noise is update each DNS time step $\Delta t_{rsp} = \Delta t$, namely

$$f_j(\alpha, \beta, n\Delta t_{rsp}) = \epsilon_j e^{i2\pi rand(n\Delta t_{rsp})} \tag{2.19}$$

Where $rand(n\Delta t_{rsp})$ represents a random number at the time $n\Delta t_{rsp}$, generated with a white noise generation algorithm. Furthermore the exponential allows to generate a random complex number starting from a real one.

### 2.3.2 Correlation computation

The discrete representations of equation 2.18 is the following

$$\hat{\mathcal{H}}_{ij}(\alpha, y, \beta, k\Delta t) = \frac{1}{\epsilon_j^2}\frac{1}{N}\sum_{n=0}^{N-1} \hat{u}_i(\alpha, y, \beta, (n+k)\Delta t)\hat{\mathfrak{f}}_j^*(\alpha, \beta, n\Delta t) \quad (2.20)$$

with $k,\ n \in \mathbb{N}$. $N$ is the maximum number of passed time step, and $k = 0, \ldots, K \leq N$. As in the above subsection, also the correlation could be implemented in more than one manner. Most frequently used algorithm, required the knowledge of the whole time history of both the correlating elements. This traditional approach is unfeasible in a DNS simulation, because the memory storage of the velocity field also in the time, clearly overshoot the limits. The way used here is based on the least memory occupation criteria. Only the forcing history $\mathcal{F}_j$ is saved each updating time step $\Delta t_{sample}$ for a maximum of $nt_{sample}$ time step. At the following updating step, the previous forcing history is shifted by one step and the first slot is update with the new white noise input. Hence at the update iteration $it_{rsp}$ we have

$$\begin{cases} \mathcal{F}^{it_{rsp}}(\alpha, \beta, 1) = \hat{\mathfrak{f}}_j^*(\alpha, \beta, n\Delta t_{sample}) \\ \mathcal{F}^{it_{rsp}}(\alpha, \beta, i+1) = \mathcal{F}^{it_{rsp}-1}(\alpha, \beta, i) \qquad \text{for } i = 2 \ldots nt_{sample} \end{cases} \quad (2.21)$$

Correlation computation simply becomes a sum, between the old term and the product of the velocity field and the forcing history $\mathcal{F}_j$.

$$\begin{aligned} &\hat{\mathcal{H}}_{ij}^{it_{rsp}}(\alpha, y, \beta, k\Delta t_{sample}) = \\ =&\hat{\mathcal{H}}_{ij}^{it_{rsp}-1}(\alpha, y, \beta, k\Delta t_{sample}) + \hat{u}_i^{it_{rsp}}(\alpha, y, \beta)\mathcal{F}_j^{it_{sample}}(\alpha, \beta, k\Delta t_{sample}) \end{aligned} \quad (2.22)$$

for $k = 0 \ldots nt_{sample}$ and for each $\alpha$, $y$ and $\beta$. The impulse response so obtained must be divided by the factor $\epsilon^2 N$ to take in to account the normalization and the mean operator. Proceeding this way only the instantaneous velocity field is required, since the previous fields are implicitly considered in the term $\hat{\mathcal{H}}_{ij}^{t_{rsp}-1}$.

This approach is very memory efficient, since, for a typical simulation, the forcing history require two order of magnitude less memory space than the impulse response, therefore its storage is more handy.

### 2.3.3 Impulse response memorization and saving

The last step is the informations saving. According to the parallel strategy chosen, a typical simulation length may reach the oder of days, hence for precautionary reasons the parameter $\Delta t_{save}$ is introduced to prevents the loss of data in case of unexpected interruptions. This procedure may require up to several minutes according to the calculator architecture.

For this reason the response definition in the homogeneous direction has been reduced by computing the response on a smaller set of wavenumbers $nxh$ and $nzh$. The choice of these parameters will be explained further in the next chapter.

### 2.3.4 Response parallel strategy

As underlined in section 1.5, the main feature of the DNS code developed by Luchini and Quadrio, is the high parallel efficiency. The response computation part of the code preserves the same characteristic by arranging also the correlation in slices. Thanks to this arrangement the forcing updating concerns only the machine which manages the forcing generation. Despite this, as equation 2.20 states, the correlation is computed at every wall-normal distance requiring the updated forcing history. Therefore the machine, which generates the force, needs to communicate the forcing history to the others. Fortunately the dimension of transmitted data is small, and communication times do not have great impact on the total simulation time.

Even the shared memory parallelization is still exploitable both for forcing generation and correlation computation. This allows a further division in more slice between the cores of each single CPU.

## 2.4 Direct convolution simulation

One of the main goals of impulse response identification, is the possibility of a straight computation of the velocity field given a known body force input, without the need of any direct numerical simulation. Furthermore a convolution simulation is an useful tool to test the fidelity of the impulse response computed. If the response is correct, indeed, the convolution output should perfectly match a DNS approach with the same forcing applied.

Starting from the definition of the impulse response 2.1, the velocity field output is obtained as follows

$$\hat{u}_i(\alpha, y, \beta, t) = \int_{-\infty}^{\infty} \hat{\mathcal{H}}_{ij}(\alpha, y, \beta, t-\tau; \bar{y}) \hat{\mathbf{f}}_j(\alpha, \beta, \tau) d\tau \tag{2.23}$$

Linear time invariant system framework, may lead to a better understanding of equation 2.23. Under linearity hypothesis the dynamic system which relates the body force with the velocity field ca be written as

$$\begin{cases} \dot{\mathbf{x}}(t) = A\mathbf{x}(t) + B\mathbf{f}(t) \\ \mathbf{u}(t) = C\mathbf{x} \end{cases} \tag{2.24}$$

Since we are mainly interested to velocity fluctuations, we can impose null initial conditions $\mathbf{x}(0) = \mathbf{0}$. A Fourier transform, also for the time dependency, can be performed to bring the system in the frequency domain, where the input-output relationship emphasizes the tensorial nature of the impulse response $\mathcal{H}_{ij}$.

$$\tilde{\mathbf{u}}(j\omega) = \left[\tilde{C}\left(sI - \tilde{A}\right)^{-1}\tilde{B}\right]\tilde{\mathbf{f}}(j\omega) \tag{2.25}$$

where the symbol $\tilde{(\cdot)}$ states the Laplace transformed variables. By enlarging this vectorial relationship we finally obtain

$$\begin{bmatrix} \tilde{u}(\alpha, y, \beta, j\omega) \\ \tilde{v}(\alpha, y, \beta, j\omega) \\ \tilde{w}(\alpha, y, \beta, j\omega) \end{bmatrix} = \begin{bmatrix} \tilde{\mathcal{H}}_{ux} & \tilde{\mathcal{H}}_{uy} & \hat{\mathcal{H}}_{uz} \\ \tilde{\mathcal{H}}_{vx} & \tilde{\mathcal{H}}_{vy} & \hat{\mathcal{H}}_{vz} \\ \tilde{\mathcal{H}}_{wx} & \tilde{\mathcal{H}}_{wy} & \hat{\mathcal{H}}_{wz} \end{bmatrix} \begin{bmatrix} \tilde{f}_x \\ \tilde{f}_y \\ \tilde{f}_z \end{bmatrix} \tag{2.26}$$

Equation 2.26 suggests an array representation of the impulse response. Thus, in a more general form, convolution result can be written as a summation of the three forcing components.

$$\hat{u}_i(\alpha, y, \beta, t; \bar{y}) = \sum_{j=1}^{3} \int_{-\infty}^{\infty} \hat{\mathcal{H}}_{ij}(\alpha, y, \beta, t - \tau; \bar{y}) \hat{\mathbf{f}}_j(\alpha, \beta, \tau) d\tau \tag{2.27}$$

This equation comes from the linearity hypothesis, and exploits the superposition principle. The same principle is used in section 3.3.1 to obtain each of the nine components of $\hat{\mathcal{H}}_{ij}$ in the same simulation.

The velocity field in the equation 2.27 is computed with a body force localized at single wall-normal distance $\bar{y}$. In other words as shown in section 2.1 the body force has a Dirac delta shape among the $y$ coordinate. For these reason a method is needed which can take into account also the three-dimensional force shape. This could be done by decomposing the forcing shape as a summation of more contributes distributed as Dirac delta among the wall-normal coordinate. Recalling equation 2.5 and considering the single *q-th* wall-normal distance $\bar{y}_q$, the force can be written as

$$\hat{\mathbf{f}}_j(\alpha, \beta, t) = \epsilon_q(\alpha, \beta, t)\delta(y - \bar{y}_q) \tag{2.28}$$

The complete forcing shape can be obtained with the following summation

$$\hat{f}(\alpha, y, \beta, t) = \sum_{q=1}^{N_y-1} \epsilon_q(\alpha, \beta, t)\delta(y - \bar{y}_q) \tag{2.29}$$

Finally employing the convolution equation 2.27 we obtain

$$\hat{u}_i(\alpha, y, \beta, t) = \sum_{q=1}^{N_y-1} \sum_{j=1}^{3} \int_{-\infty}^{\infty} \hat{\mathcal{H}}_{ij}(\alpha, y, \beta, t-\tau; \bar{y}_q)\epsilon_q(\alpha, \beta, t)\delta(y-\bar{y}_q)d\tau \tag{2.30}$$

This equation allows to compute the whole mean velocity field starting from a generic body force with assigned shape and time evolution law. The power of this equation is that any DNS simulation is needed.

### 2.4.1 Convolution implementation

Numerical implementation of impulse response convolution, needs the knowledge of the whole three dimensional forcing history $\mathcal{F}$, with

$$\mathcal{F} = \left[\mathcal{F}_x, \mathcal{F}_y, \mathcal{F}_z\right] \tag{2.31}$$

For this reason, the first computational step concerns the creation of the forcing history for the whole simulation time. The following step consists in the numerical discretization of equation 2.27. This discretization involves a double summation, one on the forcing directions $j$ and one on the time index $n$.

$$\hat{u}(\alpha, y, \beta, k\Delta t_{rsp}) = \sum_{j=1}^{3} \sum_{n=0}^{N} \hat{\mathcal{H}}_{ij}(\alpha, y, \beta, (k-n)\Delta t_{rsp})\mathcal{F}(\alpha, \beta, n\Delta t_{rsp}) \tag{2.32}$$

The results of this approach are presented in the next chapter, in section (??)

It is interesting to notice that, as denote later, for the laminar case a convolution simulation requires (tot volte) less computational time that a DNS approach. While for the turbulent case, a convolution simulation represent the only affordable approach to a mean output description, since the DNS comparison required many days of simulation. (??ancora da dimostrare)

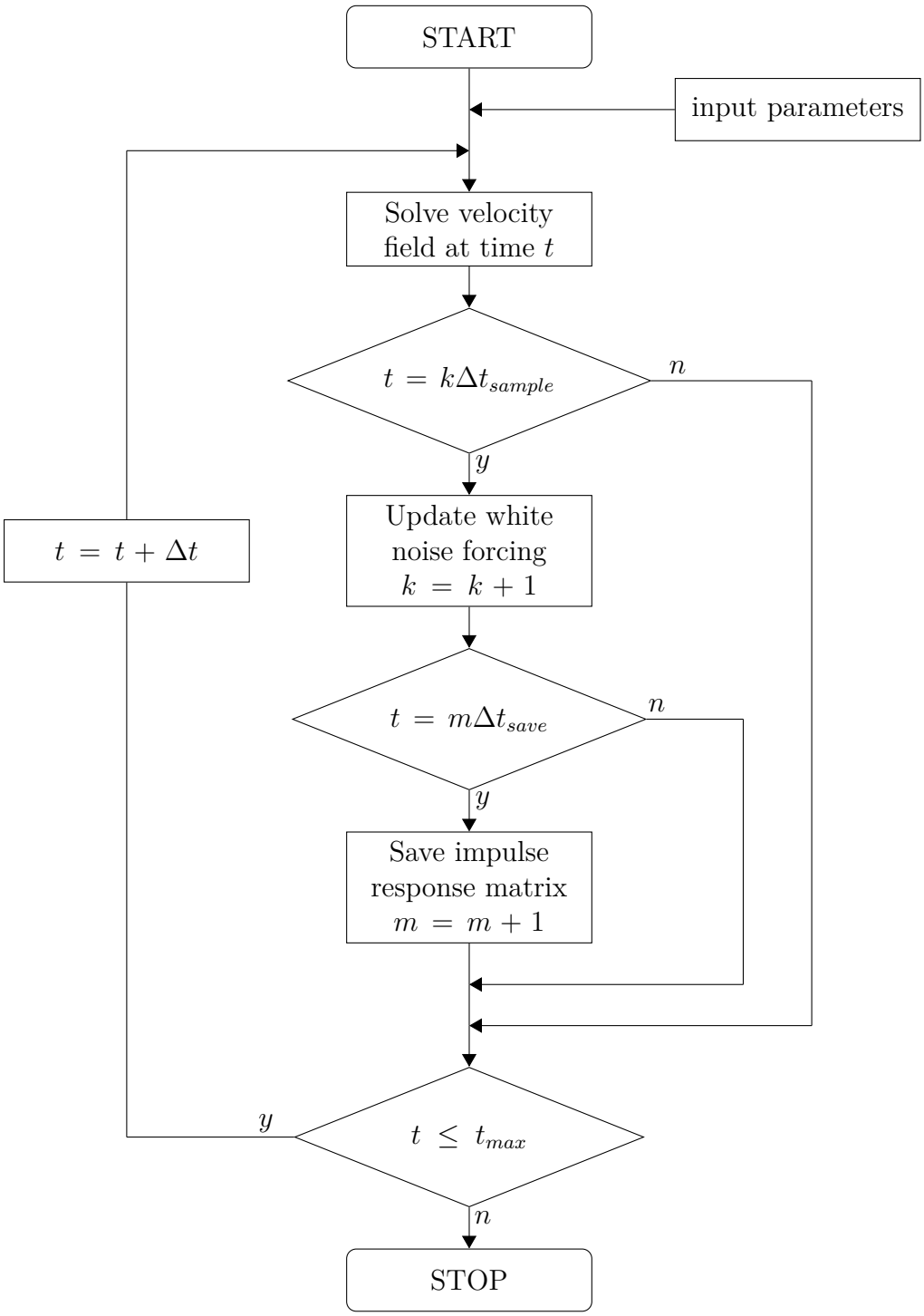


FIGURE 2.1. DNS based measurement flowchart

# 3 | Simulations planning

A complete description of the mean impulse response should require unaffordable investigations among an infinite parameter space. This parameter space is mainly composed by the Reynolds number $Re_\tau$ and the force distance from the wall $\bar{y}$.

The novelty of these response measurement technique, imposes an accurate setting of many other parameters, mainly about the most suitable space-time discretization of the impulse response itself. For these reasons the simulations performed are primarily focused on the wall-normal distances $\bar{y}$ and only two Reynolds numbers are considered, one for the laminar base flow and an other for the turbulent one.

Despite this restriction in the parameters space, the DNS based measurement of $\mathcal{H}_{ij}$ still requires a considerable numerical effort, therefore a careful simulations planning becomes crucial to obtain good results with a reasonable resources expenditure. Given the Reynolds number and the flow typology, the planning concerns mainly the wall-normal distances $\bar{y}$ subdivision and the forcing amplitude $\epsilon_j$.

## 3.1 channel flow parameters

The preliminary step, before computing the impulse response, is the setting of the channel geometry and the base flow.

Computational domain size must be large enough to catch the most extended turbulent structures and, at the same time, to ensure that almost the most relevant part of the impulse response is contained. Furthermore, bigger box dimensions allow to compute low order statistics, such as two-point spatial correlation, with greater accuracy. Despite this, increasing the dimensions, the resolution requirements may lead to critical computational costs.

The box dimensions are the same for both the laminar and the turbulent simulations, while the grid discretization is more finer in the turbulent case.

The space discretization is described by the number of Fourier modes in $nx$ and $nz$, and the number of point $ny$ used for the finite differences. As suggested by literature (*e.g.* Kim *et al.* in [16]) the number of terms in streamwise and spanwise Fourier expansions are set to respect the limits of wall unit resolution, which in this work are set to $\Delta x^+ = 10$ and $\Delta z^+ = 5$. The wall-normal direction needs a more strict resolution of $\Delta y^+ = 0.05$ at wall, and $\Delta y^+ = 4$ at the centerline of the channel, thus the grid has been refined by adopting a non uniform spacing.

In Laminar simulations the initial velocity field is the Poiseuille flow. The flow is driven with a constant mass flux at $Re_B = 1450$, which can be considered, through the turbulent unit scaling, as $Re_\tau = 100$. The choice of a so high Reynolds number, quite at the laminar bound, allows a better likelihood with turbulent simulations, so to exploit the informations obtained in the laminar simulations to set the turbulent ones. Indeed, if the Reynolds numbers was too low, the nonlinear convective terms, so important in turbulent flows and responsible of noise amplifications, would be neglectable.

For the turbulent simulations, instead, the Reynolds number has been raised up to $Re_B = 2280$, which is comparable to $Re_\tau = 150$. This value involves a fully developed turbulent behaviour (*i.e.* with steady statistics) without increasing the computational efforts excessively.

DNS solver proceeds in time with a fixed time step $\Delta t$. This choice implies a variable CFL condition [7] which remains bounded between 0.9 and 1.1. The maximum simulation time deeply depends from the flow nature. For the reasons shown in section 2.2, turbulent simulations require much more time, to reach the impulse response convergence, than laminar ones. This is due to the turbulent velocity fluctuations which must be averaged to make the response emerge. Furthermore, simulation time is inherently related to the forcing amplitude, and consequently to the signal to noise ratio.

Table 3.1 shows the whole list of channel flow parameters.

| | | Laminar | Turbulent |
|---|---|---|---|
| Geometry and Reynolds | $Re_\tau$ | 100 | 150 |
| | $L_x$ | $4\pi$ | $4\pi$ |
| | $L_y$ | 2 | 2 |
| | $L_z$ | $2\pi$ | $2\pi$ |
| Time and space discretization | $nx$ | 64 | 96 |
| | $ny$ | 64 | 100 |
| | $nz$ | 64 | 96 |
| | $\Delta t$ | 0.025 | 0.0125 |
| | $t_{max}$ | 600 | 4200 |

TABLE 3.1. Channel flow parameters used in the laminar and turbulent simulations

## 3.2 Impulse response parameters

The impulse response parameters setting is the most delicate part of this work. The novelty of this work necessitates a preliminary analysis in order to establish the possible truncation criteria. This parameters choice (table 3.2) is strictly related to a complete visualization of the impulse response, for this reason this section anticipate some visualization tools which are presented better further in the next chapter (4).

The route to numerical implementation begins with the discretization definition of the four space-time variable of the impulse response.

$$\hat{\mathcal{H}}_{ij} = \hat{\mathcal{H}}_{ij}(\alpha, y, \beta, t) \tag{3.1}$$

Since the wall-normal distance is a key factor in turbulent flows description, the resolution among the coordinate $y$ is the same of the channel flow: $nyh = ny$, and the grid has the same non-uniform discretization, with a refinement in the region near the wall.

Time resolution, as shown further in section 3.3.2, adopts a variable time step discretization, where each time step is a multiple of the parameter $\Delta t_{sample}$ and the total number of considered time step is $nt_{rsp}$.

The most delicate choice concerns the numbers of Fourier modes to keep in the homogeneous directions. Indeed, from a practical viewpoint, the file dimension of the impulse response array could lead to unaffordable simulation costs for what concerns the memory management. Hence a truncation is needed, so that the wavenumbers space, used for the impulse response description, is a subset of the one used in the channel flow simulation. For

| | | Laminar | Turbulent |
|---|---|---|---|
| Impulse response parameters | $nxh$ | 32 | 22 |
| | $nzh$ | 32 | 34 |
| | $nyh$ | 64 | 100 |
| | $nt_{rsp}$ | 100 | 100 |
| | $\Delta t_{sample}$ | 0.0125 | 0.0125 |
| | $\mathcal{T}_{max}$ | 8 | 8 |

TABLE 3.2. Impulse response parameters used in the laminar and turbulent simulations

example, according to the other parameters chosen, the same wavenumbers space of turbulent channel flow is applied to the response discretization, the memory space required to store the response would be about 6 GB for each one of the three $j$-$th$ components of $H_{ij}$. Consequently without an appropriate truncation the computational cost would be prohibitive.

These numerical consideration brought to a convergence study of the impulse response related to the wavenumbers space extension. This analysis needs the application of well-known mathematical tools. As indicated by Jovanović and Bamieh in [13] the most suitable mathematics operator, which allows to visualize the impulse response information, are the $H_2$ and $H_\infty$ system norms.

### 3.2.1 $H_2$ norm of impulse response

The introduction of $H_2$ norm is needed to eliminate the dependency of the impulse response from the time domain and the $y$ coordinate. In this way our attention can be focused only on the wavenumbers dependency $\alpha$ and $\beta$, which are the object of the convergence analysis related to the truncation need.

The wall-normal coordinate can be eliminated through the following integration

$$\tilde{\mathcal{H}}_{ij}(\alpha,\beta,t;\bar{y}) = \int_{-1}^{1} \hat{\mathcal{H}}_{ij}(\alpha,y,\beta,t;\bar{y})dy \tag{3.2}$$

where the symbol $(\tilde{\cdot})$ states for the new variables space. $H_2$ norm is usually defined for system in the frequency domain (Zhou *et al.* [14]), namely

$$\|\mathcal{H}(\alpha,\beta)\|_2^2 \triangleq \frac{1}{2\pi}\int_{-\infty}^{\infty} \|\tilde{\mathcal{H}}(\alpha,\beta,\omega)\|_{HS}^2 d\omega \tag{3.3}$$

| | complete | truncated |
|---|---|---|
| $nxh$ | 64 | 32 |
| $nzh$ | 64 | 32 |
| $nyh$ | 64 | 64 |
| $nt_{rsp}$ | 100 | 100 |
| $\epsilon_j$ | 0.001 | 0.001 |
| $\bar{y}_q$ | $-0.8685$ | $-0.8685$ |
| $\Delta t_{sample}$ | 0.0125 | 0.0125 |
| $\mathcal{T}_{max}$ | 8 | 8 |

TABLE 3.3. response parameters for the truncation analysis simulations

where $\|\cdot\|$ is the Hilbert-Schmidt norm of an operator defined by

$$\|\mathcal{H}\|_{HS}^2 \triangleq \mathrm{Tr}(\mathcal{H}\mathcal{H}^*) \tag{3.4}$$

Since the impulse response is computed in the time domain, equation 3.3 must be transformed with the Parseval theorem.

$$\|\mathcal{H}(\alpha,\beta)\|_2^2 \triangleq \int_0^\infty \|\tilde{\mathcal{H}}(\alpha,\beta,t)\|_{HS}^2 dt \tag{3.5}$$

From a physical viewpoint, a wavenumbers analysis allows to investigate the impulse response energy repartition among the turbulent scales. Furthermore, this analysis enhances the components of $\hat{\mathcal{H}}_{ij}$, which contain more energy, in other word the components with the greatest influence on the flow behavior. In fluid mechanics literature, $H_2$ norm is also referred to as the ensemble average energy density of the statistical steady state (Farrel and Ioannou [9]). The study of this kind of norm allows to select the appropriate wavenumbers space truncation by considering only the most energetically relevant wavenumbers.

Since turbulent flow requires huge simulation time to compute the impulse response, in this preliminary phase of simulations planning, the energy repartition analysis is performed only for the laminar flow.

In order to compare the different effects that a wavenumbers space truncation could have on the response computation, two laminar simulations are performed. The first one employs the maximum wavenumbers space which is the same of the DNS solver of the channel flow, while the second simulation employs an halved resolution. The response parameters used in each of this two simulation are shown in the table 3.3.

$H_2$ norm of the complete resolution simulation is shown in figure 3.1 for each of the nine components of $\mathcal{H}_{ij}$. The extra diagonal components have

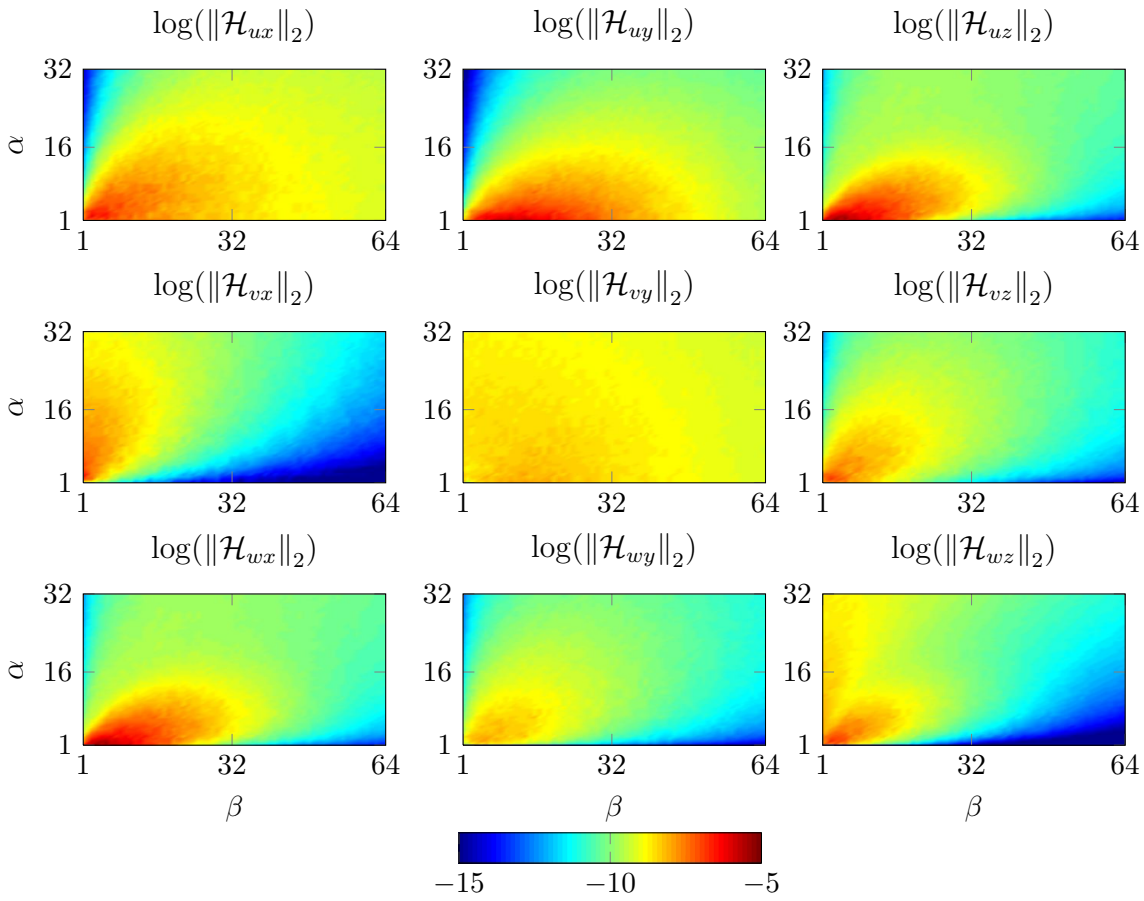


FIGURE 3.1. $H_2$ norm of the impulse response averaged in time and in wall-normal wall-normal distance. The axis are the dimensionless wavenumbers $\alpha = \alpha_0 nxh$ and $\beta = \beta_0 nzh$ with $nxh = 1, \ldots, 64$ and $nzh = 1, \ldots, 64$.

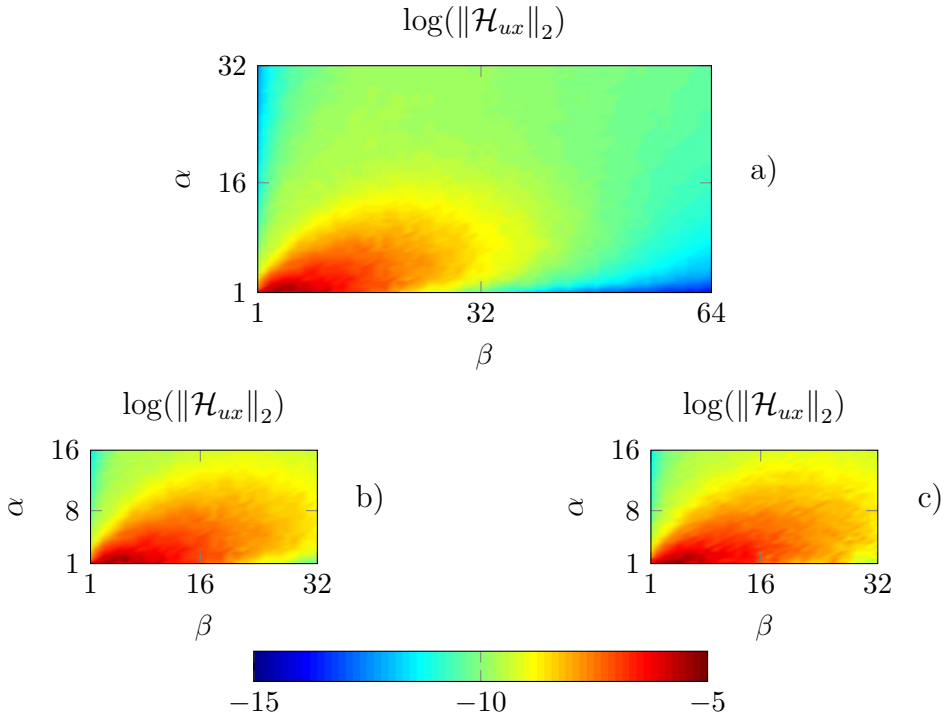


FIGURE 3.2. Comparison between the norm component $\|\mathcal{H}_{uz}\|_2$ of the two simulation in the table 3.3. Figure a) is the norm of the simulation with the complete wavenumbers space, while figure c) corresponds to the reduced simulation. Figure b) is an enlargement of the above figure a), in order to ease the comparison.

a strong concentration of energy at the lowest spatial frequencies. Indeed, as shown in the figure, the differences between the norm values in the low frequency region and in the extreme borders are about four order of magnitude at least. Hence for these components a wavenumbers space truncation can be done without compromise the quality of the results. On the contrary, the diagonal components does not show a clear decay of the energy as the wavenumbers increase. This could lead to incorrect backward transformation from the Fourier domain to the time one. Luckily we are main interested to extra diagonal components behaviour since the diagonal components represent trivial manners to force the fluid.

The physical interpretation of this figure is well examined in the result chapter 4, where a comparison is done also at different wall-normal wall-normal distances.

Interesting consideration about linearity can be done starting from the $H_2$ norm analysis. The response measurement technique is based on the non-

linear Navier–Stokes equation but, as shown further in section 4.1 a linear relationship between input and output is always obtained if a the forcing amplitude is small enough. Flow stability studies (such as those in [33] and [34]) have shown that the linearized Navier–Stokes equations for plane Puoiseuille flow are non-normal. The possible implications of this important results of the fluid dynamics is well discussed in section 4.1, here we are mainly interested to inspect the effects of the truncation on the $H_2$ norm computed with the reduce wavenumbers space simulation. Hence a further analysis is needed to prove that the high wavenumbers, which are truncated, do not affects the reduced wavenumbers space considered in the second simulation of the table 3.3.

Figure 3.2 compares the $H_2$ norm of the component $\mathcal{H}_{uz}$ between the two laminar simulations. No relevant differences appear from the comparison between the full resolution case a) and the reduced resolution one c).

### 3.2.2 Direct convolution

A direct convolution computation can be viewed as an *a posteriori* test to verify the accuracy of the truncated simulation. For this reason a comparison can be done between different velocity fields obtained from two impulse responses with a different wavenumbers space resolution as those in the table 3.3.

The convolution test has been performed with a particular body force shape by assigning directly a given amplitude for each spatial mode of the force. This procedure allows to select precisely the energy repartition among the wavenumbers space of the force, so to excite a specific portion of the wavenumbers space of the response. The chosen testing force acts only on the direction $z$, and has the following time law

$$\hat{\mathfrak{f}}_z(\alpha, \beta, t) = \epsilon_j \sin(pit) \tag{3.6}$$

with $\alpha = 1, 8, 16$ and $\beta = \pm 1, \pm 16, \pm 32$.

In order to have an index of the convolution computation accuracy, figure 3.3 shows the temporal behaviour of the maximum of the output velocity field. The oscillations are due to the particular kind of forcing, and their main period is the comparable to the forcing one. The two curves have quite the same behaviour specially at the beginning where the convolution errors, due to the summation in the time, are small.

The overall good matching of the two curves is a proof that if we aim to compute the impulse response for a control design application, a truncation of the wavenumbers space can be done. Indeed, for this application good

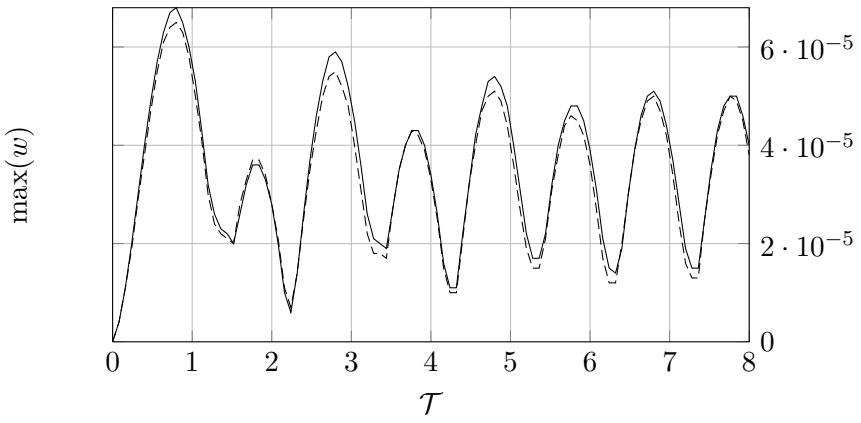


FIGURE 3.3. Maximum of the velocity component $w$ as result of the convolution between $\mathcal{H}_{iz}$ and the test forcing in the equation 3.6. (- - -) is obtained with the complete wavenumbers space response, (——) with the truncated response

results can be achieved only considering the same wavenumbers space for both the response and the forcing.

### 3.2.3 Convergence analysis conclusion

The convergence analysis of impulse response in respect with the wavenumbers space has shown interesting turbulent phenomena which are better explained in the next results chapter. As seen, the wavenumbers truncation has different effects according to the component of $\mathcal{H}_ij$ studied. For the most interesting components, namely the extra diagonal elements ($i \neq j$) the truncation does not affect the result quality too much since a direct convolution with a given forcing shows the same result regardless of the spatial frequencies truncation.

In conclusion the extra diagonal components, the $H_2$ norm analysis shows that a reduced wavenumbers space with $nxh = 32$ and $nzh = 32$ is sufficient to keep into account the most energetically relevant part of the response. This truncation allows a numerical implementation which deeply improve the computational speed. Particularly the memory space required is one fourth of the original one.

The same truncation is applied for the turbulent flow simulations. Since the $y$ coordinate discretization is finer ($ny = 100$) the wavenumbers space truncation has led to the choice of $nxh = 22$ and $nzh = 34$. The numbers of Fourier modes considered for the $z$ direction is higher because of the presence of turbulent structures which are typically elongated in the streamwise direction $x$.

## 3.3 Algorithm modifications

The program employed for the simulations is based on the DNS solver written by Quadrio and Luchini [19], while the response measurement procedure for the *blowing/suction* forcing has been implemented by the same authors and Zuccher in [20]. Subsequently the response measurement procedure has been extended for the body forcing by Pelis and Rampanelli in [28].

For this work, further developments of the program has been done. The main modifications consist in the introduction of a three dimensional forcing and the improvement of the measurement algorithm for a variable time step analysis.

### 3.3.1 Three dimensional forcing

As shown in section 2.4, thanks to the linearity hypothesis one can exploit the superposition principle to compute each of the nine components of $\mathcal{H}$ in the same simulation. Clearly this procedure has the great benefit of avoid the need of three separate simulations, at the price of a little increase in the computational effort for each response update step.

Since the columns of $\mathcal{H}_{ij}$ are independent, a different forcing amplitude can be applied for each direction. This allows to set the forcing amplitude, according to the different signal-noise ratio that may exists among different forcing directions.

Another little step to program efficiency, can be done during the forcing update phase. Instead of an independent white noise generation for each forcing direction, one can use the same random number generation for every forcing components, without compromise the measurement procedure.

### 3.3.2 Variable time step discretization

Impulse response measurement algorithm presented in section 2.3 employs a constant time step resolution. Since the phenomenology of impulse response is more meaningful in the first transient instants, a finer time grid should be preferable at the beginning. An uniform refinement would be unpractical due to the memory requirements, therefore a variable time step represents the most suitable choice.

This algorithm improvement is achieved by applying a variable time step discretization of the correlation equation 2.20. In the numerical implementation of this equation, only the term $\mathcal{F}_j$ contains an explicit time dependency. For this reason this term need to be redefined according to the variable time step law in the following manner.

Given the variable time step law, it is possible to define a map $\mathfrak{T}$, which relate the constant time step index $it$ of $\mathcal{H}_{ij}(i\alpha, iy, i\beta, it)$ with the new variable time step index $it_{var}$ of the forcing history.

$$\mathfrak{T}\colon it \to it_{var} \tag{3.7}$$

Where $it_{var} = 0, 1, 2 \dots N_{history}$, and $N_{history} = t_{maxrsp}/\Delta t_{sample}$ since the forcing history must be update each sample time step. Applying this map the forcing history array must be enlarged till the dimension $N_{history}$. Finally, equation 2.22 can be rewritten in its implementation form

$$\begin{aligned} &\hat{\mathcal{H}}_{ij}^{it_{rsp}}(i\alpha, iy, i\beta, it) = \\ =&\hat{\mathcal{H}}_{ij}^{it_{rsp}-1}(i\alpha, y, i\beta, it) + \hat{u}_i^{it_{rsp}}(i\alpha, iy, i\beta)\mathcal{F}_j^{it_{sample}}(i\alpha, i\beta, \mathfrak{T}(it)) \end{aligned} \tag{3.8}$$

for $it = 0 \dots nt_{sample}$ and for each $i\alpha$, $iy$ and $i\beta$. Variable time step must be a multiple of the constant time step used by the DNS solver.

The $\mathcal{H}_{ij}$ measurement proceeds in the same way as shown before in the time scheme flowchart (figure 2.1). The forcing and the correlation are update at each $\Delta t_{sample}$, but now, the time index of the forcing history selects the forcing values with a variable step.

## 3.4 Wall-normal distances subdivision

As shown in sec 2.1 the DNS based measurement of impulse response, exploits the Dirac delta function properties to apply the body forcing among the wall-normal distance $\bar{y}$, namely

$$\hat{f}_j(\alpha, y, \beta, t) = \hat{\mathfrak{f}}_j(\alpha, \beta, t)\delta(y - \bar{y}) \tag{3.9}$$

Therefore the impulse response has a parametric dependency from the forcing wall-distance, and it is computed for an unique $\bar{y}$ coordinate for each simulation.

Since one of the main aims of this work is the full description of the relationship between the velocity field and body forces, a parametric research among different forcing distance from the wall must be done. This involves the creation of a set of simulations with the related set of forcing wall-normal distances $\bar{\mathcal{Y}}$. In order to reduce the computational efforts, the number of distances considered are a subset of the wall-normal discretization of the channel. This subset is describe in the table 3.4 for the laminar simulations and in the table 3.5 for the turbulent ones. Since turbulent phenomena have stronger effects in the regions near the wall, the wall-normal distances subset

is chosen with a non uniform criterion by thickening the wall region. The number of heights studied is 17 for the laminar case and 20 for the turbulent one.

The particular geometry of the plane channel enjoys a wall-normal symmetry that can be exploited to halve the forcing wall-normal distances required. Indeed, the impulse response computed at a given height $\bar{y}$ above the channel centerline can be used also for the opposite wall-normal distance $-\bar{y}$, namely

$$\hat{\mathcal{H}}_{ij}(\alpha, y, \beta, t; \bar{y}) = \hat{\mathcal{H}}_{ij}(\alpha, -y, \beta, t; -\bar{y}) \tag{3.10}$$

In this way, one can found the whole influence of a generic body force, just applying the forcing in one of the half of the channel.

This wall-normal distances subdivision becomes fundamental if the impulse response is used to compute the velocity field with a direct convolution approach, since a parametric description is needed to apply equation 2.30.

| | sim. $N^\circ$ | height index $q$ | height value $\bar{y}_q$ | amplitude $\epsilon_j$ |
|---|---|---|---|---|
| main simulations | 1 | 1 | $-0.9914$ | 0.001 |
| | 2 | 2 | $-0.9821$ | 0.001 |
| | 3 | 3 | $-0.9718$ | 0.001 |
| | 4 | 4 | $-0.9606$ | 0.001 |
| | 5 | 5 | $-0.9483$ | 0.001 |
| | 6 | 6 | $-0.9350$ | 0.001 |
| | 7 | 7 | $-0.9204$ | |
| | 8 | 8 | $-0.9045$ | 0.001 |
| | 9 | 10 | $-0.8685$ | 0.001 |
| | 10 | 12 | $-0.8263$ | 0.001 |
| | 11 | 14 | $-0.7772$ | 0.001 |
| | 12 | 16 | $-0.7205$ | 0.001 |
| | 13 | 18 | $-0.6557$ | 0.001 |
| | 14 | 20 | $-0.5827$ | 0.001 |
| | 15 | 24 | $-0.4122$ | 0.001 |
| | 16 | 28 | $-0.2124$ | 0.001 |
| | 17 | 32 | 0. | 0.001 |
| linearity test | 18 | 1 | $-0.9914$ | 0.0005 |
| | 19 | 5 | $-0.9483$ | 0.0005 |
| | 20 | 10 | $-0.8685$ | 0.0005 |
| | 21 | 20 | $-0.5827$ | 0.0005 |
| | 22 | 32 | 0 | 0.0005 |
| | 23 | 1 | $-0.9914$ | 0.002 |
| | 24 | 5 | $-0.9483$ | 0.002 |
| | 25 | 10 | $-0.8685$ | 0.002 |
| | 26 | 20 | $-0.5827$ | 0.002 |
| | 27 | 32 | 0 | 0.002 |
| | 28 | 1 | $-0.9914$ | $-0.001$ |

TABLE 3.4. Simulation arrangement for the laminar base flow simulations

| | sim. $N^\circ$ | height index $q$ | height value $\bar{y}_q$ | amplitude $\epsilon_j$ |
|---|---|---|---|---|
| main simulations | 1 | 1 | $-0.9946$ | 0.002 |
| | 2 | 2 | $-0.9889$ | 0.002 |
| | 3 | 3 | $-0.9829$ | 0.002 |
| | 4 | 4 | $-0.9764$ | 0.002 |
| | 5 | 5 | $-0.9697$ | 0.002 |
| | 6 | 6 | $-0.9625$ | 0.001 |
| | 7 | 8 | $-0.9468$ | 0.001 |
| | 8 | 10 | $-0.9293$ | 0.001 |
| | 9 | 12 | $-0.9097$ | 0.001 |
| | 10 | 14 | $-0.8880$ | 0.001 |
| | 11 | 16 | $-0.8638$ | 0.001 |
| | 12 | 18 | $-0.8371$ | 0.001 |
| | 13 | 20 | $-0.8075$ | 0.001 |
| | 14 | 24 | $-0.7395$ | 0.001 |
| | 15 | 28 | $-0.6585$ | 0.001 |
| | 16 | 32 | $-0.5639$ | 0.001 |
| | 17 | 36 | $-0.4560$ | 0.001 |
| | 18 | 40 | $-0.3358$ | 0.001 |
| | 19 | 45 | $-0.1721$ | 0.001 |
| | 20 | 50 | 0 | 0.001 |
| linearity test | 21 | 1 | $-0.9946$ | 0.001 |
| | 22 | 5 | $-0.9697$ | 0.001 |
| | 23 | 10 | $-0.9293$ | 0.0005 |
| | 24 | 20 | $-0.8075$ | 0.0005 |
| | 25 | 50 | 0 | 0.0005 |

TABLE 3.5. Simulation arrangement for the turbulent base flow simulations

## 3.5 Supercomputing organization

Impulse response computation involves a considerable numerical effort for a twofold reason. First of all long simulation times are required. Even if, the method proposed by Luchini, Quadrio and Zuccher in [20] has many computational advantages respect to others methods previously proposed, the velocity fluctuations need to be averaged for a long time in order to make the response emerge. The second reason is related to the parametric wall-normal distances description of $\mathcal{H}_{ij}$ which imposes the creation of many independent simulations, one for each $\bar{y}$ forcing wall-normal distance. Moreover the total number of simulations is increased by the need of a linearity analysis among different forcing amplitudes. As shown in the tables 3.4 and 3.5, these considerations have led to 28 simulations for the laminar flow, and 25 simulations for the turbulent flow.

A group of many independent simulations, as those considered in this work, can perfectly run on a supercomputer architecture. The availability of an huge number of CPU cores allows to investigate every $\bar{y}$ wall-normal distance simultaneously.

The machine used is PLX, which belongs to the Cineca HPC resources, an Italian academic consortium for supercomputing applications. PLX has a structure composed by 274 computing nodes, with 2 esa-core CPUs per node (Intel(R) Xeon(R) E5645 2.40 $GH_z$).

Parallel strategy of the DNS solver presented in the chapter 1 can be exploited successfully on this machine. Indeed, theoretically, both the shared or distributed memory parallelization can be performed. Despite this, only the shared memory parallelization has been used, since the availability of such a number of cores for each CPU make this kind of parallelization the preferable one for practical reasons. Hence a trade-off choice must be done about the numbers of cores used and an efficient usage of the computing resources, namely the total number of computing hours available.

This analysis is performed exploiting the speedup factor, defined as the ratio of the actual wall-clock computing time $t_p$ obtained with $p$ cores, and the wall-clock time $t_1$ required by the same computation on a single core.

$$S(p) = \frac{t_1}{t_p} \tag{3.11}$$

It is well known that the speedup factor grows less than linearly, since the cores spends part of the computational time on communication processes between each other. This speed losses can be token into account by considering the efficiency index $E(p)$ which estimates how well-utilized the cores are in

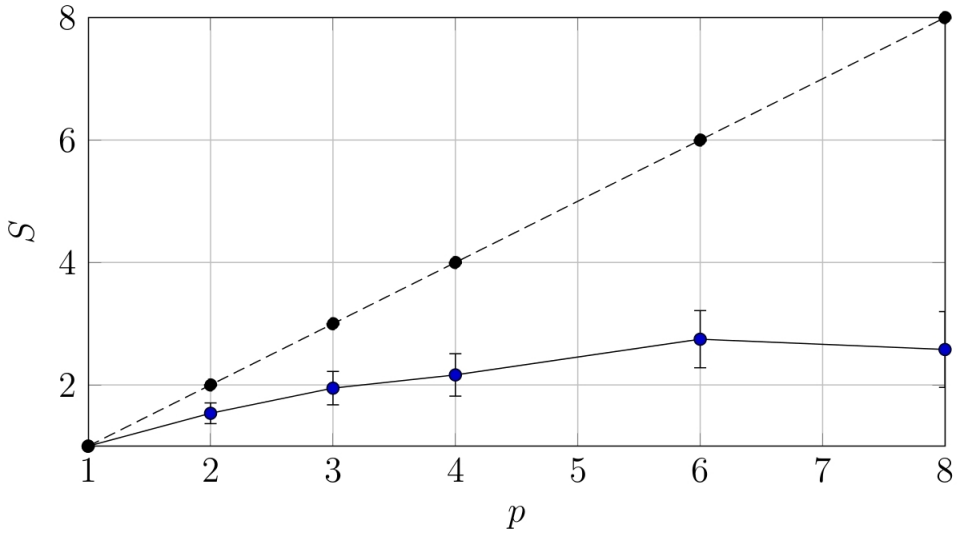


FIGURE 3.4. Measured speedup for shared memory parallelization on PLX machine. (——) is the measured speedup, while (- - -) is the theoretical comparison

solving the problem, compared to how much effort is wasted in communication and synchronization.

$$E(p) = \frac{t_1}{pt_p} = \frac{S(p)}{p} \tag{3.12}$$

The efficiency index is a number typically between zero and one, and can be seen as the percentage of the wall clock time which is actually employed by cores for the computation. The remaining percentage represents the time wasted in communication and synchronization.

Figure 3.4 shows the behaviour of $S(p)$ among the number of cores utilized. The shared memory parallelization doesn't seem to have efficient speedup effects, since its trend is lower than the linear theoretical one. This is confirmed also by the efficiency index $E(p)$ in figure 3.5. Speedup data present a little uncertainty, this is due to PLX batch system which may assign the same computation among cores on different CPUs or nodes. This lead to a little increase in communication times.

In order to exploit the cpu-time resources available with a good compromise between speedup and efficiency, each simulation employs two cores.

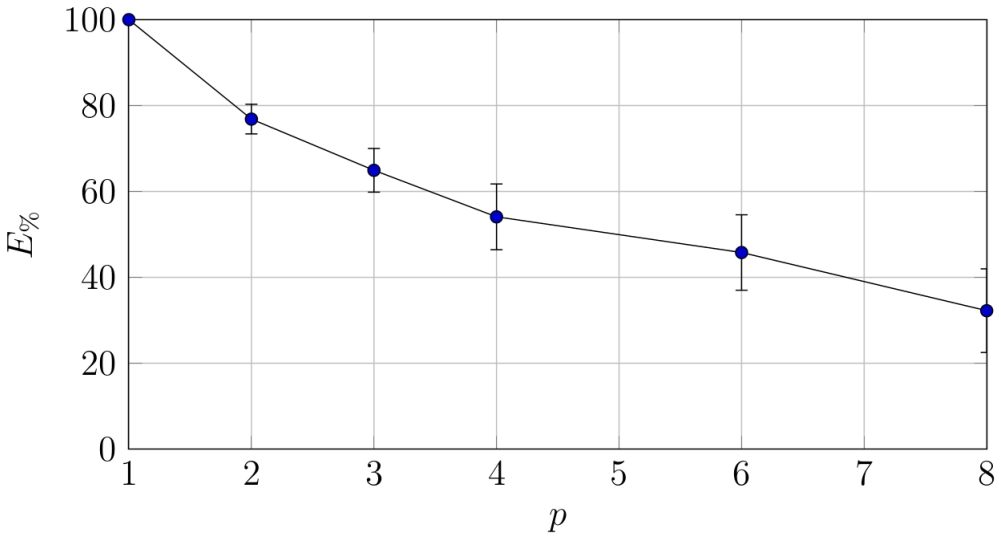


FIGURE 3.5. Measured parallelization efficiency on PLX machine

# 4 | Results

The impulse response in the channel flow presents a phenomenology rich of contents and informations about the behaviour of turbulent flows. This huge amount of informations, requires a patient analysis in order to understand the physical mechanisms at the base.

This chapter presents the numerical result obtained with the DNS based measurement technique previously shown. The first section is dedicated to the linearity analysis to select the correct forcing amplitude. Then Laminar and turbulent flow results are presented. Last section shows the direct convolution results and their comparison with the DNS approach.

## 4.1 Linearity test

The linearity hypothesis is the cornerstone of the impulse response definition. Since the measurement procedure is based directly on the Navier–Stokes equation and not on a linearization (unlike done by Jovanović and Bamieh in [13]), we must ensure that the linearity range is never exceeded. A first linearity test has been done by Luchini, Quadrio and Zuccher in [20] for the wall boundary forcing of the kind *blowing/suction*, finding the correct amplification of the white noise input which give a linearly proportional output. The thesis of Pelis and Rampanelli ([28]) founds the linearity limit for the laminar response but did not investigate the linearity range of the turbulent response. In this work a linearity test is done also for the turbulent simulations so to validate the reliability of the results.

It is important to notice that the choice of the forcing amplitude has remarkable consequences on the maximum simulation time. As shown in section 2.2, the averaging process is done in real time, and requires an huge amount of sample to elide the uncorrelated velocity fluctuation and make emerge the velocity field correlated with the white noise. Hence the signal to noise ratio plays a key role in the computational speed of this process, since a bigger forcing amplitude is able to raise the ratio between the forcing

effects and the spurious velocity fluctuations.

Thus the choice of the forcing amplitude becomes a trade-off between the respect of the linearity range and the maximization of the signal to noise ratio.

For these reason a preliminary test campaign has been done with the laminar base flow, in order to get enough informations about the nonlinear effects of different forcing amplitudes. These informations constitute a good starting point to the selection of a forcing amplitude also for the turbulent flow simulations, since the Reynolds number is not so far from the laminar region.

**Laminar flow**

The laminar linearity analysis has been done among five different forcing heights $\bar{y}$, and for each height three different forcing amplitudes have been tested, namely $\epsilon = \{0.002, 0.001, 0.0005\}$. The complete list of the laminar simulations, done for the linearity analysis, is shown in the previous chapter in the table 3.4.

Among all the nine components of the response $\mathcal{H}_{ij}$ analyzed, the most representative of the linearity analysis is $\mathcal{H}_{uz}$ for the laminar case (and $\mathcal{H}_{vz}$ for the turbulent one), furthermore an extensive presentation for all the components and wall-normal distances is not important in this presentation, since we they present analogous results.

Figure 4.1 shows the different behaviour of the maximum of this laminar response component according to the three forcing amplitude. From the enlarged figures on the right, we can observe that for the first two wall-normal distances the lines of the two higher amplitude (namely $\epsilon = 0.002$ and $\epsilon = 0.001$) are closer each other than the third one. This appends because the third forcing amplitude is smaller and the result is affected by the low signal to noise ratio. This behaviour does not change even if the total simulation time is increased.

From the third to the fifth row of graphics in the figure 4.1 is clear that the linearity limit is reached. The higher amplitude, indeed, shows a definitely different behaviour, while the other two curves are much closer. A possible explanation of this phenomenon lies in the great influence that the wall-distance has to the viscous and non linear term of the Navier–Stokes equation in a plane channel flow. At the lower heights the viscous effects are dominant and the effect of a body perturbation are soon damped, increasing the linearity range. Otherwise, getting closer to the channel center line the dissipation effects decrease and, even if the flow remains laminar, the linearity range is lowered.

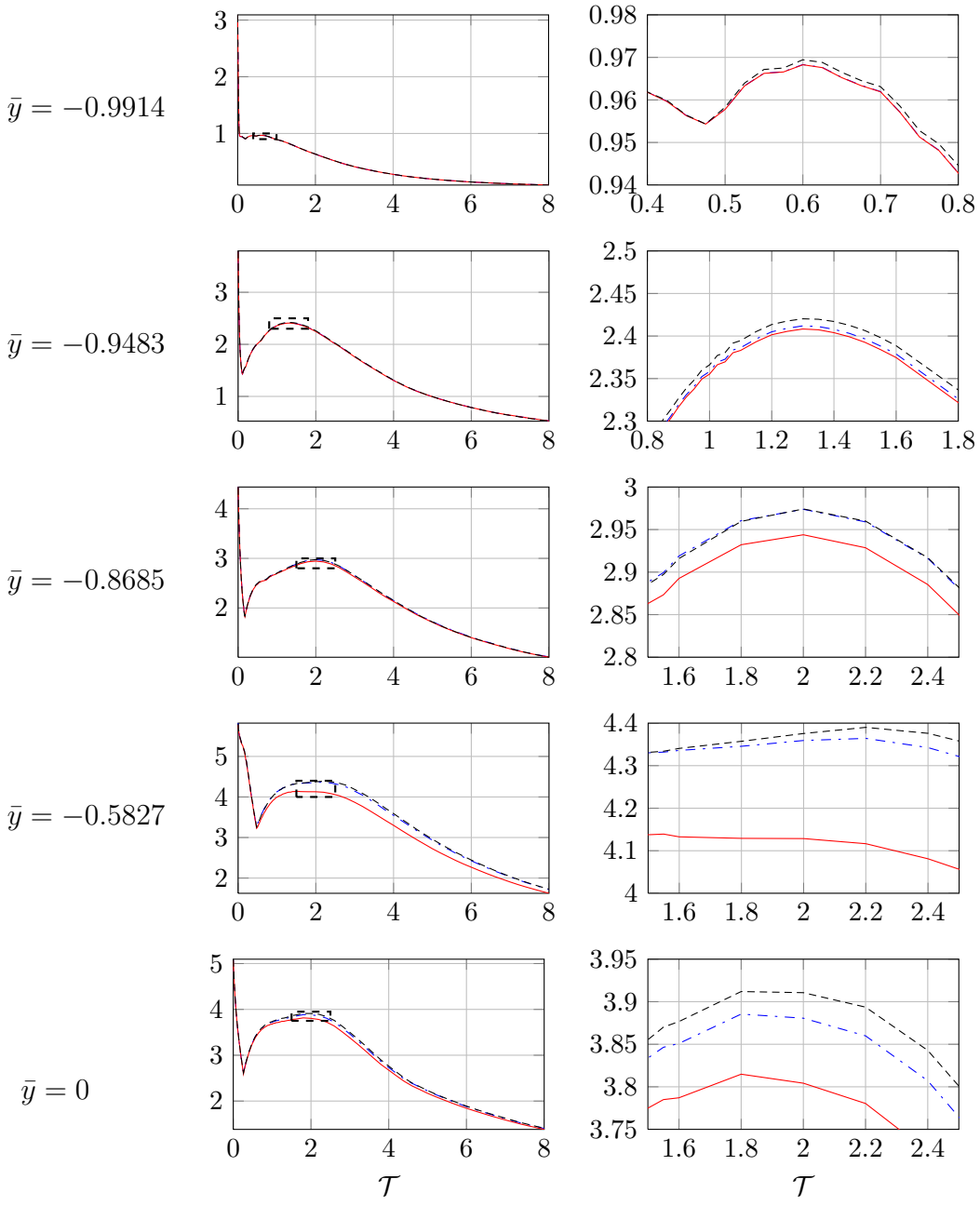


FIGURE 4.1. Variations of $\max(\mathcal{H}_{uz})$ among the time due to different forcing amplitudes. The forcing amplitudes are the following: (——) for $\epsilon = 0.002$, (·-·-) for $\epsilon = 0.001$ and (- - - -) for $\epsilon = 0.0005$. Figures on the right are the enlargement of the ones on the left.

Recalling the equation 2.19 it is important to notice that the body force is computed with a delta-correlated random number generator which is the argument of an exponential function.

$$f_j(\alpha, \beta, n\Delta t_{rsp}) = \epsilon_j e^{i2\pi rand(n\Delta t_{rsp})} \tag{4.1}$$

This implies that the forcing assumes both positive and negative values. Indeed, the linearity test with a negative amplitude done in the last simulation of the table 3.4, showed the same result on the simulation with the positive amplitude.

It is interesting to notice that no relevant differences occurs in the linearity analysis between different forcing directions. Particularly, the three components $\mathcal{H}_{iy}$ due to a forcing in the $y$ direction do not show different linearity behaviours in respect with the other two directions near the wall. Therefore, even if the program allows to set a different amplitude for each forcing direction, in all the simulations in table 3.4 the forcing amplitude is the same for all the components of $\mathcal{H}_{ij}$ and varies just among the wall-normal distances.

### Turbulent flow

The linearity tests with the turbulent base flow are done for five different forcing heights, the complete list of these testing simulation are shown in the previous chapter in the table 3.5. In these turbulent simulations, the linearity range results obtained from the laminar case are initially assumed to be true. Hence the turbulent tests employ the couple of forcing amplitudes which was find to respect the linearity range in laminar simulations. These amplitudes are $\epsilon = 0.002$ and $\epsilon = 0.001$ for the two lower wall-normal distances, and $\epsilon = 0.001$ and $\epsilon = 0.0005$ for the remaining three upper distances.

The results of this linearity test are shown in figure 4.2. This figure shows the behaviour of the maximum in physical space among the time for the response component $\mathcal{H}_{vz}$. The two lines in each figure clearly present different stages of convergence. Indeed the lower forcing amplitudes are less able to elide to spurious velocity fluctuation, this fact underlines the importance to chose the correct signal to noise ratio.

However, if we consider only the deterministic part of these graphics, we can observe that the maximum difference between the curves never exceeds the 3% of the initial maximum value. Hence the linearity hypothesis is verified.

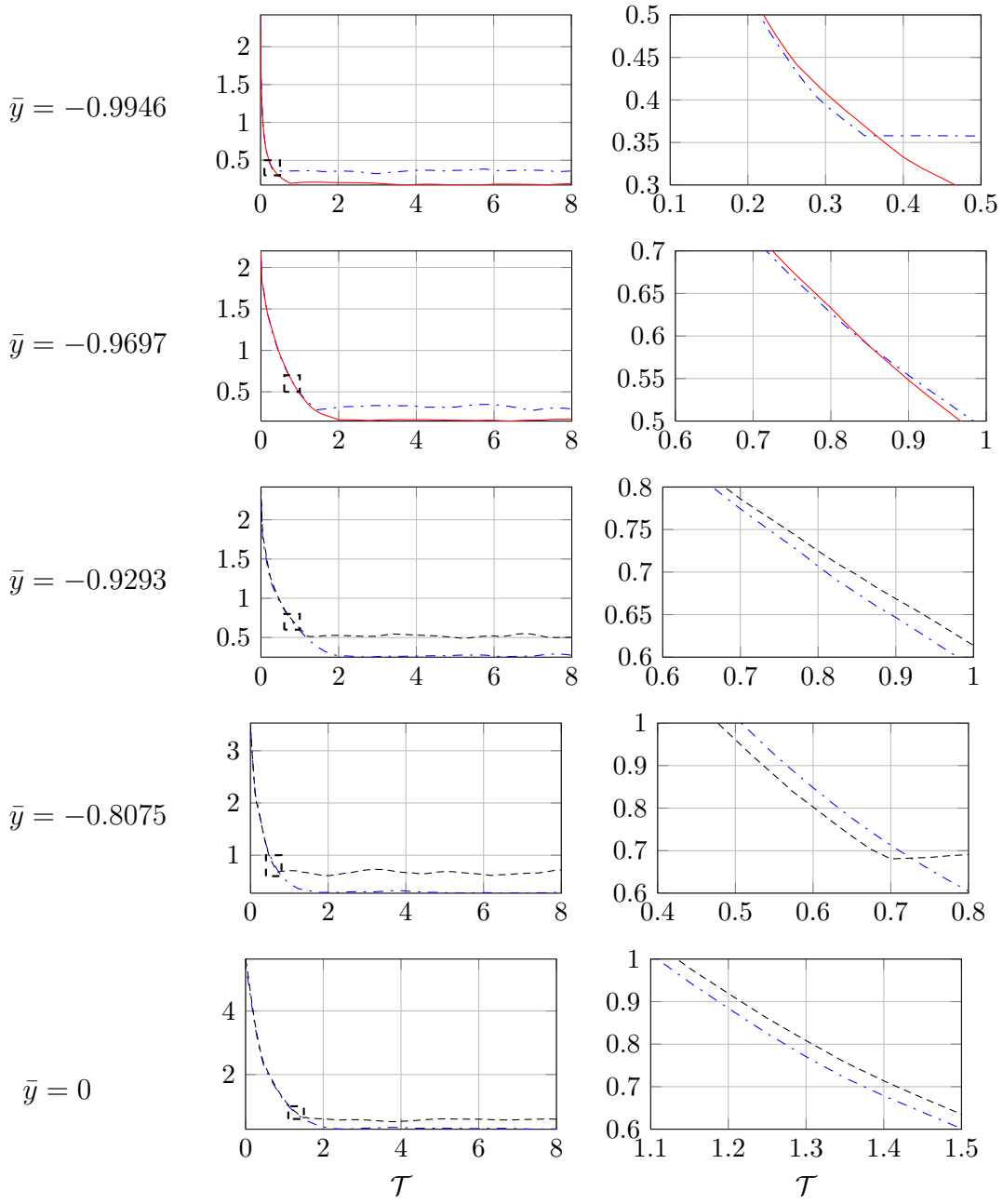


FIGURE 4.2. Variations of $\max(\mathcal{H}_{vz})$ among the time due to different forcing amplitudes. The forcing amplitudes are the following: (——) for $\epsilon = 0.002$, (·-·-) for $\epsilon = 0.001$ and (- - - -) for $\epsilon = 0.0005$. Figures on the right are the enlargement of the ones on the left, (zoom: 20x for the $x$ axis and 10x for the $y$ axis).

## 4.2 Result presentation

This work performs a complete description of the impulse response tensor $\mathcal{H}_{ij}$ in the channel flow by considering also the forcing heights $\bar{y}$. The forcing heights has a great influence on the behaviour and the propagation of a body perturbation. Many considerations can be done by adopting different post processing analyses. As said in the previous chapter the most useful are the following:

- $H_2$ norm in the wavenumbers space
- maximum in the physical space
- isosurfaces of the impulse response

### 4.2.1 $H_2$ norm analysis

This section presents the results obtained with the laminar and turbulent analysis of the $H_2$ norm. As seen in section 3.2.1, this kind of norm has interesting physical meanings, since it is also referred to as the ensemble average energy density of the statistical steady state (Farrel and Ioannou [9]). This mathematical tool leads to interesting consideration about the relationship between the energy repartition in the wavenumbers space and the forcing height.

This analysis can be initially split between laminar and turbulent base flow simulations.

#### laminar flow

Impulse response in laminar flow presents a strong dependency from the forcing height. The analysis with the $H_2$ norm has been done for each forcing height $\bar{y}$, among these, the three most representative are shown in the figures 4.3 (with the forcing at $\bar{y} = -0.9914$), 4.4 ($\bar{y} = -0.9045$) and 4.5 ($\bar{y} = 0$).

These three wall-normal distances are chosen to ease the comparison with the turbulent case, where this distances, as shown further, represents particular wall-normal position of the turbulent mean velocity profile.

It is important to notice that these figures have different logarithmic scale, in particular the $H_2$ norm at the first forcing height available is four order of magnitude smaller than the one obtained by forcing in the channel centerline.

This is an expected result, since we excluded the response computation only for the modal couple $\alpha = \beta = 0$ and not for the various combinations

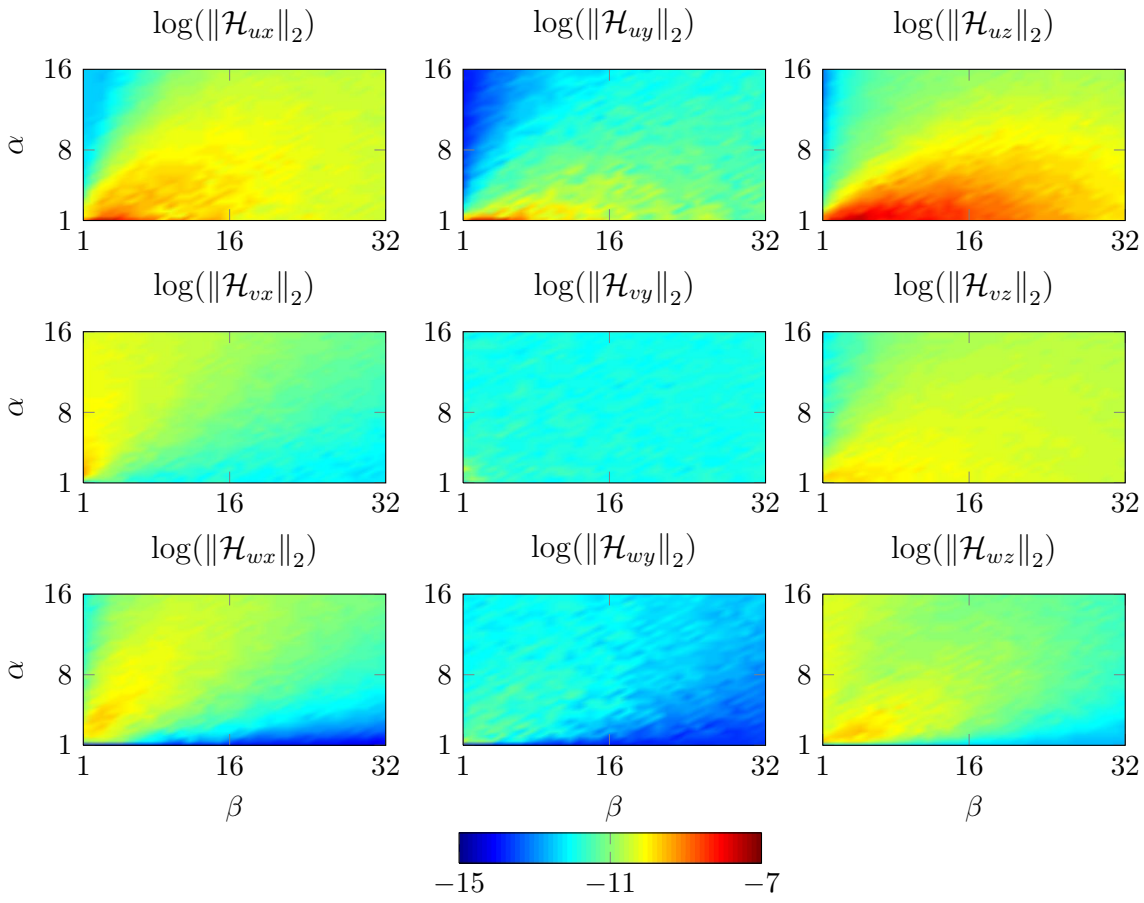


FIGURE 4.3. $H_2$ norm of $\mathcal{H}_{ij}$ for the laminar flow simulation with the forcing input posed at the first available wall-normal distance $\bar{y} = -0.9914$. (height index $q = 1$)

$\alpha = 0$ and $\beta \neq 0$ or $\alpha \neq 0$ and $\beta = 0$. Hence the impulse response feels the effect of the flow transport which grows as we leave the wall.

By observing these three figures, we can see that the components with the highest energetic content are always those ones which are related to the velocity component $u$, and in particular the components $\mathcal{H}_{uy}$ and $\mathcal{H}_{uz}$. Indeed, the maximum values of these two components are at least one order of magnitude higher than the peaks in of the other components especially in the lower forcing heights. These results are in agreement with the literature, such as those ones found by Jovanović and Bamieh in [13].

This implies that the wall normal and the spanwise forcing have a stronger influence on the streamwise component of the velocity. These two compo-

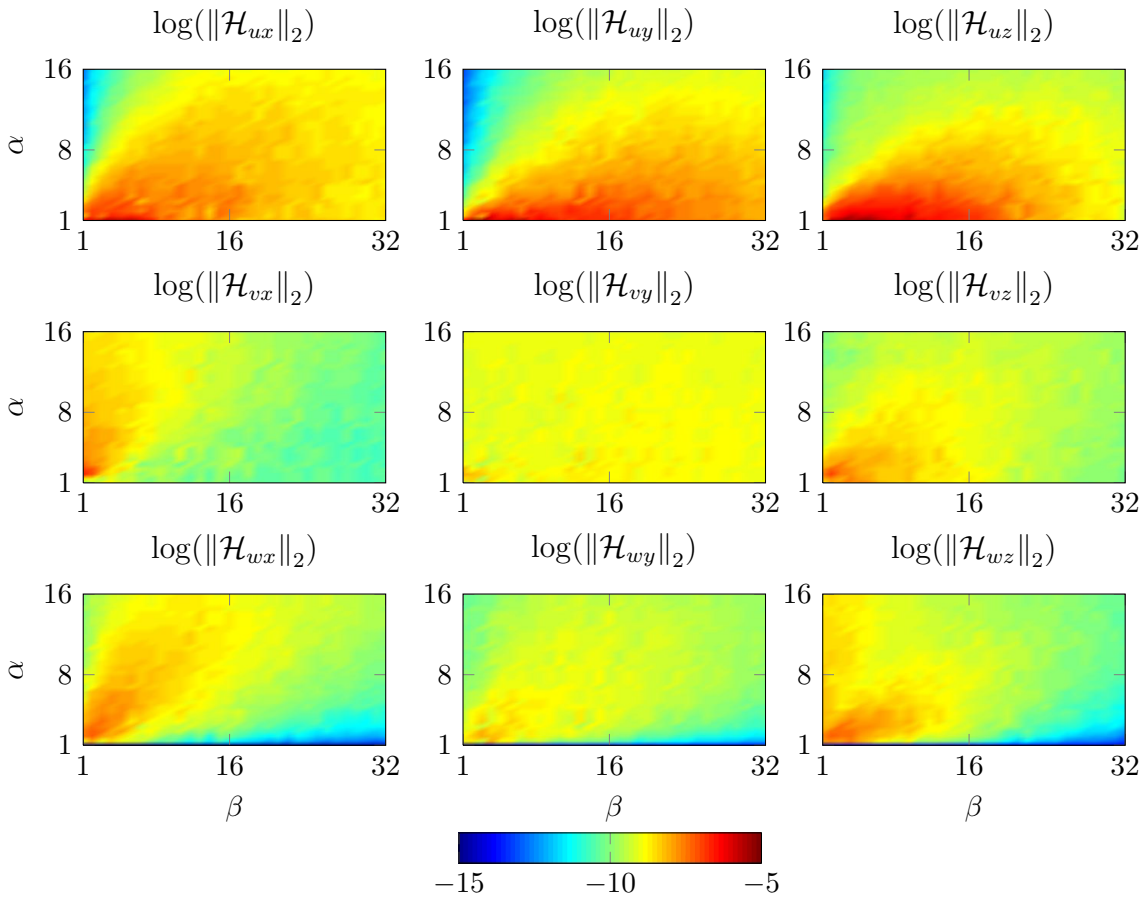


FIGURE 4.4. $H_2$ norm of $\mathcal{H}_{ij}$ for the laminar flow simulation with the forcing input posed at the wall-normal distance $\bar{y} = -0.9045$ (height index $q = 8$).

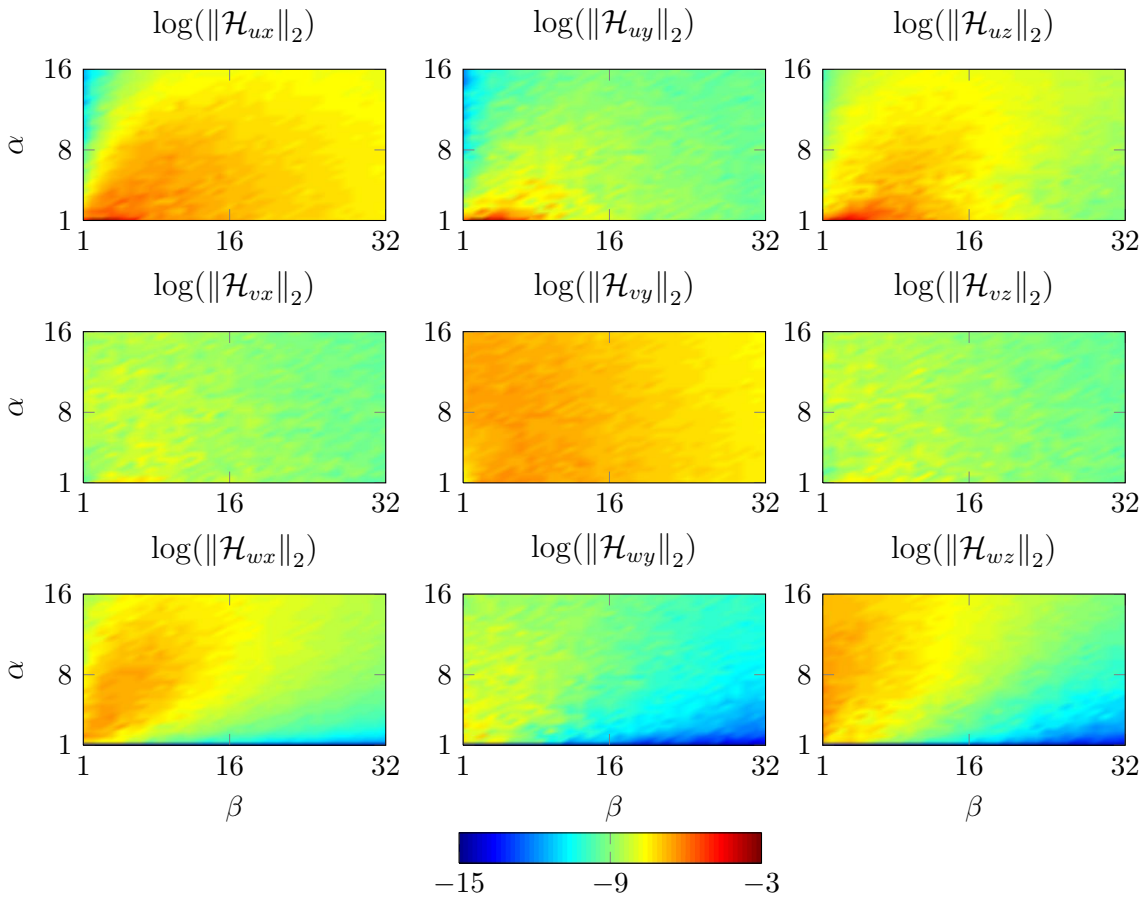


FIGURE 4.5. $H_2$ norm of $\mathcal{H}_{ij}$ for the laminar flow simulation with the forcing input posed at the centerline $\bar{y} = 0$. (height index $q = 32$)

nents also have a similar shape. Indeed both $\mathcal{H}_{uy}$ and $\mathcal{H}_{uy}$ have an energy repartition which is much more distributed among the wavenumber $\beta$ than among $\alpha$. This implies that their representation in the physical space is stretched in the $x$ direction, as confirmed further in figure 4.16, forming the streamwise structures.

The literature result cited in [13] is deepened in this work by the possibility to investigate also the forcing height effects. Some interesting consideration can be done by noticing the behaviour of the wall-normal forcing $\mathcal{H}_{iy}$ among the forcing height. At the first wall-normal height (figure 4.3), the forcing in the $y$ direction has a very small influence on velocity field, especially in the wall-normal and spanwise direction. This influence get higher and higher, as leaving the wall, and becomes one of the most influent.

The components $\mathcal{H}_{vx}$, $\mathcal{H}_{wx}$ and $\mathcal{H}_{wy}$ have a shape which is mainly distributed among the wavenumbers $\alpha$, hence their physical space representation is constituted by structures with spanwise elongated shape. In [13] Jovanović and Bamieh relate this kind of shape to the Tollmien-Schlichting waves. While, always in this paper, the authors relate the components, whose energy in equally distributed in $\alpha$ and $\beta$, to the oblique waves.

From the analysis of these figures we can see that the response components related to the streamwise structures ($\mathcal{H}_{uy}$ and $\mathcal{H}_{uz}$) are much more stronger than the oblique and TS waves. However, as Jovanović and Bamieh suggest, this is not to say that the TS waves and especially the oblique waves should be neglected in the transition mechanisms analysis, since either of them can trigger nonlinear terms if the perturbation are big enough.

The forcing height dependency of the $H_2$ norm is shown more in details in figure 4.6 where six different wall-normal distances $\bar{y}$ are shown. The streamwise structures get stronger and stronger as the wall-normal distance is increased. The strongest effects are reached from $\bar{y} = -0.6557$ on. After this distance the $H_2$ norm peak decreases and the energy distribution in wavenumbers space changes and higher $\alpha$ wavenumber are involved, hence the streamwise structures change and becomes more similar to the oblique waves

In conclusion, for what concerns the laminar flow, the $H_2$ norm analysis points out that the energy content of the streamwise velocity is much bigger than the energy content of the other two velocity components. Remarkable attention deserve the component $\mathcal{H}_{uz}$ which shows the most higher energy content particularly at the first forcing height. Furthermore at the two remaining wall-normal distances the external excitation applied in the wall-normal and spanwise directions have a much bigger impact on the velocity filed than the streamwise direction forcing.

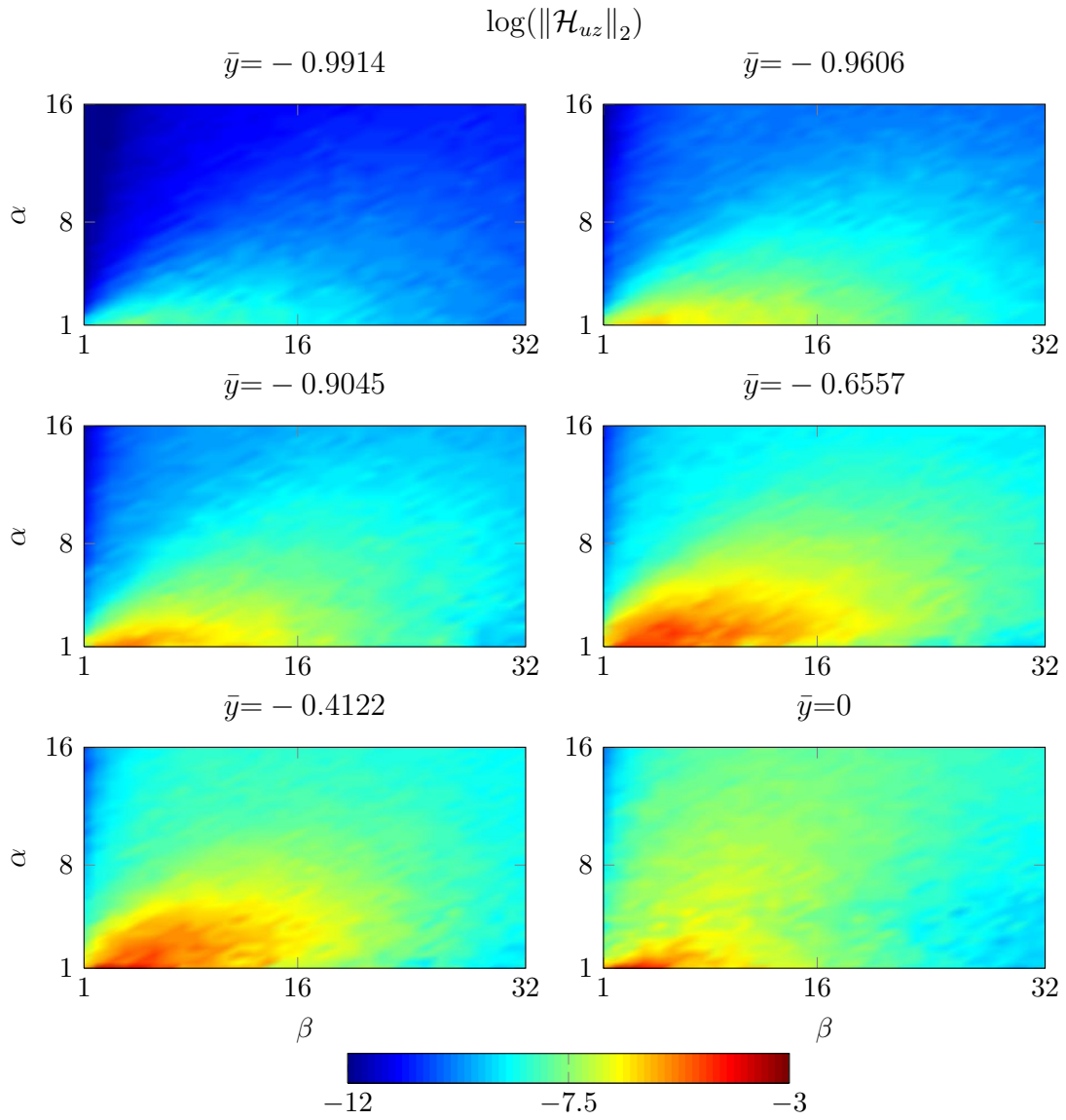


FIGURE 4.6. Deepening about the forcing wall-distance dependency of the $H_2$ norm of $\mathcal{H}_{uz}$. Each graphic is at a different forcing height $\bar{y}$

**turbulent flow**

Turbulent flow dynamics is much more complex than laminar, since its main feature consists in the presence of chaotic motions that make a deterministic approach useless. However the statistics are repeatable and this leads to the computation of the mean impulse response. The mean operation is essential for another reason: the spurious velocity fluctuation are much bigger than the effects of the white noise forcing. Hence the more the velocity field is averaged, the more the impulse response emerges by eliding the uncorrelated velocity noise.

This procedure requires a great simulation time which, unfortunately, exceeds the time given for this work. The maximum dimensionless time reached with the turbulent simulations in the table 3.5 is $t_{max} = 4200$ (table 3.1). Thus, even if the mean impulse response can clearly be detected with visualization in the physical space, a certain level of spurious fluctuation are still present in the velocity filed. For these reason the $H_2$ norm results in the figures 4.7, 4.8 and 4.9 are more noisy than the laminar case.

These figures show the $H_2$ norm of $\mathcal{H}_{ij}$ for three different forcing heights ($\bar{y} = -0.9946$, $\bar{y} = -0.9097$ and $\bar{y} = 0$), which are comparable with the forcing heights of the laminar case figures 4.3, 4.4 and 4.5

These forcing heights are chosen by considering the main properties of the turbulent flow in respect with the wall distance. As known in turbulent flow literature (*e.g.* [29],[16]), the turbulent boundary layer can be divided in different region according to the physical interpretation of the Navier–Stokes equation terms. The first chosen distance lies at the bound of the viscous sublayer ($\bar{y}^+ = 4.54 < 5$), while the second one is in the middle of the buffer layer ($5 < y^+ < 30$), where the velocity fluctuations $\langle uu \rangle$ have their maximum. The third and last wall-normal distance shown is the channel centerline.

The turbulent components shape shows many analogies with the laminar ones previously seen. The most energy relevant components concern again the streamwise velocity, which shows peaks which are at least one order of magnitude higher than the other components.

The response shape of the streamwise components is constituted by structures which are mainly distributed among the wavenumber $\beta$. For this reason the choice of the wavenumbers space truncation for the turbulent flow has been done by considering a discretization among $\beta$ which is finer than the one among $\alpha$.

Otherwise, the wall-normal and the spanwise velocity components have a shape which is distributed more homogeneously in the wavenumbers space. This may suggest the presence of oblique waves structures as denoted in [13]

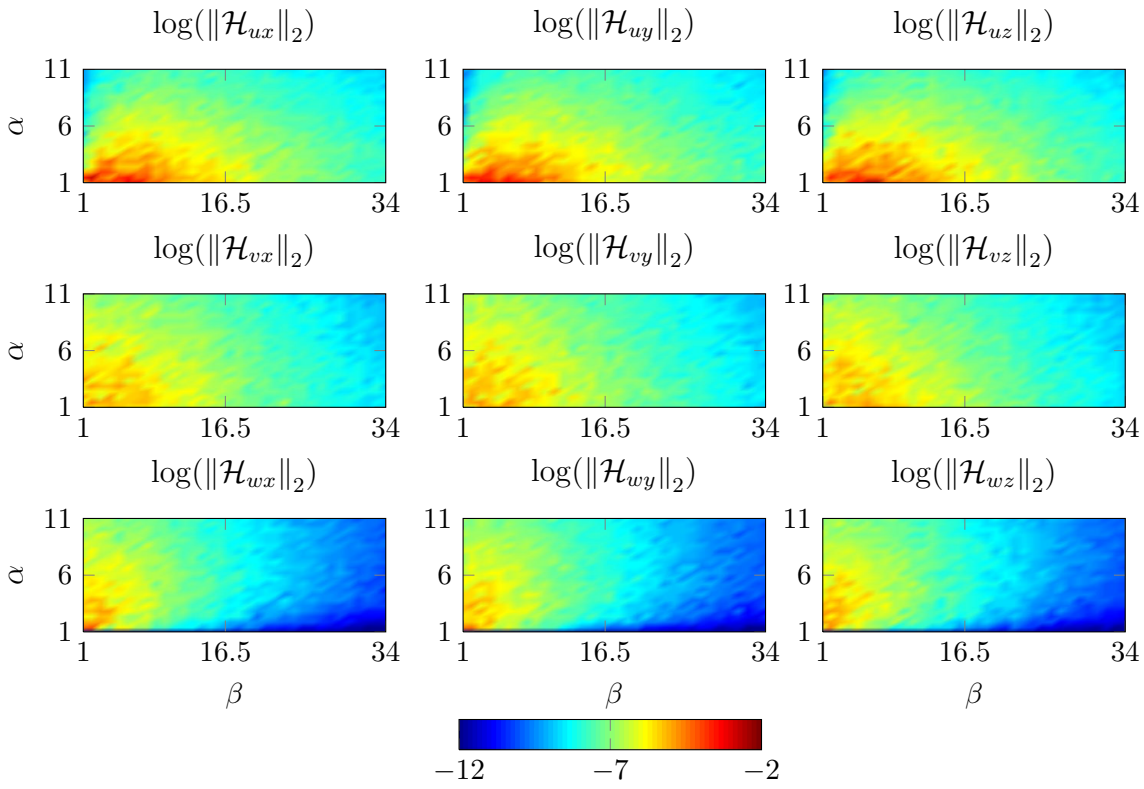


FIGURE 4.7. $H_2$ norm of $\mathcal{H}_{ij}$ for the turbulent flow simulation with the forcing input posed at the first available wall-normal distance $\bar{y} = -0.9946$, $\bar{y}^+ = 0.81$.

for the laminar case.

The forcing distance has a slight effect on the peaks values. The difference between the various distances is less than one order of magnitude for the streamwise velocity components, and a bit more for the other two velocity components.

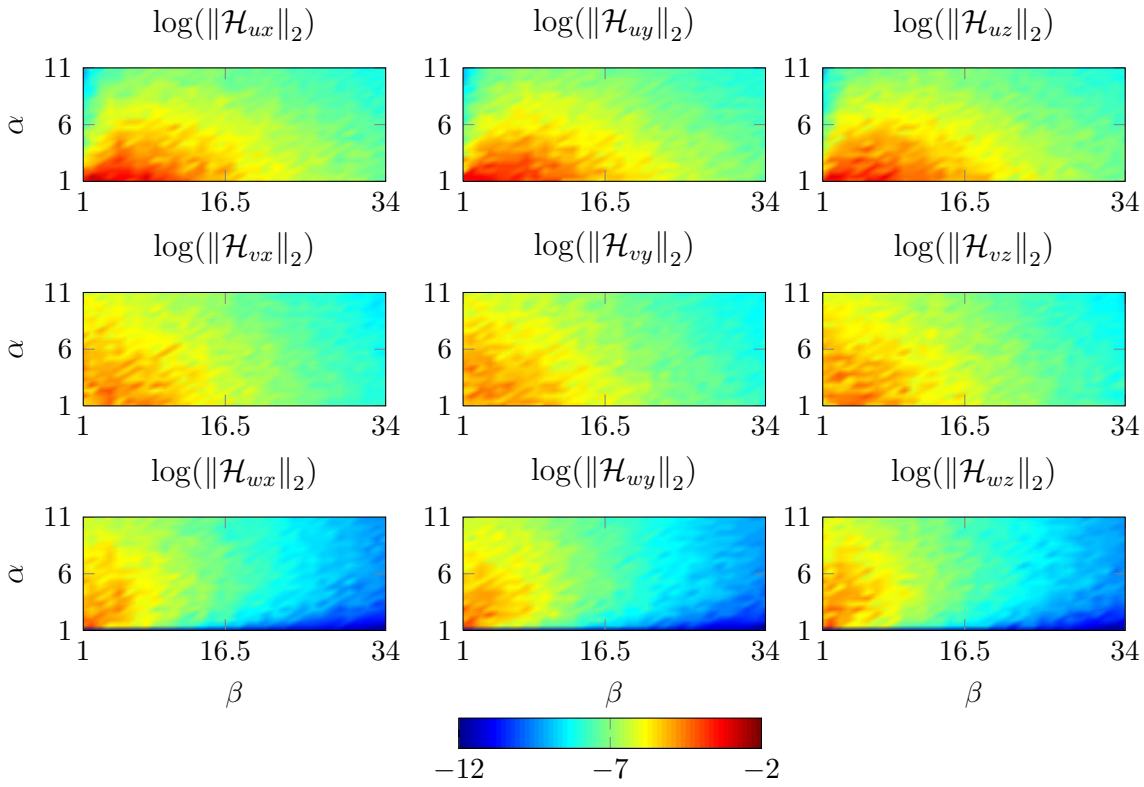


FIGURE 4.8. $H_2$ norm of $\mathcal{H}_{ij}$ for the turbulent flow simulation with the forcing input posed in the buffer layer at the wall-normal distance $\bar{y} = -0.9097$, $\bar{y}^+ = 13.55$.

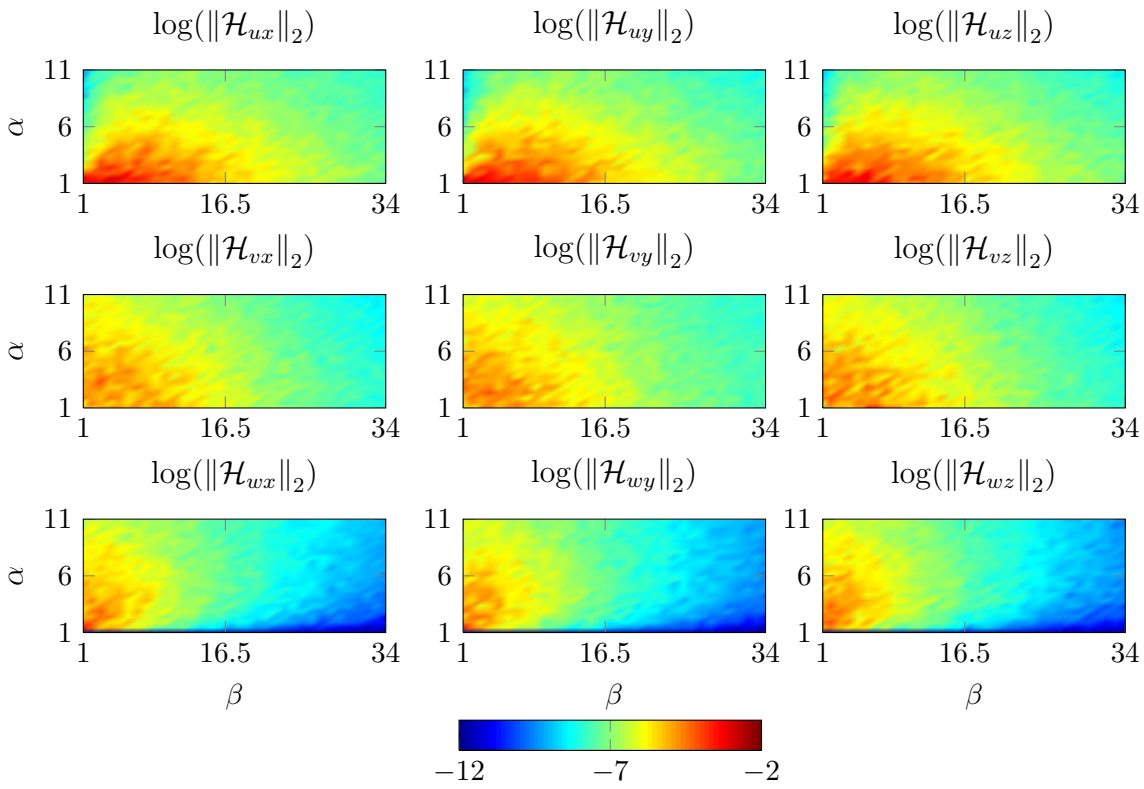


FIGURE 4.9. $H_2$ norm of $\mathcal{H}_{ij}$ for the turbulent flow simulation with the forcing input posed at the channel centerline $\bar{y} = 0$, $\bar{y}^+ = 150$.

### 4.2.2 Spatial maximum and minimum

The impulse response measure presented in [13] by Jovanović and Bamieh is based on a linearization of the Navier–Stokes which is solved in the state space framework. One of the main benefit of the DNS based measurement employed in this work, is the possibility to have a visualization of the impulse response also in the physical space, and not only in the wavenumbers space with the $H_2$ norm computation.

This gives the opportunity to understand the effects, that the body force perturbations have on the flow behaviour, and the mechanisms at the base of the input-output relationship.

Since one of the main purposes of this work concerns the research of the most sensitive components an useful visualization is the maximum among the time of $\mathcal{H}_{ij}$.

The values of $\mathcal{H}_{ij}$ are got dimensionless with the mean velocity since the velocity field, computed by the DNS solver, uses the same scale. The response scaling clearly involves the Reynolds number, but, since the only two Reynolds numbers considered in this work belong to two different flow natures, a numerical approach to the research of the correct scaling is not practicable. Moreover no meaningful scaling is known in literature, hence a purely qualitative comparison is done between laminar and turbulent results. The non dimensional time $\mathcal{T}$ is rescaled with the mean velocity and the channel half-width.

Figures 4.10, 4.11 and 4.12 show the maximums of $\mathcal{H}_{ij}$ for three different forcing distances $\bar{y} = \{-0.99; -0.9; 0\}$.

The maximums behaviour points out that the most influent components are $\mathcal{H}_{ux}$ and $\mathcal{H}_{wz}$. This components show, at every forcing distance, peak values about an order of magnitude higher than the other components. Furthermore also the component $\mathcal{H}_{vy}$ reaches comparable peak values as the forcing distance is increased. This behaviour suggests that the wall influence puts a strong limit to the growth of the motion among the wall-normal direction, while, at the centerline the most intense way to force the fluid is to apply the forcing in same direction of the velocity component which one wants to modify. Hence, where the flow is as more homogeneous as possible the most important components are those on the diagonal $\mathcal{H}_{ii}$. Otherwise if a boundary is present (such as a wall) the components of $\mathcal{H}_{vj}$ are affected by the non penetration boundary condition, and the effects of the body force are lowered.

The forcing distance effects can be related to the velocity fluctuations behaviour among the wall-normal coordinate.

In the figure 4.10 the forcing height is posed in the viscous sublayer where

the dissipative effects associated with the viscous stresses are predominant. This reason can explain why the major part of the maximum behaviours in the figure, decay soon to zero. The response components $\mathcal{H}_{uy}$, $\mathcal{H}_{uz}$ and $\mathcal{H}_{wx}$ clearly show a non monotonic evolution of the maximums with a local growth which can be higher even than the peak at the origin. This phenomenon is explainable recalling the non-normal property of the eigenvectors of the Orr–Sommerfeld's linearized system, as done by Orr in [24] and Schmid in [33]. However this transient growth is not sufficient to bring the system out of the linearity range.

By increasing the forcing distance, we can observe that the transient growth phenomena change their relevance according to the laminar or turbulent nature of the flow. The comparison between figure 4.10 and figure 4.11 shows that for the laminar case the transient growth phenomena get higher as the forcing distance is increased, furthermore at $\bar{y} = -0.90$ the response components, which experience the transient growth, are more than at the lower wall-normal distance $\bar{y} = -0.99$. Otherwise, for the turbulent response tensor, the transient growth is more remarkable at distance $\bar{y} = -0.90$ shown in figure 4.10.

The analysis of maximums points out that the transient growth phenomena reach their peak in the boundary layer region which is situated across the viscous sublayer ($0 < y^+ < 5$) and the buffer layer ($5 < y^+ < 30$). This phenomena occur at lower wall-normal distances in the turbulent case since the higher Reynold number make the viscous layer thiner than the laminar case.

The transient growth effect becomes more and more weak as the forcing height is raised and, by posing the body force at the channel centerline (figure 4.12), the maximums of the impulse response show a monotonic decay for every components both in turbulent and laminar case.

Even if the figures of turbulent maximums show a noisy behaviour in the second half of the time representation, for the computational reason explained before, a stable decaying trend can be supposed both for laminar and turbulent flow. This agrees with the Orszag's results in [25], for which stable linear behaviours can be obtained for linear systems, whose dynamics is governed by the Orr–Sommerfeld's equation, if the Reynold number is below $Re = 5772.22$.

Turbulent response maximums show a decay trend which is faster than laminar, since in turbulent flow the dissipation is higher.

Figure 4.13 shows the behaviour of the minimums of $\mathcal{H}_{ij}$ with the same forcing distance of the figure 4.11 ($\bar{y} = -0.90$). By comparing this two figures, we can observe that the off-diagonal components of the forcing directions $x$ and $z$ present a symmetrical behaviour in respect with the null mean value.

The components $\mathcal{H}_{ux}$ has a non symmetrical maximums and minimums since there is the transport effect due to the mean flow. For what concerns the components related to the wall-normal forcing $\mathcal{H}_{iy}$, the symmetry is present only for the spanwise velocity while the other two components are affected by the presence of the wall.

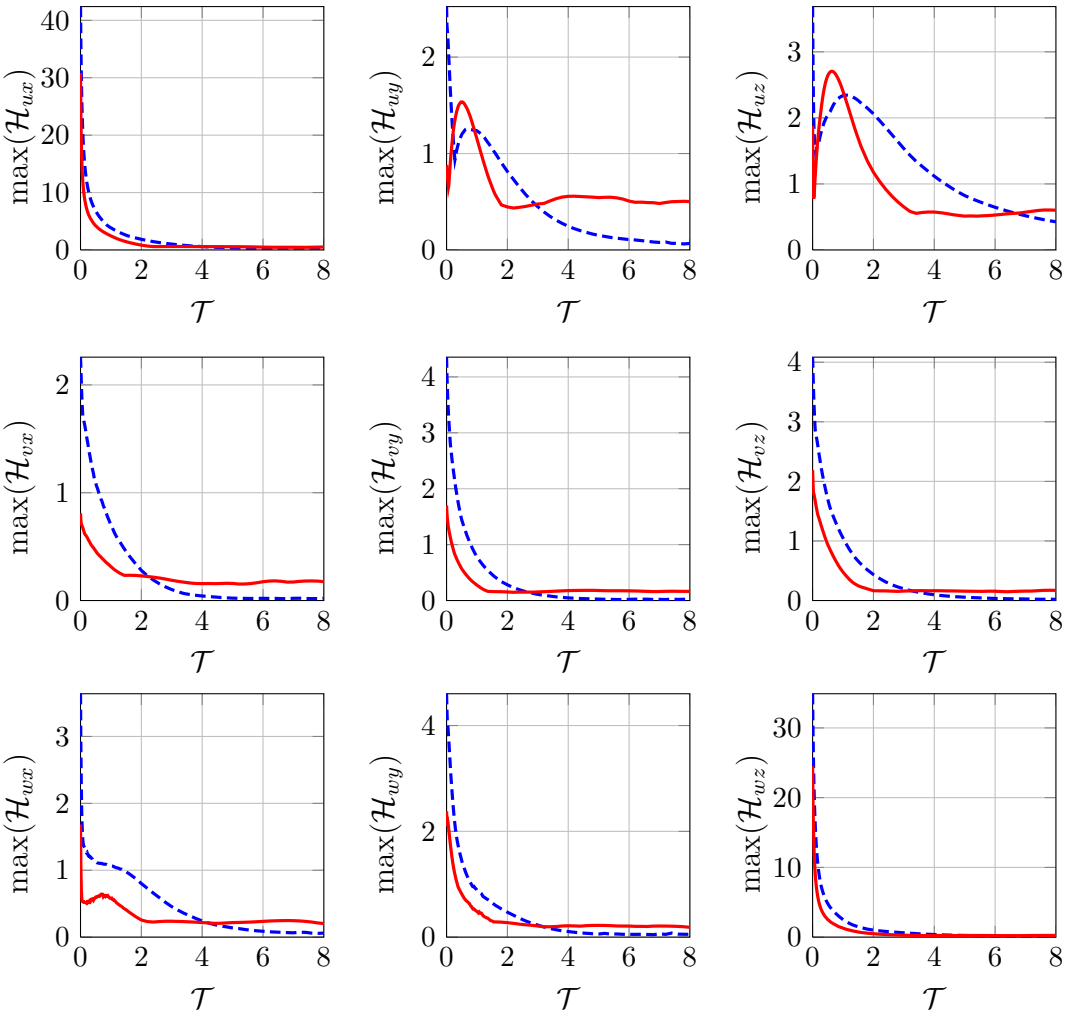


FIGURE 4.10. Comparison between laminar and turbulent maximum of $\mathcal{H}_{ij}$ in the physical space among the non dimensional time $\mathcal{T}$. The forcing is applied at the wall-normal distance $\bar{y} = -0.96$. ((- - -)laminar, (——) turbulent.

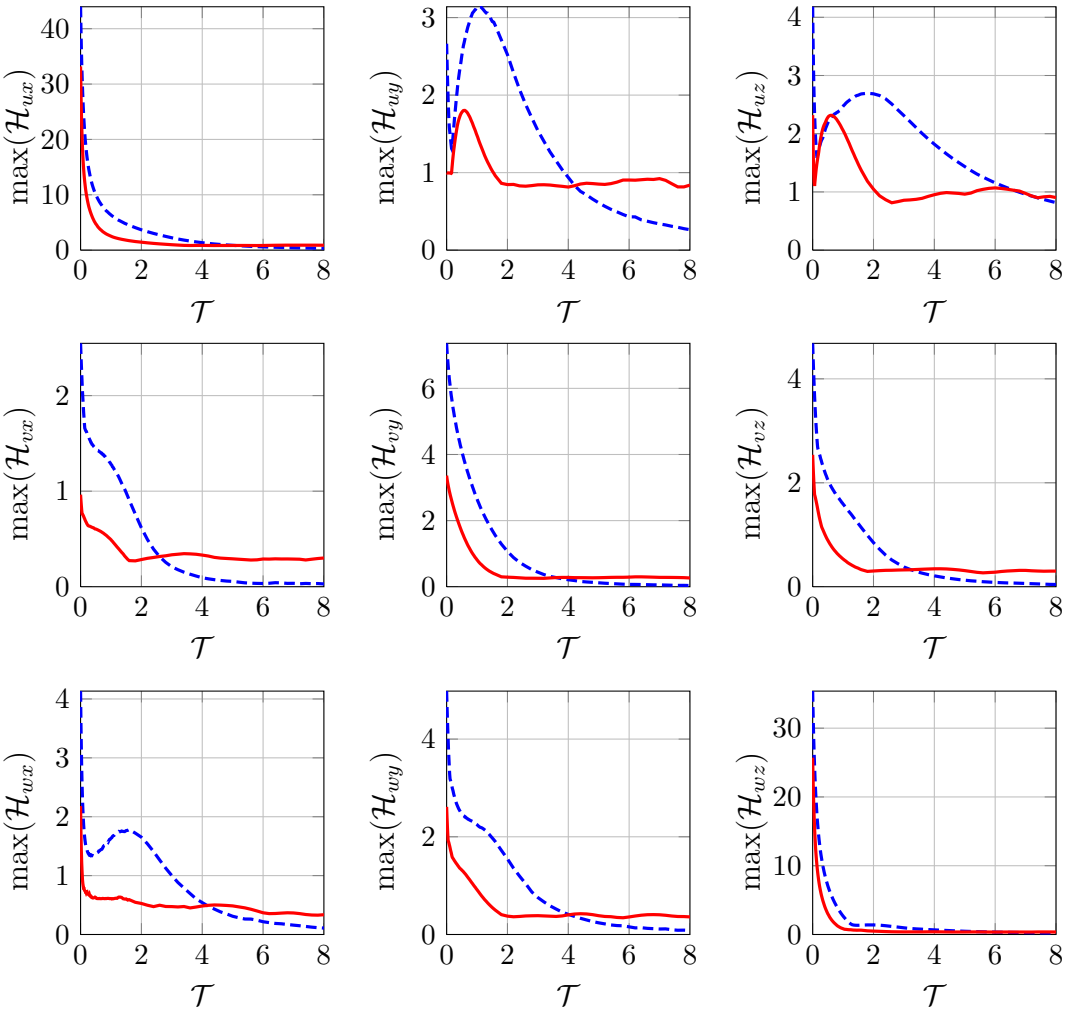


FIGURE 4.11. Comparison between laminar and turbulent maximum of $\mathcal{H}_{ij}$ in the physical space among the non dimensional time $\mathcal{T}$. The forcing is applied at the wall-normal distance $\bar{y} = -0.90$. ((- - -)laminar, (——) turbulent.

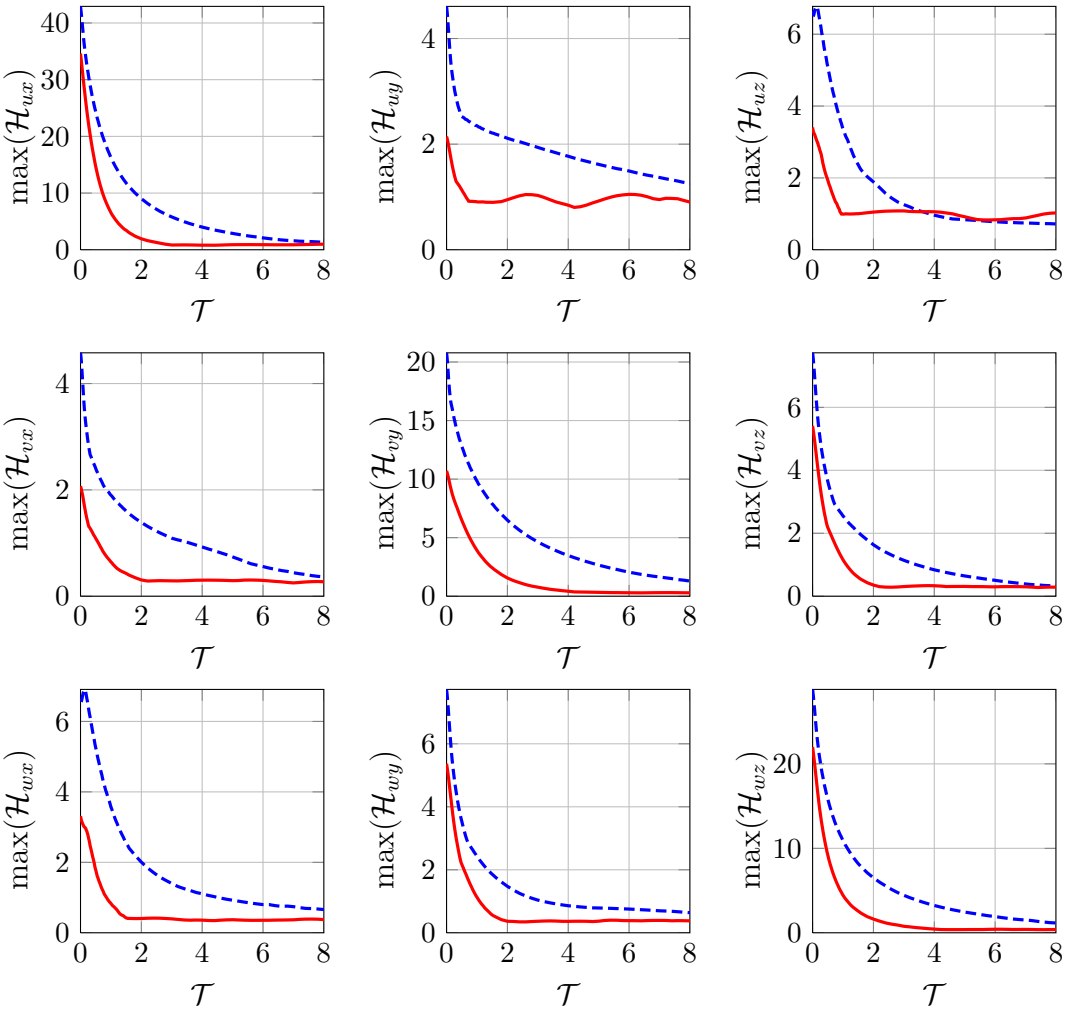


FIGURE 4.12. Comparison between laminar and turbulent maximum of $\mathcal{H}_{ij}$ in the physical space among the non dimensional time $\mathcal{T}$ The forcing is applied at the channel centerline $\bar{y} = 0$. ((- - -)laminar, (——) turbulent.

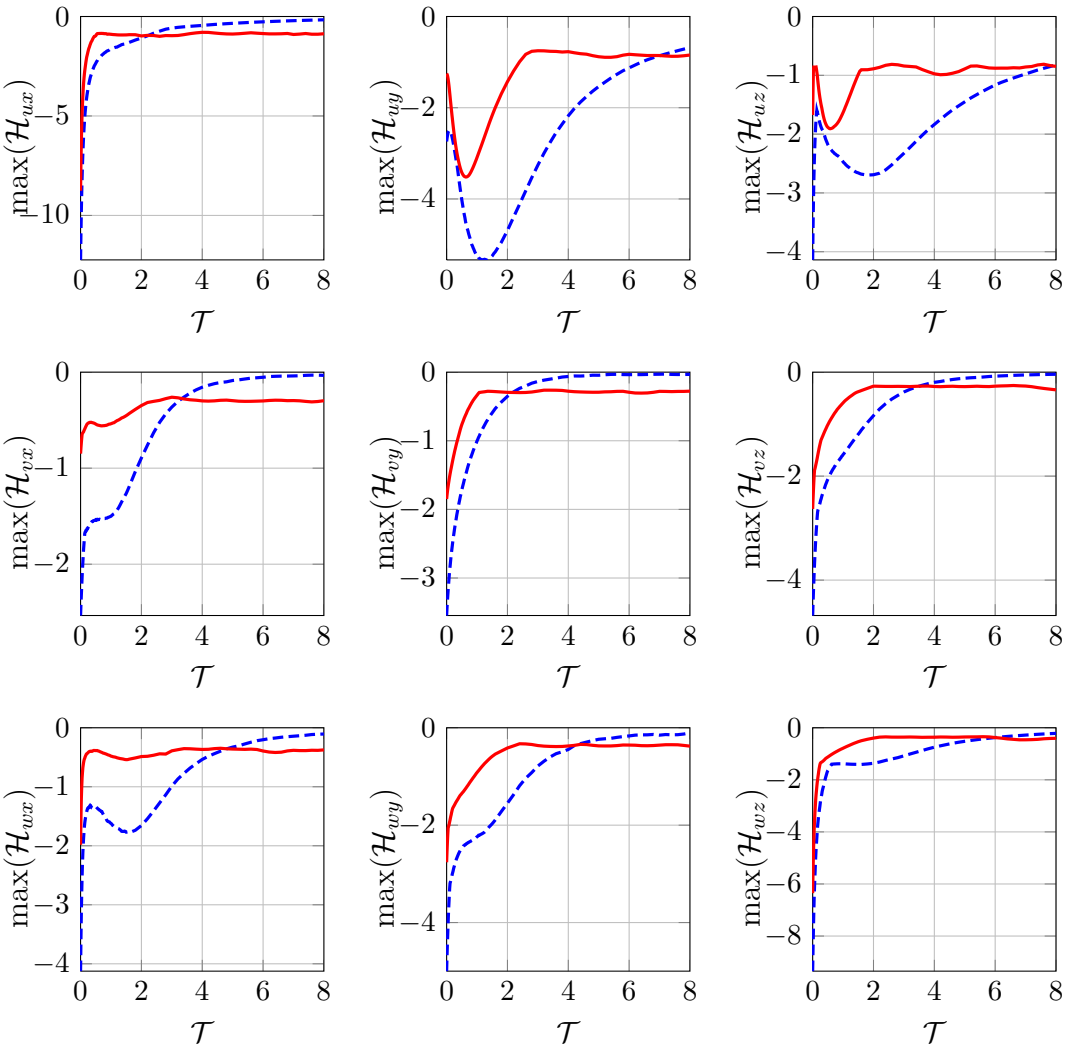


FIGURE 4.13. Comparison between laminar and turbulent minimum of $\mathcal{H}_{ij}$ in the physical space among the non dimensional time $\mathcal{T}$ The forcing is applied at the same wall-normal distance of the figure 4.11 $\bar{y} = -0.90$. ((- - -)laminar, (——) turbulent.

### 4.2.3 Maximum among the forcing distances

The possibility to analyze the impulse response in the physical space, gives the opportunity to find the most suitable forcing distance by studying the maximums behaviour of $\mathcal{H}_{ij}$ among different forcing distances. This analysis is interesting from the viewpoint of a possible design of a control system. Particularly, useful informations can be found for the actuation design strategies.

The maximums behaviour of $\mathcal{H}_{ij}$ among the forcing distances is shown in figure 4.14. The aim of this analysis is to understand why some curves do not show a monotonic trend and how to exploit the curve peaks in a possible control application. However, even if little non monotonic trends are found in some components, the position of the absolute maximums and minimums is quite always at the bounds of the graphics, *i.e.* at the first wall-normal distance near the wall or at the channel centerline.

As previously shown in subsection 4.2.2, the components on the diagonal, which share the same input and output direction, reach the highest peaks. however, the behaviour of the components $\mathcal{H}_{vy}$ is deeply different from the other two one. The wall presence greatly influences the development of the wall-normal direction velocity, the effects of a forcing among $y$ are very small near the wall and strongly increase getting close to the centerline. Indeed, for the turbulent case, the maximum value at the centerline is an order of magnitude higher than the minimum at the wall, and in the laminar case the difference is even higher. The other two diagonal components $\mathcal{H}_{ux}$ and $\mathcal{H}_{wz}$ show little non monotonic trend, but the overall trend of the maximums remains quite constant with the forcing distance.

Many of the off-diagonal components show a little peak near the wall both in the laminar and in turbulent case. This peak is related to the maximum position among the time, which can be either at the initial time or generally not more further as a transient growth peak. For example, for what concerns the component $\mathcal{H}_{uz}$, the near wall maximum in figure 4.14 is related to the transient growth peaks which can be easily detected in figure 4.10 and 4.11, while, as the forcing distance is increased, the curves in figure 4.14 are related to the initial maximum of figure 4.12. Another example is the component $\mathcal{H}_{uy}$, which has a little peak quite at the quarter of height of the channel. Also this peak is due to the transient growth visible at the in figure 4.10 and 4.11.

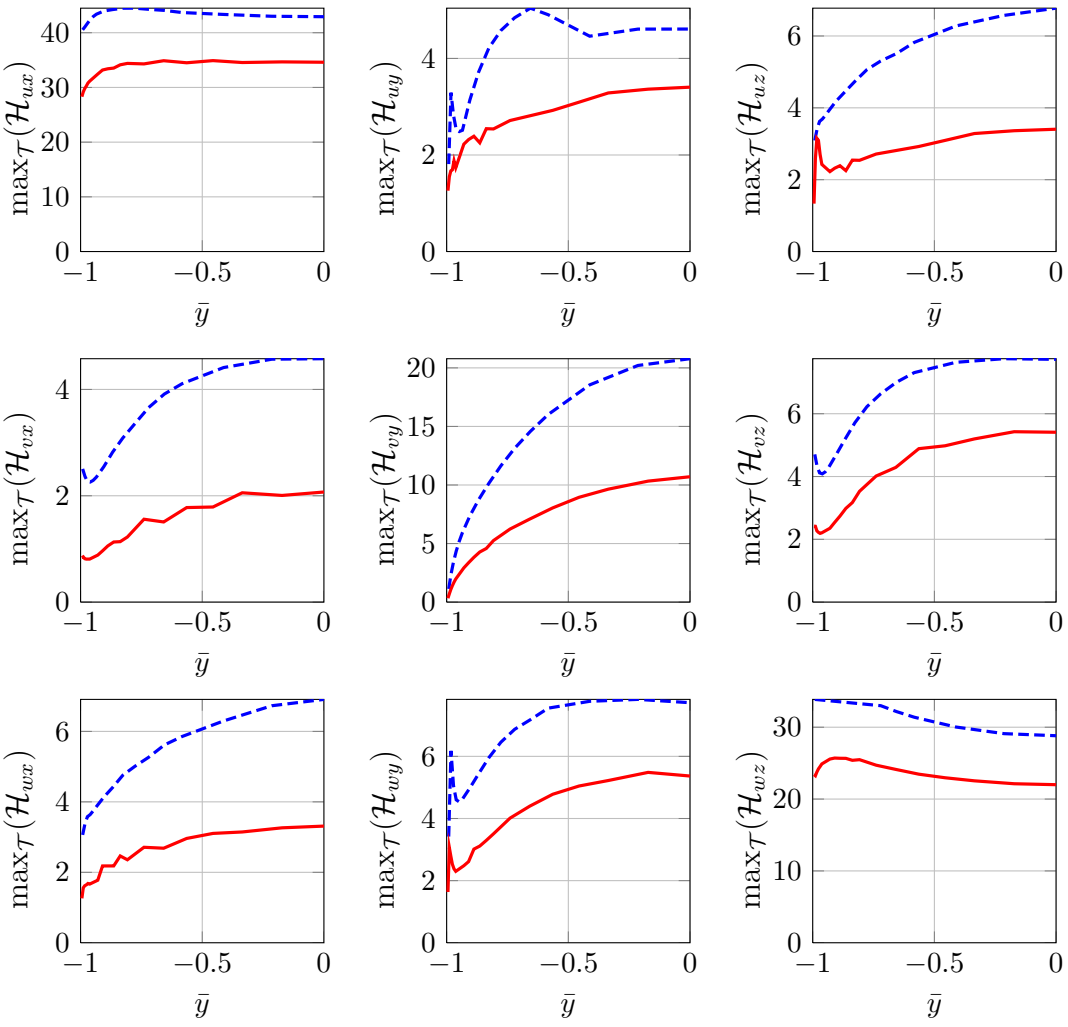


FIGURE 4.14. Maximum in the physical space among different forcing distances.

### 4.2.4 Isosurfaces of $\mathcal{H}_{ij}$ among the forcing distances

The mechanisms, with whom the body forcing interacts with the flow dynamics, can be pointed out with the aid of a visualization of the velocity isosurfaces in the physical space. The three dimensional representation of the response allows to have an immediate view, about the effects of different forcing direction and distances. Since the computational domain is much extended, a reduction is needed to make the visualization more suitable (figure 4.15).

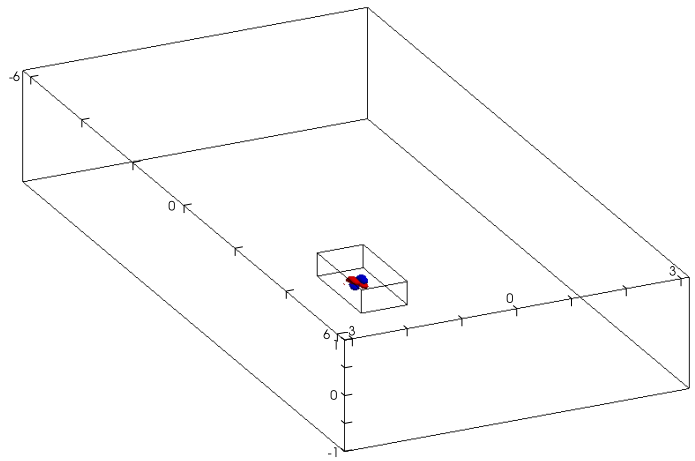


FIGURE 4.15. Comparison between the computational domain and the reduced visualization domain used in figures 4.16, 4.17 and 4.18. Figure 4.19 used a reduced box elevated around the channel centerline.

The isosurface visualization are realized at the dimensionless time $\mathcal{T} = 0.5$, since at this time the maximums of the turbulent response, previously shown in subsection 4.2.2, have an interesting local peak. Four figures are presented about the isosurfaces analysis. The first one 4.16 concerns the laminar response obtained with the forcing distance at $\bar{y} = -0.9045$. The other three figures (4.17, 4.18 and 4.19) treat the turbulent response for the same distances used in the subsection 4.2.2.

The values of the isosurface are as equal as possible among the different components of $\mathcal{H}_{ij}$, so to allows a comparison between them. In the laminar case, the isosurfaces are obtained at the value $\pm 1$, while the turbulent isosurfaces are obtained with the value $\pm 1$ for the components on the diagonal, and $\pm 0.5$ for the remaining components (in few cases the value $\pm 0.25$ is used, since certain components reach smaller values).

The flow phenomena that act on the evolution dynamics of the isosurface are mainly two. The first is the transport due to the mean velocity profile, while the second is the viscous diffusion. The nonlinear convective terms of the Navier–Stokes equations 1.8 are neglectable, since the linearity hypothesis is respected. Hence the shape of the isosurfaces are mainly due to the two cited mechanisms. The effects of the transport concern the slower advancing velocity of the structures next to the wall. The effects of the diffusion exhibit themselves in the decrease of the total extension of the isosurface and by diffusing the effects of the forcing in the closeness of the applying point of the force.

Several changing can be detected between each component of $\mathcal{H}_{ij}$ according to the forcing distance and the flow nature. However, certain mechanisms of interaction, between the body force and the velocity field, appear frequently. A possible way to classify each component behaviour, consists in the identification of the main vorticity component, that arises from each interaction.

Before proceeding with the presentation of the numerical result of the figures with the isosurfaces, it must be noticed that, the lacking of a scaling of the impulse response among different Reynolds number, make impossible a quantitative comparison between the laminar and the turbulent case. Hence the laminar isosurfaces in figure 4.16 can be compared, with the turbulent ones, just from a qualitative viewpoint.

A first analysis can be done about the growth of a spanwise vorticity. This is the case of the component $\mathcal{H}_{vx}$, where a positive isosurface, in the wall-normal direction, is followed by a negative one, creating a positive spanwise vorticity (figure 4.17). This behaviour is present both in the laminar and in the turbulent case. Interesting effects are found for this component by forcing at the channel centerline, where two extra isosurface appear above the channel centerline with an inverted velocity direction. This leads to the creation of two saddle points at the centerline, one between each isosurface and its relative opposite one. The positive streamwise velocity between these two saddle points must be positive to respect the mass conservation and, indeed, the component $\mathcal{H}_{vx}$ is formed by one big isosurface of positive velocity which starts from the rear saddle point and goes into the front one. Also the component $\mathcal{H}_{wx}$ has a shape that validates this flow reconstruction.

The development of this interaction mechanism (about the streamwise forcing) is common for both the laminar and turbulent case. Simple sketches of these interaction mechanisms are shown in figure 4.20 for each of the three forcing directions. It is interesting to notice that the velocity components, which are different from the forcing direction, have the same behaviour at the saddle points, they are always both inward or outward. While the ve-

locity component, in same direction of the forcing, has always an opposite sign in respect to the other two components. Hence this kind of interaction satisfies the mass conservation principle. Furthermore each sketch in figure 4.20 is equal to the other two except for a rigid rotation. The only changes concern the effect of the transport velocity and the diffusion which must vary among the forcing distances and the Reynolds numbers (*e.g.* the turbulent isosurfaces have a more stretched shape due to the higher transport velocity).

We must notice that this kind of interaction mechanism is more evident in the figure 4.19, where the forcing distance is posed at the channel centerline. As we get close to the wall, this mechanism is affected by the wall locking and becomes weaker and weaker, furthermore for the wall-normal forcing case this interaction mechanism vanishes near the wall and we need another physical interpretation.

A similar interaction mechanism occurs also for the forcing in the spanwise direction. Starting from the component $\mathcal{H}_{wz}$ we can identify two possible saddle point at the right and at the left of the main positive isosurface which can justify the growth of a contra-rotating wall-normal vorticity for the component $\mathcal{H}_{uz}$ and a contra-rotating streamwise vorticity for the component $\mathcal{H}_{vz}$. For this forcing direction the forcing distance has strongly influences the behaviour of the component $\mathcal{H}_{uz}$. Indeed the interaction mechanism in figure for the forcing distance $\bar{y} = -0.9697$ (4.17), mainly concerns the development of only two isosurfaces, while increasing the forcing distance (like in figures 4.18 and 4.19) other two opposite isosurface appear between the first ones and the wall. This means that near the wall the interaction mechanism between the spanwise forcing and the streamwise velocity assumes a shape which is less three dimensional than at higher forcing distances.

The effects of the wall-normal forcing near the wall ($\mathcal{H}_{iy}$) have a more complex physical interpretation, since the presence of the wall, greatly influences the interaction mechanisms. From the component $\mathcal{H}_{vy}$ shown in figure 4.17 and 4.18, we can see that a wall-normal forcing creates a relatively big region of positive (upward) wall-normal velocity bounded by two smaller negative region. This leads to the creation of two contra-rotating regions of streamwise vorticity. An analogous behaviour acts on the streamwise velocity and a wall-normal vorticity is established. It is interesting to notice that the main streamwise velocity isosurface has a backward direction in respect with the mean velocity.

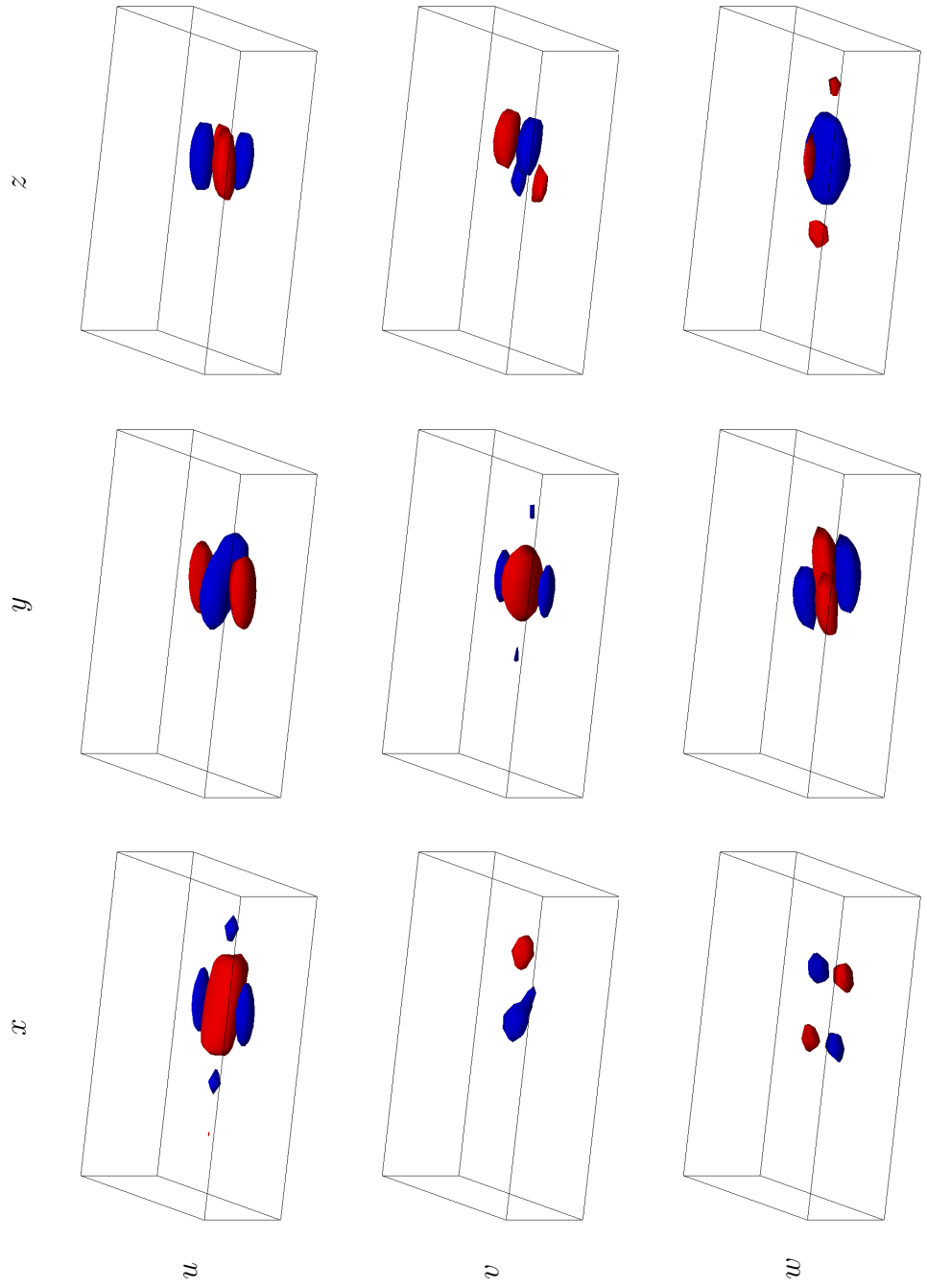


FIGURE 4.16. Isosurface of the response tensor $\mathcal{H}_{ij}$ at the non dimensional time $\mathcal{T} = 0.5$ for the laminar case. The forcing is at the wall-normal distance $\bar{y} = -0.9045$ All the isosurfaces are at the value $\pm 1$. (red for positive values, blue for negative ones).

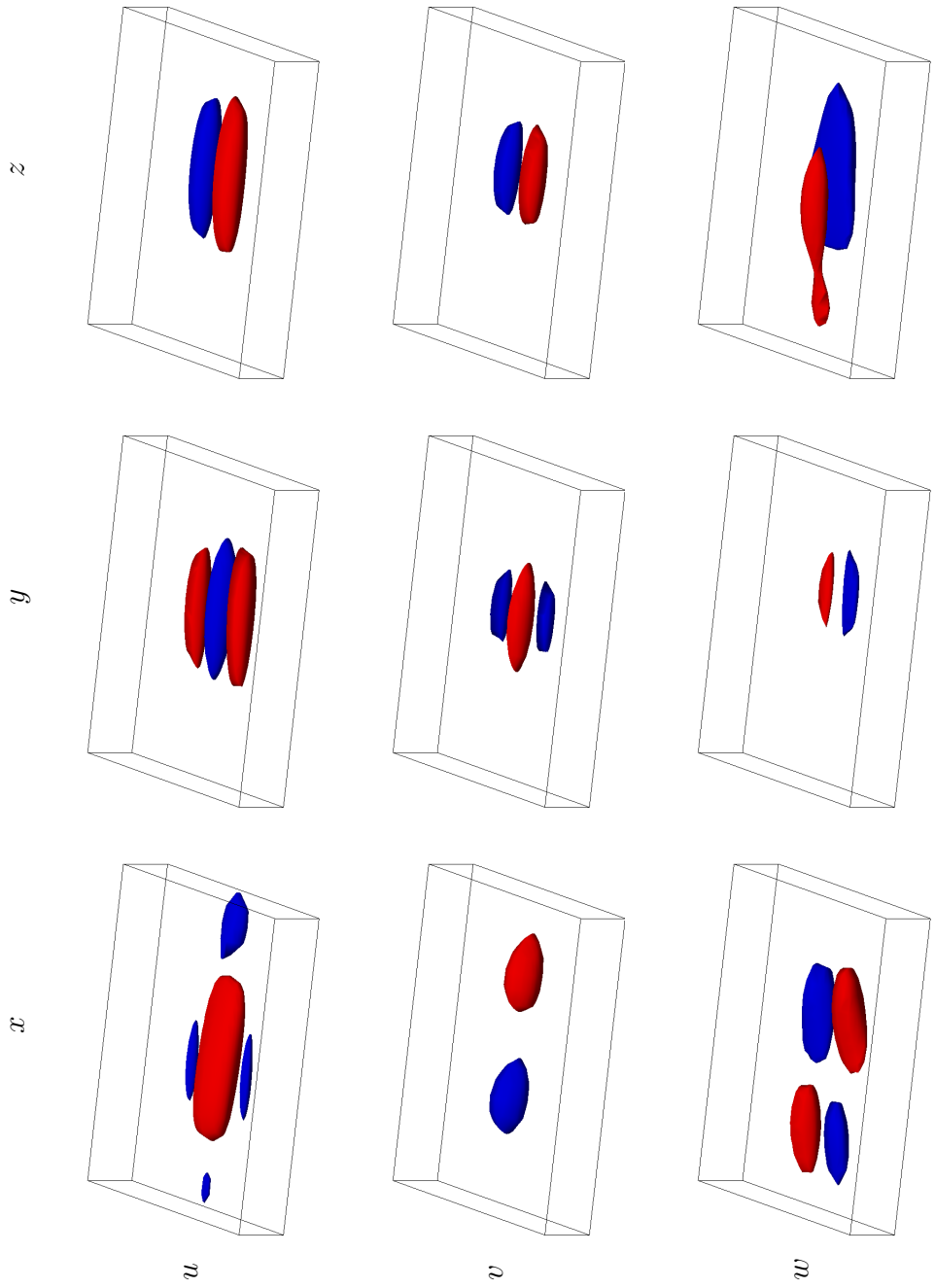


FIGURE 4.17. Isosurface of the response tensor $\mathcal{H}_{ij}$ at the non dimensional time $\mathcal{T} = 0.5$ for the turbulent case. The forcing is at the wall-normal distance $\bar{y} = -0.9697$ ($\bar{y}^+ = 4.54$) All the isosurfaces are at the value $\pm 0.5$ except for the components $\mathcal{H}_{vx}$ and $\mathcal{H}_{wx}$ which are at the value $\pm 0.25$. (red for positive values, blue for negative ones).

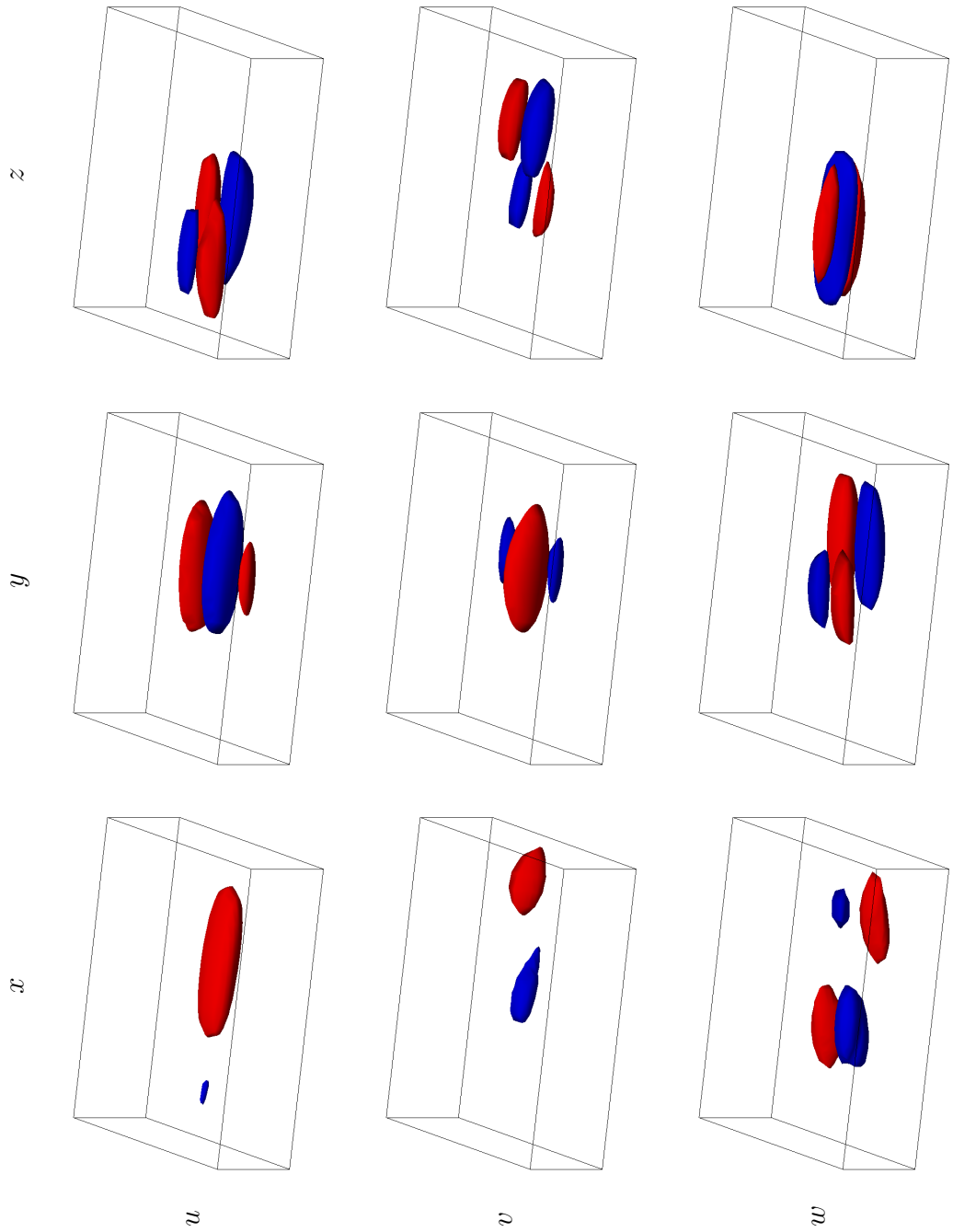


FIGURE 4.18. Isosurface of the response tensor $\mathcal{H}_{ij}$ at the non dimensional time $\mathcal{T} = 0.5$ for the turbulent case. The forcing is at the wall-normal distance $\bar{y} = -0.9097$ ($\bar{y}^+ = 14$) All the isosurfaces are at the value $\pm 0.5$ except for the components on the diagonal ($\mathcal{H}_{ii}$) and $\mathcal{H}_{uy}$ and $\mathcal{H}_{uz}$ which are at the value $\pm 1$. (red for positive values, blue for negative ones).

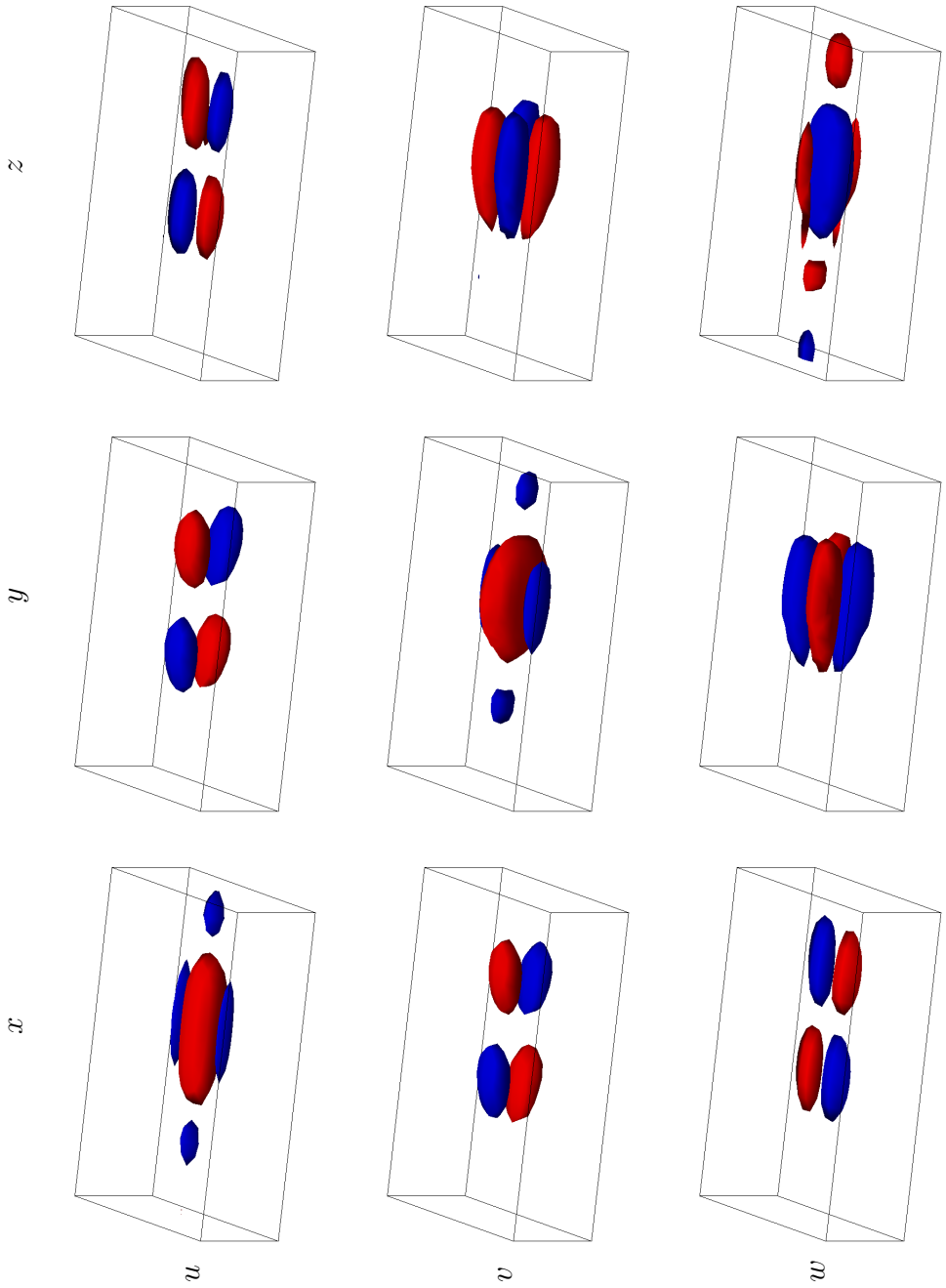


FIGURE 4.19. Isosurface of the response tensor $\mathcal{H}_{ij}$ at the non dimensional time $\mathcal{T} = 0.5$ for the turbulent case. The forcing is at the channel centerline $\bar{y} = 0$ ($\bar{y}^+ = 150$) All the isosurfaces are at the value $\pm 0.5$ except for the components on the diagonal ($\mathcal{H}_{ii}$) which are at the value $\pm 1$. (red for positive values, blue for negative ones).

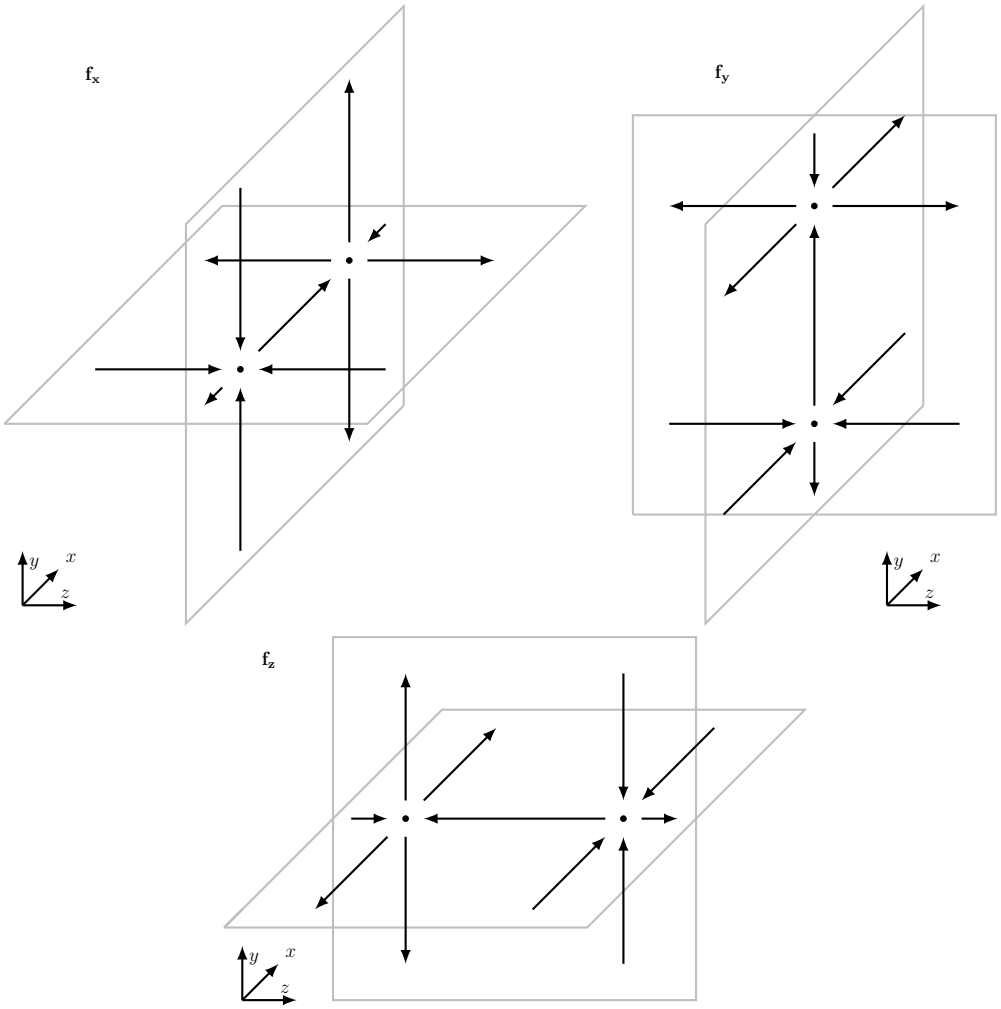


FIGURE 4.20. Topology of the interaction mechanisms between the forcing perturbations and the velocity field. This figure is made by considering the three dimensional effects of each forcing direction, as they appear in the isosurfaces figure 4.19, obtained posing the forcing at the channel centerline. The two dots are the saddle points.

### 4.2.5 Isosurfaces evolution of $\mathcal{H}_{uz}$

The interesting non-normal behaviour of the components $\mathcal{H}_{uz}$ and $\mathcal{H}_{uy}$, seen in subsection 4.2.2, can be studied in deep with an isosurfaces evolution analysis.

Figure 4.21 shows the evolution of the response component $\mathcal{H}_{uz}$ among nine different time snapshots, starting from $\mathcal{T} = 0$ to $\mathcal{T} = 4$. The forcing is posed at the wall-normal distance $\bar{y} = -0.9067$. At the first time step $\mathcal{T} = 0$, the negative and positive isosurfaces are arranged symmetrically at the corners of an hypothetical square. This brings to the creation of a wall-normal vorticity which is positive on the front and negative on the rear. The initial isosurfaces present a less regular shape. This occurs since the forcing is applied in the wavenumbers space as a delta-correlated white noise and, after the inverse Fourier transform the forcing assumes, in the physical space, the shape of a Dirac delta. Hence the first time steps are influenced by the highly irregular shape of the forcing at the origin.

The following shown time step is at $\mathcal{T} = 0.1$ and the isosurfaces become more regular due to the viscous diffusion phenomena. Furthermore the diffusion, with its smoothing effect, reduces the isosurfaces significantly. This trend can be clearly seen in figure 4.11, where the maximums of $\mathcal{H}_{uz}$ among the time experiences a downward peak. From this snapshot on, the isosurface becomes to grow due to transient growth effects and this behaviour can be easily seen in the succeeding snapshots. It must be notice that even if the isosurfaces seem to go on growing, as the time advances, the maximums values reach a peak at $\mathcal{T} = 0.5$ and then begin to decrease again. This occurs since the diffusion effects spread the velocity in the space, making the isosurface bigger, despite the maximum values inside the isosurfaces are getting lower and lower.

The upper isosurfaces are transported faster by the mean velocity profile. This leads to invert the wall-normal vorticity component which is created by the arrangement of the velocity isosurfaces.

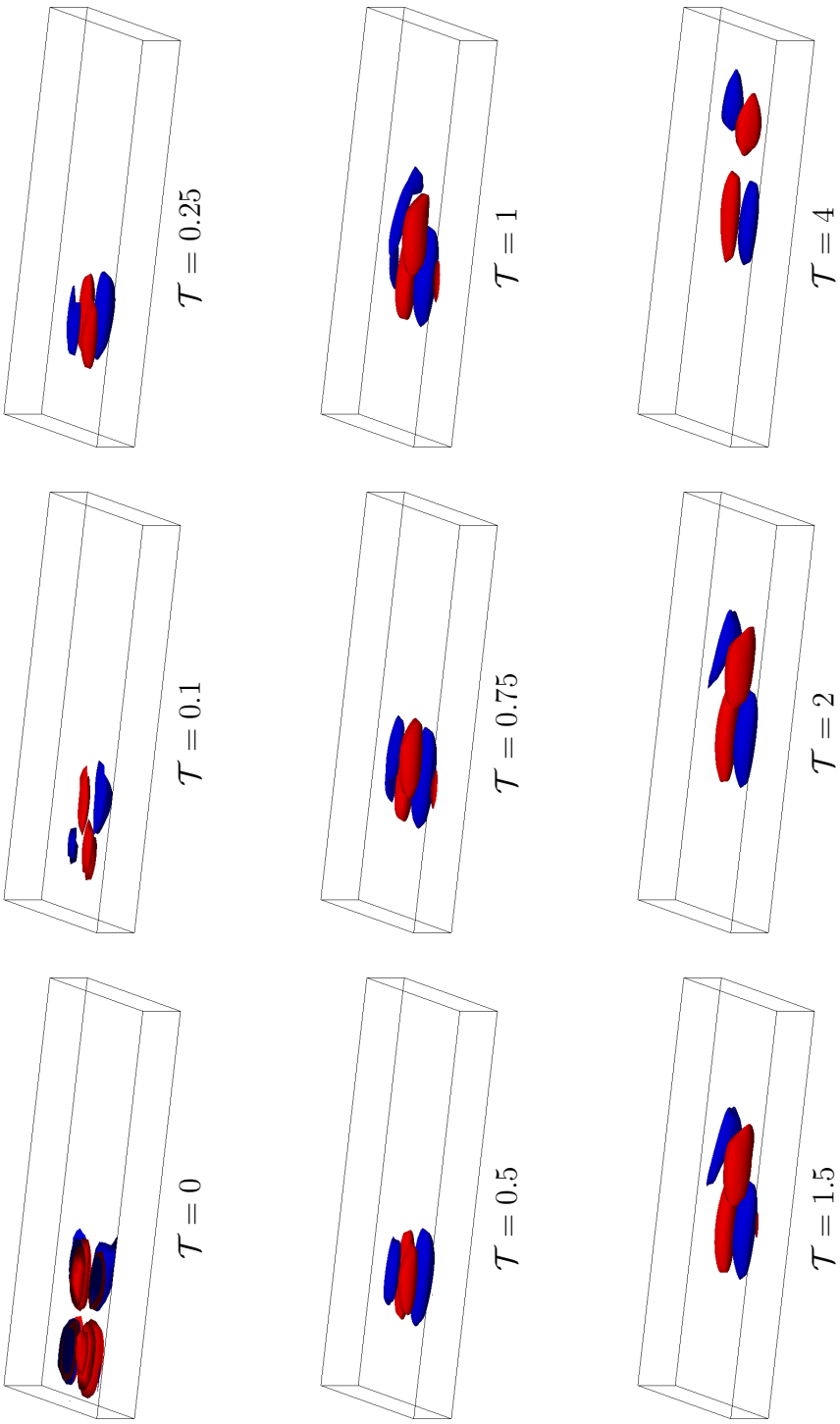


FIGURE 4.21. Time evolution of the isosurfaces of the response component $\mathcal{H}_{uz}$. The isosurfaces are at the value $\pm 0.5$.

## 4.3 Direct convolution

The Direct convolution computation has a great importance for a twofold reason. First of all, as seen in the subsection 3.2.2, this approach is a validation *a posteriori* of the impulse response results. Indeed, if the output velocity field obtained with the convolution computation is coincident with the one obtained with a DNS (which applies the same forcing history), the impulse response validation is provided. The second reason lies in the possibility to probe the effect of a given forcing by computing directly the mean velocity filed, without the need of the computational efforts of a DNS approach, which requires a long simulation time to performs the average. Furthermore this kind of computation allows to check the presence of possible nonlinearity.

The following results are obtained with the formulation presented in section 2.4.

**Laminar flow**

The response parameters employed for the convolution computation are the same as those ones used for the response measurement shown in table 3.2, and also the comparing DNS simulation uses the same channel flow parameters shown in table 3.1. The convolution results show here are obtained with forcing at the wall-normal distance $\bar{y} = -0.8685$. The forcing amplitude is $\epsilon = 0.001$, which assures that the linearity range is respected.

The forcing used to obtained the laminar results in figure 4.22 is the following

$$\mathfrak{f}_j(x, z, t) = \epsilon \cos(2\pi x) \cos(2\pi z) \sin(2\pi t) \qquad j = 1, 2, 3 \tag{4.2}$$

which can be transformed in the wavenumbers space as

$$\hat{\mathfrak{f}}_j(\alpha, \beta, t) = \epsilon \sin(pit) \tag{4.3}$$

with $\alpha = 1$ and $\beta = \pm 1$. Since this forcing is three-dimensional, the equation used to compute the convolution is the 2.27 which is reported here.

$$\hat{u}_i(\alpha, y, \beta, t; \bar{y}) = \sum_{j=1}^{3} \int_{-\infty}^{\infty} \hat{\mathcal{H}}_{ij}(\alpha, y, \beta, t - \tau; \bar{y}) \hat{\mathfrak{f}}_j(\alpha, \beta, \tau) d\tau \tag{4.4}$$

Figure 4.22 shows the maximums and minimums behaviours of the velocity field, computed both with the convolution and the DNS. The overall matching is good, however, while in the first part of the transitory difference between the curves is neglectable, as the time advances a little error

increases. This trend is easily explained observing the equation 2.27, where we can notice that each term of the summation contributes to increase the numerical error.

### Turbulent flow

The comparison between the convolution and the DNS based results becomes much more difficult for the turbulent case. The reason is the great simulation time required to simulate the mean transient effect of the forcing with a DNS based approach. Indeed the correct way to measure this mean velocity transient would consists in a phased-locked averaged process. During this process the forcing should be switched on for the desired simulation time and then switched off for certain amount of time, which is necessary to obtain a velocity field completely uncorrelated with the forcing effects. Unfortunately the time needed to have an uncorrelated velocity field is so elevated that this process becomes unaffordable.

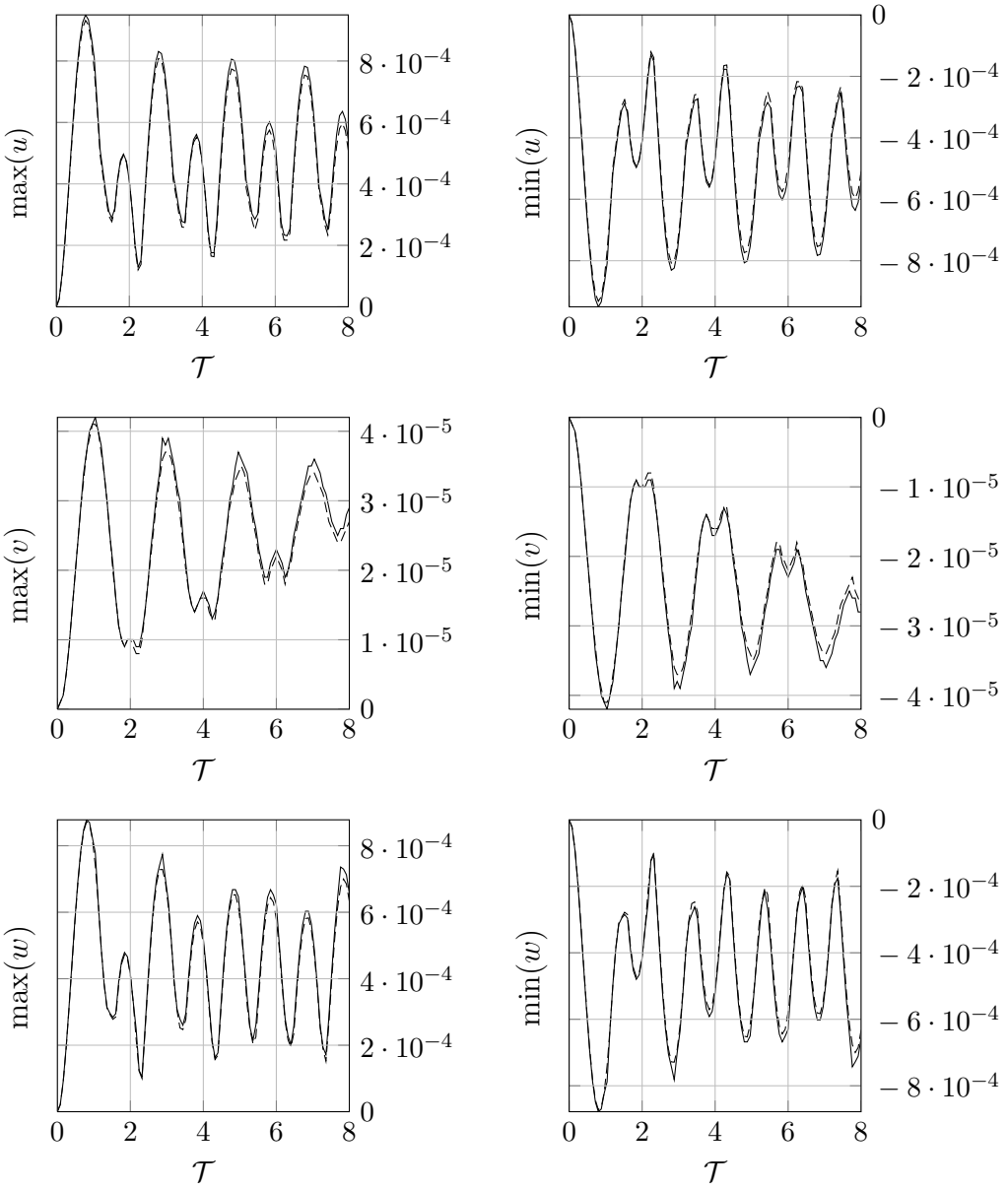


FIGURE 4.22. Maximum of the velocity components in the physical space as result of the convolution between $\mathcal{H}_{ij}$ (at the wall-normal distance $\bar{y} = -0.8685$) and the forcing in the equation 4.3. (- - -) DNS, (——) convolution. with the truncated response

# 5 | Conclusions

This thesis presents, for the first time, a complete description of the mean impulse response function of a turbulent channel flow by means of a DNS measurement. The impulse response is related to a body forcing input applied at different distances from the wall of the channel, while the output is the velocity field. The computational program used for the numerical response measurement is based on the DNS solver implemented by Luchini and Quadrio in [19], with the body forcing added and validated by Pelis and Rampanelli in [28]. Further program extensions of the response measurement procedure are developed in this thesis, in order to improve the computational speed. This improvements have been a key factor since the measurement procedure treat the dependency from forcing distance with a parametric approach, which requires an huge amount of computational efforts.

For this reason, great attention is posed to the setting of the impulse response parameters and to the planning of the simulations campaign among the forcing distances. In particular, a truncation analysis in the wavenumbers space has been performed, in order to reduce the memory space required by the impulse response which must taken into account the velocity field for a given number of time steps.

Two main simulations campaigns have been done, one with a laminar base flow and the other with a fully developed turbulent flow at $Re_\tau = 150$. The linearity results about the laminar case presented in [28] have been extended to the turbulent case by means of simulations at different forcing distances, in order to study the linearity range exploitable with the response measurement procedure employed. This analysis has founded that the linearity range is bigger for the lower forcing distances near the wall, because of the higher dissipation phenomena that damp the forcing effects.

The analysis of the results is mainly divided in two parts. The first one concerns the visualization of the energetic content of the response, which leads to interesting consideration about the most suitable forcing directions for a possible control application. The laminar case is initially studied so

to have a possible comparison with the laminar results present in literature such as the work of Jovanović and Bamieh [13], where the authors analyzed the laminar impulse response by means of the $H_2$ norm in the wavenumbers space. The results found by them about the major influence of the response components $\mathcal{H}_{uy}$ and $\mathcal{H}_{uz}$ are confirmed, furthermore their results have been extended by considering different forcing distances which show that near the wall the component $\mathcal{H}_{uz}$ has the most remarkable influence and as we increase the wall-normal distance also the components $\mathcal{H}_{ux}$ and $\mathcal{H}_{uy}$ become stronger. Also in the turbulent case the most influent components concerns the streamwise velocity ones $\mathcal{H}_{uj}$ and their influence increase with the forcing distance.

Then, the response analysis focused on physical space, where the $H_\infty$ norm was analyzed to investigate the maximum and minimum behaviour of each response components among the time. The physical space results show that the most relevant components are $\mathcal{H}_{ii}$ which share the same input-output direction. We must notice that the component $\mathcal{H}_{vy}$ drastically decreases as the forcing distance gets close to the wall. Furthermore the maximums and minimums among the time of the extra-diagonal components show interesting behaviour of transient growth which may give useful information about the non normal behaviour of the Navier–Stokes equations.

The maximums of $\mathcal{H}_{ij}$ was studied also in relation to different forcing distances, in order to find the most relevant forcing distance for control application. This analysis showed that the maximum effects of the forcing distance is obtained quite always at the channel centerline. Few components showed a quite constant behaviour with weak local peaks near the quarter of the channel height.

The second part of the results analysis is focused on the study of the interaction mechanisms between the forcing and the flow. Thanks to three dimensional visualizations it was possible to identify to flow topology of this interaction mechanisms which allows to understand how the body perturbations are propagated. At the channel centerline, where the flow has a more isotropic behaviour, there exists a mechanism which is common to all the three forcing directions, Lowering the forcing distance this mechanism vanishes and near the wall we need a specific reconstruction of the interaction topology for each response component.

The last part of the results concerns the computation of the convolution, which allows to compute the velocity field due to a given forcing by means of the impulse response. The good matching between the convolution results and the DNS simulations, which employed the same convolution forcing, is an index of the reliability of the computed impulse response.

This work presented in this thesis allows many further developments, es-

pecially from the numerical viewpoint much work is yet to come to investigate the effects of different Reynold numbers. The Reynolds parameter dependency can be very important for the research of the correct scaling between different flow conditions. Higher Reynolds could allows to simulate interesting flow condition also from an industrial viewpoint. Furthermore, the research of the scaling and the effects of $Re_\tau$, can bring to the developments of useful mathematical models, which may help the closure problems about the turbulent flows modeling.

Interesting flow control applications can start from this work. A control based on the Wiener-Hopf filter can be designed starting from the impulse response dataset computed in this work. Practical applications can be based on plasma or electromagnetic actuators, which can find great industrial purposes in the aeronautic or the biomedical field.

# A | Estratto in lingua Italiana

Molti dei fenomeni fisici che ci circondano nella vita di tutti i giorni sono legati a correnti turbolente. La scia di un aereo, i gas nelle stelle, lo scorrere del sangue nelle vene, le correnti oceaniche e atmosferiche, sono tutti fenomeni turbolenti che hanno un forte impatto sulla vita degli esseri umani. Questo spiega il grande interesse che da sempre suscitano questo tipo di correnti.

Prima di introdurre l'argomento principale della tesi, ossia la risposta impulsiva media in un flusso turbolento, è utile presentare lo stato dell'arte della ricerca riguardo al controllo di flussi turbolenti.

Le tecniche di controllo della turbolenza hanno la grande capacità di poter mainipolare il campo di moto al fine di ottenere comportamenti specifici del flusso che migliorano o soddisfano determinati obbiettivi. L'impatto economico dello sviluppo di queste tecnologie porterebbero al risparmio di miliardi di dollari riguardo al comsumo di carbulante per veicoli di ogni tipo.

In campo aeronautico, l'interesse principale è rivolto alla possibilità di ottenere consistenti riduzioni di attrito e quindi della resistenza aerodinamica. Questa tesi si collega al filone di ricerca che riguarda il controllo attivo, cioè che immette energia nel sistema, e in particolare al controllo tramite forzanti di volume. A differenza di altri metodi, l'uso di forze di volume permette di operare direttamente nell'intero dominio considerato, e non solo sul contorno, con notevoli vantaggi di versatilità.

La realizzazioni di tali forze può avvenire tramite attuatori elettromagnetici, usati nel controllo di flussi ionizzati, oppure tramite l'impiego di attuatori al plasma freddo per fluidi standard come l'aria. Negli ultimi vent'anni molto lavoro è stato fatto a questo proposito sia dal punto di vista numerico che sperimentale, un esempio sono i seguenti lavori: Berger *et al.* [1], Pang and Choi [26], Du *et al.* [8], Stenzel *et al.* [37, 36], Moreau [22] and by Corke *et al.* [6].

I principali lavori che hanno portato allo sviluppo di questa tesi riguardano la teoria del controllo lineare applicato a correnti tubolente. In particolare in [18] Luchini, Bewley e Quadrio hanno posto le basi per l'implementazione di

un controllo basato sul filtro di Wiener-Hopf. Tale controllo sfrutta la proprietà della risposta impulsiva di poter descrivere la dinamica del sistema in un unico oggetto matematico. Ciò ha portato allo sviluppo di una nuova tecnica per misurare la risposta impulsiva in un flusso turbolento ([20] Luchini, Quadrio e Zuccher) basata su un controllo di tipo *blowing/suction* a parete. Questa tecnica è stata estesa a forzanti di volume nella tesi di Pelis e Rampanelli [28] ed è stata ulteriormente sviluppata in questa tesi per affrontare al meglio il notevole sforzo computazionale richiesto.

**Flusso nel canale piano**

Il canale piano svolge un importante ruolo nello studio dell'interazione tra correnti turbolente e pareti rigide. Questo genere di problema modello fornisce un ottimo banco di prova per lo studio della turbolenza e della transizione in flussi confinati da pareti. Inoltre questa particolare geometria permette un'implementazione numerica molto efficente delle simulazioni dirette (DNS) a moderati numeri di Reynolds, e mostra molte delle caratteristiche anche dei flussi più complessi. L'approcio tramite DNS permette di risolvere fedelmente anche le scale spazio-temporali più fini dei fenomeni turbolenti e lo sforzo computazionale richiesto è bilanciato dalla semplicità del dominio di calcolo.

Il codice di calcolo utilizzato si basa sulla discretizzazione delle equazioni di Naver–Stokes incomprimibili. La particolare geometria del problema permette di espandere in serie di Fourier la soluzione nelle direzioni omogenee parallele alle pareti. Come mostrato da Kim *et.al.* in [16], le equazioni di Navier-Stokes possono essere riscritte in due nuove variabili: la vorticità normale a parete $\eta$ e la velocità normale a parete $v$. Il sistema di equazioni differenziali alle derivate parziali si compone, quindi, di un'equazione del quarto ordine spaziale in $v$ e una del secondo in $\eta$.

$$\begin{cases} \dfrac{\partial \nabla^2 v}{\partial t} = h_v + \dfrac{1}{Re}\nabla^2\nabla^2 v + \left(\dfrac{\partial^2}{\partial^2 x} + \dfrac{\partial^2}{\partial^2 z}\right) f_y - \dfrac{\partial}{\partial y}\left(\dfrac{\partial f_x}{\partial x} + \dfrac{\partial f_z}{\partial z}\right) \\ \dfrac{\partial \eta}{\partial t} = h_\eta + \dfrac{1}{Re}\nabla^2\eta + \dfrac{\partial f_x}{\partial z} - \dfrac{\partial f_z}{\partial x} \\ \dfrac{\partial v}{\partial y}(x, y_{l/u}, z) = 0 \qquad \text{non-penetration} \\ \left.\begin{array}{l} v(x, y_{l/u}, z) = 0 \\ \eta(x, y_{l/u}, z) = 0 \end{array}\right\} \qquad \text{non-slip} \end{cases} \tag{A.1}$$

La discretizzazione spaziale nel piano sfrutta la rappresentazione della soluzione in serie di Fourier definendo un certo numero di frequenze spaziali

risolte. La discretizzazione in direzione normale alla parete è per diferenze finite del quarto ordine. La particolarità del codice consiste nel trattamento in modo esplicito del termine non lineare. Ciò permette di risolvere in modo rapido tanti piccoli sistemi due per due, uno per ogni quota e per ogni coppia di numeri d'onda, incrementando notevolmente la facilità di parallelizzazione e la velocità di calcolo. Il passo di integrazione esplicita con un Runge–Kutta del terzo ordine è poi corretto con un metodo di Crank–Nicholson, il quale rende il metodo semi implicito.

### Risposta impulsiva media nel canale

Anche se una corrente turbolenta è un fenomeno non lineare, si può definire una risposta lineare a delle perturbazioni abbastanza piccole. Sotto l'ipotesi di linearità la risposta di una corrente turbolenta può essere descritta con un'unico oggetto matematico detto risposta impulsiva. La risposta impulsiva è un strumento potente che permette di caratterizzare il comportamento del sistema, soggetto ad una forzante esterna, cercando direttamente la connessione tra ingresso e uscita.

La misura della risposta risposta impulsa svolta in questa tesi si basa sulla tecnica esposta per la prima volta da Luchini, Quadrio e Zuccher in [20]. Il principio della misura si basa su un risultato noto della teoria dei segnali: la correlazione tra ingresso e uscita di un sistema è proporzionale alla risposta impulsiva di quest'ultimo. Considerando il sistema come lineare, il campo di velocità in uscita si ottiene dalla seguente convoluzione:

$$u_i(x,y,z,t) = \int_0^{L_x}\int_{-\delta}^{\delta}\int_0^{L_z}\int_{-\infty}^{\infty} \mathcal{H}_{ij}(x-\xi, y-\eta, z-\zeta, t-\tau) f_j(\xi,\eta,\zeta,\tau) d\tau d\zeta d\eta d\xi \tag{A.2}$$

Dato che, nelle direzioni omogenee, la soluzione è espansa in serie di Fourier, la convoluzione diventa semplicemente un prodotto. La dipendenza da $y$ è invece risolta applicando la forzante con una distribuzione a delta di Dirac, quindi la risposta ottenuta sarà legata ad una singola quota di forzamento.

$$\hat{f}_j(\alpha,y,\beta,t) = \hat{\mathfrak{f}}_j(\alpha,\beta,t)\delta(y-y') \tag{A.3}$$

Sostituendo questo forzamento nell'equazione A.2 si ricava la seguente equazione

$$\hat{u}_i(\alpha,y,\beta,t) = \int_{-\infty}^{\infty} \hat{\mathcal{H}}_{ij}(\alpha, y-y', \beta, t-\tau)\hat{\mathfrak{f}}_j(\alpha,\beta,\tau) d\tau \tag{A.4}$$

La misura basata sulla DNS si ottiene, quindi, dalla correlazione tra ingresso e uscita nel seguente modo:

$$\langle \hat{u}_i(\alpha, y, \beta, t)\hat{\mathfrak{f}}_j^*(\alpha, \beta, t-\mathcal{T})\rangle = \int_0^\infty \hat{\mathcal{H}}_{ij}(\alpha, y, \beta, t-\tau; y')\langle \hat{\mathfrak{f}}_j(\alpha, \beta, \tau)\hat{\mathfrak{f}}_j^*(\alpha, \beta, t-\mathcal{T})\rangle d\tau \tag{A.5}$$

Applicando un rumore bianco la cui autocorrelazione è la delta di Dirac ed esplicitando la risposta impulsiva $\hat{\mathcal{H}}_{ij}$ otteniamo l'equazione che permette di misurare la rispsota impulsiva

$$\hat{\mathcal{H}}_{ij}(\alpha, y, \beta, \mathcal{T}; y') = \frac{\langle \hat{u}_i(\alpha, y, \beta, t)\hat{\mathfrak{f}}_j^*(\alpha, \beta, t-\mathcal{T})\rangle}{\epsilon^2} \tag{A.6}$$

**Pianificazione delle simulazioni**

Come si può vedere dall'equazione A.6, la risposta dipende in modo parametrico dalla quota di forzamento $\bar{y}$. Questo significa che la completa conoscenza della risposta impulsiva a varie quote, necessita di più simulazioni. In questa tesi sono stati analizzati due differenti numeri di Reynolds, $Re_\tau = 100$ per il caso laminare e $Re_\tau = 150$ per il caso turbolento. Per ciascuno dei due Reynolds, sono state condotte varie simulazioni a varie quote $\bar{y}$, l'elenco di tali prove si trova nelle tabelle 3.4 e 3.5.

Ovviamente tutto ciò richiede un notevole sforzo computazionale, che è stato affrontato con l'ausilio del centro di calcolo interuniversitario del CINECA, in particolare le simulazioni turbolente hano richiesto tre mesi di calcolo sulla macchina PLX.

Alcune modifiche all'algoritmo di misura sono state apportate per migliorarne la velocità. È stato aggiunta la possibilità di forzare il flusso in modo tridimensionale e con un passo temporale variabile.

Particolare attenzione è stata rivolta alla scelta dei parametri della risposta, soprattutto alla scelta di uno spazio di numeri d'onda ridotto, da considerare nel calcolo della risposta, così da ridurre le dimensioni su disco della risposta stessa, le quali sarebbero risultate altrimenti proibitive.

**Risultati**

La parte iniziale dei risultati consiste nell'analisi di linearità della risposta nel caso turbolento. Per verificare la linearità sono state efettuate prove su cinque quote $\bar{y}$ diverse con due differenti ampiezze di forzamento. Come si può vedere dalla figura 4.2, nonostante le ampiezze usate siano una il doppio dell'altra, le due risposte ottenute presentano delle piccole differenze di non più del 3% tra loro.

La risposta impulsiva è un tensore del quarto ordine $\mathcal{H}_{ij}(\alpha, y, \beta, \mathcal{T}; \bar{y}$, risulta, quindi, chiaro che una sua possibile visualizzazione neccessiti di appositi strumenti matematici. Uno di questi è senza dubbio la norma $H_2$ nello spazio dei numeri d'onda. L'analisi di tale norma per ogni componente di $\mathcal{H}_{ij}$ e per ogni quota permette di capire quale componente risulti più influente e in più, a seconda della distribuzione di energia tra i numeri d'onda, si può avere un'idea della forma delle strutture nello spazio fisico. Questa analisi ha confermato dei risulatati noti in letteratura ([13]), i quali indicano che le componenti più influenti sono $\mathcal{H}_{uy}$ e $\mathcal{H}_{uy}$. Inoltre i risultati in letteratura sono stati anche estesi per quanto riguarda la dipendenza dalla quote di forzamento, in particolare si è trovato che vicino a parte la componente $\mathcal{H}_{uy}$ risulta avere un piccolo impatto e $\mathcal{H}_{ux}$ risulta comparabile con $\mathcal{H}_{uz}$. questi risultati sono visibile dalle figure 4.3, 4.4, 4.5, 4.7, 4.8, 4.9.

La ricerca delle componenti più influenti è stata fatta anche studiando la risposta nello spazio fisico, andando a calcolare l'evoluzione dei massimi e dei minimi nel tempo (figure 4.10, 4.11, 4.12,4.13). Da quest'analisi risulta che le componenti più influenti sono quelle situate sulla diagonale, ovvero quelle per le quali il forzamento e la velocità sono nella stessa direzione. Le tre componenti $\mathcal{H}_{iy}$ relative al forzamento normale alla parete presentano una notevole diminuizione man mano che ci si avvicina alla parete. Questi risultati sono stati confermati andando a studiare anche l'andamento dei massimi e minimi rispetto alla quota di forzamento $\bar{y}$ (figura 4.14).

L'analisi della risposta nello spazio fisico, tramite la visualizzazione di isosuperfici, ha portato alla comprensione dei meccanismi di interazione tra la forzante e il campo di moto. Infatti, per quanto riguarda il forzamento in centro al canale, dove il flusso assume delle carateristiche più omogenee, è stato possibile identificare un mecchanismo di iterazione comune a tutte e tre le direzioni di forzamento. Avvicinadosi a parete, invece, la turbolenza è sempre più anisotropa e i meccanismi di interazione possono essere dedotti solo componente per componente, tramite un'analisi sulla vorticità che la forzante instaura nel campo di moto.

L'ultimo aspetto analizato nei risultati è l'ottenimento del campo di velocità direttamente sfruttando la convoluzione con un ingresso noto, quindi senza l'utilizzo di simulazioni dirette. Nel caso laminare, è stato possibile effettuare un confronto tra i risultati della convoluzione e le simulazioni dirette (a parità di ingresso), il quale risulta essere in ottimo accordo, fornendo quindi una prova dell'affidabilità delle misure effettuate.

# Bibliography


[1] T. W. Berger, J. Kim, C. Lee, and J. Lim. Turbulent boundary layer control utilizing the Lorentz force. *Phys. Fluids*, 12(3):631–649, 2000.

[2] T. Bewley. Flow Control: New Challenges for a New Renaissance. *Prog. Aerosp. Sci.*, 37:21–58, 2001.

[3] S.A. Billings. Identification of nonlinear systems-a survey. In *IEE Proc.*, volume 127, pages 272–285, 1980.

[4] M. Carini and M. Quadrio. The DNS-based measurement of the mean impulse response of homogeneous isotropic turbulence. *Submitted to Phys. Rev. E*, 2010.

[5] K.-S. Choi, T. Jukes, and R. Whalley. Turbulent boundary-layer control with plasma actuators. *Phil. Trans. R. Soc. A*, 369(1940):1443–1458, 2011.

[6] C. L. Corke, T. C. Enloe and S. P. Wilkinson. Dielectric barrier discharge plasma actuators for flow control. *Annu. Rev. Fluid Mech.*, 42:505–529, 2010.

[7] Kurt Courant, R. Friedrichs and H. Lewy. On partial diferential equations of mathematical physics. *IBM journal of Research and Development*, 1967.

[8] Y. Du, V. Symeonidis, and G. E. Karniadakis. Drag reduction in wall-bounded turbulence via a transverse travelling wave. *J. Fluid Mech.*, 457:1–34, 2002.

[9] B.F. Farrel and P.J. Ioannou. Stochastic forcing of the linearized Navier–Stokes equations. *Phys. Fluids*, 5(11):2600–2609, 1993.

[10] M. Gad-el Hak. Flow Control: the Future. *J. Aircraft*, 38(3):402–418, 2001.

[11] A.K.M.F. Hussain and W.C. Reynolds. The mechanics of an organized wave in turbulent shear flow. *J. Fluid Mech.*, 41(2):241–258, 1970.

[12] M. R. Jovanović and B. Bamieh. Input-output analysis of the linerized Navier–Stokes equations in channel flows. *J. Fluid Mech. (rejected)*, 2002.

[13] M. R. Jovanović and B. Bamieh. Componentwise energy amplification in channel flows. *J. Fluid Mech.*, 534:145–183, 2005.

[14] K. Zhou, J. C. Doyle, and K. Glover. *Robust and Optimal Control*. Prentice Hall, 1996.

[15] N. Kasagi, Y. Suzuki, and K. Fukagata. MEMS-based feedback control of turbulence for drag reduction. *Annu. Rev. Fluid Mech.*, 41:231–251, 2009.

[16] J. Kim, P. Moin, and R. Moser. Turbulence statistics in fully developed channel flow at low Reynolds number. *J. Fluid Mech.*, 177:133–166, 1987.

[17] F. Auteri L. Quartapelle. *Fluidodinamica Incomprimibile*. Casa Editrice Ambrosiana, 2013.

[18] P. Luchini, T. Bewley, and M. Quadrio. An optimal feedback controller for the reduction of turbulent energy in 3D plane-duct flow. In *APS Meeting, Chicago, IL (US), November 20-22*, 2005.

[19] P. Luchini and M. Quadrio. A low-cost parallel implementation of direct numerical simulation of wall turbulence. *J. Comp. Phys.*, 211(2):551–571, 2006.

[20] P. Luchini, M. Quadrio, and S. Zuccher. Phase-locked linear response of a turbulent channel flow. *Phys. Fluids*, 18:121702/1–4, 2006.

[21] F. Martinelli. *Feedback control of turbulent wall flows*. PhD thesis, Politecnico di Milano, 2009.

[22] E. Moreau. Airflow control by non-thermal plasma actuators. *Journal of Physics D: Applied Physics*, 40.3:605, 2007.

[23] R. Moser, J. Kim, and N.N. Mansour. Direct numerical simulation of turbulent channel flow up to $Re_\tau = 590$. *Phys. Fluids*, 11(4):943–945, 1999.

[24] W. M. F. Orr. The stability or instability of the steady motions of a perfect liquid and of a viscous liquid. Part II. A viscous liquid. *Proc. R. Irish Acad. Sect. A: Math. Phys. Sci.*, 27:69–138, 1907.

[25] Orszag S. A. Accurate solution of the Orr-Sommerfeld stability equation. *J. Fluid Mech.*, 50(4):689–703, 1971.

[26] J. Pang and K.-S. Choi. Turbulent drag reduction by Lorentz force oscillation. *Phys. Fluids*, 16(5):L35–L38, 2004.

[27] A. Pantokratoras and E. Magyari. EMHD free-convection boundary-layer flow from a Riga-plate. *J. Eng. Math.*, 64:303–315, 2008.

[28] M. Pelis and M. Rampaneli. Risposta impulsiva in un flusso turbolento. Master's thesis, Politecnico di Milano, Milano-Italy, 2011.

[29] S.B. Pope. *Turbulent Flows*. Cambridge University Press, Cambridge, 2000.

[30] C.O. Porter, T.E. McLaughin, C.L. Enloe, G.I. Font, J. Roney, and J.W. Baughn. Boundary layer control using a DBD plasma actuator. Technical report, 45th AIAA Aerospace Sciences Meeting and Exibit, 2007.

[31] A. Pozzi. *Application of Padé's Approximation Theory in Fluid Dynamics*. Advances in Mathematics for Applied Sciences. World Scientific, 1994.

[32] Alfio Quarteroni. *Modellistica Numerica per Problemi Differenziali*. Springer, 2008.

[33] P. Schmid. Nonmodal stability theory. *Annu. Rev. Fluid Mech.*, 39:129–162, 2007.

[34] P.J. Schmid and D.S. Henningson. *Stability and Transition in Shear Flows*. Springer, 2001.

[35] G. Schrauf. Key Aerodynamic Technologies for Aircraft Performance Improvement. In 5th Community Aeronautics Days, 2006.

[36] R. L. Stenzel, J. M. Urrutia, M. C. Griskey, and K. D. Strohmaier. 3D EMHD reconnection in a laboratory plasma. *Earth Planets Space,*, 53:553–560, 2000.

[37] R.L. Stenzel, J.M. Urrutia, and K.D. Strohmaier. Experiments on nonlinear EMHD fields. *Physica Scripta*, T107:163–166, 2004.

[38] T. Yoshino, Y. Suzuki, and N. Kasagi. Feedback control of turbulence air channel flow with distributed micro-sensors and actuators. *J. Fluid Sci. Technol.*, 3:137–148, 2008.